Computer Simulation of a Nitric Oxide-Releasing Catheter with a Novel Stable Convection-Diffusion Equation Solver and Automatic Quantification of Lung Ultrasound Comets by Machine Learning

by

Xianglong Wang

A dissertation submitted in partial fulfillment
of the requirements for the degree of
Doctor of Philosophy
(Biomedical Engineering and Scientific Computing)
in The University of Michigan
2020

Doctoral Committee:

Professor Joseph L. Bull, Co-Chair, Tulane University
Professor C. Alberto Figueroa, Co-Chair
Professor Mark E. Meyerhoff
Professor Xueding Wang
Professor William F. Weitzel III

Xianglong Wang

micw@umich.edu

ORCID iD: 0000-0001-5359-8411

The last thing you taught me / is that some happiness never comes back

–*Yonezu Kenshi, "Lemon"*

Acknowledgements

This could be long, so please bear with me.

It was not an easy march, as I looked back at the paths I have trekked through.

The finish line is finally in sight, after ample frustration from administrative processes, numerous contacts with the international center, frequent travels between New Orleans and Ann Arbor, and multiple bumps I have hit during my research. One person, however, supported me all the way through, and used every bit of resource he could get his hands on. That person is my adviser, Dr. Joseph Bull. I will always appreciate his relentless efforts to devise plans for my funding and coordination between multiple offices across the two universities. All of my achievements would be impossible without his support.

I really enjoyed working with the rest of my committee: my co-chair Dr. C. Alberto Figueroa, Dr. Mark Meyerhoff, Dr. Xueding Wang, and Dr. William Weitzel. I have great joy to work with all these people in additional to their presence on my committee, in the form of research collaboration or teaching a course together. I would also like to thank my former co-chair for two and a half years, Dr. Joan Greve, for her encouragement and mentorship, and Dr. Figueroa and Dr. Wang to step up to fill her former role. All of these people have helped me wrestle the administrative procedures, mentored me professionally or personally, or supported me financially. I am lucky for you all to be on my committee.

I was really lucky to collaborate with so many people at University of Michigan

and Tulane University, including Dr. Robert Bartlett and Dr. Panduranga Rao, who provided part of my funding; Dr. Elizabeth Brisbois, Dr. Yaqi Wo, and Dr. Xuewei Wang on the catheter project; Dr. Carolyn Bayer, whom I am teaching together with; Dr. Kenny Cha, Dr. Berkman Sahiner, and Dr. Kyle Myers for their providing me a great supportive environment during my FDA internship. My special thanks to Maria Steele, the graduate coordinator of BME for her help in a lot of the administrative processes.

I spent my day-to-day life with my lab partners. Whether I was the youngest student or the senior student in the lab, these people have made sure that I felt comfortable: the current members Dr. Jonah Harmon, M. Aimée Kayitesi, Chloe Celignant-Copie, Stephen Hahn, and Natalie Schwartz; our former members Dr. Foad Kabinejadian, Dr. David Li, Dr. John Pitre, Dr. Robinson Seda, Nelson Smith, and Sam Stephenson. Thank you - I really enjoyed working with you.

My Ph.D. life would not have been complete without personal support from my dear friends, Yuxin Shi and Claire Y. Lin. These two people have absorbed an amazing amount of my grumpiness and supported me unconditionally at all times. I am blessed and grateful to have you as my best friends.

I occasionally shuttled between New Orleans and Ann Arbor for my documents, meetings with my committee, or even doctor's appointments due to the restriction of my medical insurance. These would not have been possible without the help of my dear friends: Yuan Li, Zijian Qi, Weitao "Alex" Sun, and Xinyan Wang.

I would like to extend my thanks to the following people, including: Haowei Cai, Jackie Cha, Guanyu Gao, Jin Gao, Yuting Gao, Micah Glausier, Chris "Burris" Hochkeppel, Andrea Kim, Mengfan Li, Yinglong Li, Yuling Liu, Jie Ma, Dr. Xiaotian Tan, Dr. Matthew Thomson, J. Russell Tucker, Peng Xu, Xin "Pannie" Xu, Zhao Xu,

Xinchen Yan, Xiyu "Sylvia" Zhang, Ming Zhong, Rui Zhu... It is indeed impossible to list you all, but I am glad that our path has crossed, whether is in the form of being friends and traveling together, sitting down and making some music, being someone I could talk to at workplace, and/or even being fellow turnip stalkholders in Animal Crossing. Thank you for supporting me during my Ph.D. studies - I am deeply grateful.

Fortunate as I am to be living and writing this thesis at this very moment, some of my family, former classmates, or former students, are not as fortunate as they are no longer in this world. Be assured - every one of you has lived a meaningful life. To those who are living, treasure the ones beside you, because you never know if *the last thing you taught me / is that some happiness never comes back*.

Lastly - thank you Yili, for being my special one.

Stay safe, my parents, who were summoned into the efforts to contain the coronavirus spread in China.

Table of Contents

List of Figures

Figure

List of Tables

Table

Abstract

Biological transport processes often involve a boundary acting as separation of flow, most commonly in transport involving blood-contacting medical devices. The separation of flow creates two different scenarios of mass transport across the interface. No flow exists within the medical device and diffusion governs mass transport; both convection and diffusion exist when flow is present. The added convection creates a large concentration gradient around the interface. Computer simulation of such cases prove to be difficult and require proper shock capturing methods for the solutions to be stable, which is typically lacking in commercial solvers. In this thesis, we propose a second-order accurate numerical method for solving the convection-diffusion equation by using a gradient-limited Godunov-type convective flux and the multi-point flux approximation (MPFA) L-Method for the diffusion flux. We applied our solver towards simulation of a nitric oxide-releasing intravascular catheter.

Intravascular catheters are essential for long-term vascular access in both diagnosis and treatment. Use of catheters are associated with risks for infection and thrombosis. Because infection and thrombosis lead to impaired flow and potentiality life threatening systemic infections, this leads to increased morbidity and mortality, requiring catheters to be replaced among other treatments for these complications. Nitric oxide (NO) is a potent antimicrobial and antithrombotic agent produced by vascular endothelial cells. The production level in vivo is so low that the physiological effects can only be seen around the endothelial cells. The catheter can incorporate

a NO source in two major ways: by impregnating the catheter with NO-releasing compounds such as S-nitroso-N-acetyl penicillamine (SNAP) or using electrochemical reactions to generate NO from nitrites. We applied our solver to both situations to guide the design of the catheter. Simulations revealed that dissolved NO inside the catheter is depleted after 12 minutes without resupplying, and electrochemical release of NO requires 10.5 minutes to reach steady state.

Lung edema is often present in patients with end-stage renal disease due to reduced filtration functions of the kidney. These patients require regular dialysis sessions to manage their fluid status. The clinical gold standard to quantify lung edema is to use CT, which exposes patients to high amounts of radiation and is not cost efficient. Fluid management in such patients becomes very challenging without a clear guideline of fluid to be removed during dialysis sessions. Hypotension during dialysis can limit fluid removal, even in the setting of ongoing fluid overload or congestive heart failure. Accurate assessment of the pulmonary fluid status is needed, so that fluid overload and congestive heart failure can be detected, especially in the setting of hypotension, allowing dialysis to be altered to improve fluid removal.

Recently, reverberations in ultrasound signals, referred to as "lung comets" have emerged as a potential quantitative way to measure lung edema. Increased presence of lung comets is associated with higher amounts of pulmonary edema, higher mortality, and more adverse cardiac events. However, the lung comets are often counted by hand by physicians with single frames in lung ultrasound and high subjectivity has been found to exist among the counting by physicians. We applied image processing and neural network techniques as an attempt to provide an objective and accurate measurement of the amount of lung comets present. Our quantitative results are significantly correlated with diastolic blood pressure and ejection fraction.

Part 1

Computer Simulation of a Nitric Oxide-Releasing Catheter with a Novel Stable Convection-Diffusion Equation Solver

Chapter I

Introduction

In this section, we will first introduce the theoretical background, and then the background of the specific applications.

1.1 Theory: Mass Transport with Boundary of Flow

Three major phenomena are involved in the transport of molecules: diffusion, convection, and reaction. Diffusion is the random motion of molecules from thermal energy transferred by molecular collisions [1]. Convection is transport from movement of bulk fluids [1]. Reaction is a process that results in the interconversion of chemical species [2] and can affect the concentration of certain molecules.

Biological transport also follows these principles, although many additional challenges arise, such as that the flow field may be complex [3], biological barriers may impede the process of transport [4], and the transported molecules may be snatched by binding proteins in the body [5]. One situation has been under-addressed is the transport involving a boundary of flow, or a discontinuous flow field.

Mass transport involving a boundary of flow is common in blood-contacting medical devices. Accurately resolving the mass transport phenomenon is important to understand drug delivery and chemical leaching in these devices. When placed *in vivo*, mass transport within and outside these devices depict two different situations

of mass transport: no flow exists within the biocompatible polymer (or other material) that is used to manufacture this device so that the mass transport is restricted to diffusion; all of convection, diffusion, and reaction is involved in bloodstream due to blood flow and interaction with other molecules. Depending on the relative strength of the convection and reaction with respect to diffusion, the concentration of a molecule may drop sharply at the interface, creating a sharp concentration gradient.

Real concentration levels are rarely captured accurately in animal models *in vivo* due to the following reasons. The corresponding real-time sensor for the specific molecule may not be available for *in vivo* use. Even if such a sensor exists, the insertion of such a sensor can largely affect the flow field in the bloodstream, which means that the concentration measured can be different from the concentration in the intended use case. In addition, animal studies incur various costs, including monetary costs to purchase and host the animals, time for researchers to complete the animal studies, and ethical costs with the test procedures [6].

Computational modeling has captured increased presence in guiding the designs of medical devices and is being actively recommended by the Food and Drug Administration (FDA) [7]. When the solution contains a large gradient, or "shock", however, the solution is often unstable and overshoots or undershoots can happen. Proper shock capturing methods are needed to accurately resolve shocks in the system. Biological systems typically involve complex geometries and solvers capable of handling higher dimensions, especially in 3D is necessary. No existing literature has demonstrated a method for stable numerical solutions of the convection-diffusion equation in domains containing a boundary of flow. There exists a clear need for such a solver to be developed to accurately resolve the concentration in such domains, es-

pecially for the use case below, a nitric oxide (NO)-releasing catheter. After a proper scheme for the convection-diffusion equation is deduced and implemented, the reaction term can be implemented as an additional local source term to complete the simulation of all three transport processes mentioned above.

1.2 Use Case: A Nitric Oxide-Releasing Catheter

Blood-contacting medical devices carry risks of thrombosis and infection [8], and intravascular catheters are no exception. Being a foreign material to the body, the catheter polymer can activate the coagulation pathway and cause blood clots to form around the catheter [9]. Venous thrombosis is very common from catheterization and can happen in 6 to 67% of patients [10] and may result in pulmonary embolism, catheter malfunction, and/or post-thrombotic syndrome [10, 11]. In addition, various strains of bacteria can form biofilms on the surface of the catheter [12, 13]. A biofilm is a population of bacteria growing in a polysaccharide matrix. Bacteria contained in biofilm gain increased antimicrobial resistance and can cause infections [14]. The incidence of catheter-related infections is estimated to be about 3.9 per 1000 line days and each incidence can cost on average $33000 to $75000 depending on the situation [15]. Catheter-related infections involving one group of catheters, the central venous catheters are estimated to place a burden of $1.85 billion in US every year alone [16]. The risk factors also have a synergistic effect: the risk of a patient to get deep vein thrombosis is 17.6× higher if they got a catheter-related infection [10]. The risks of having a catheter-related infection increase significantly after 5 to 7 days of catheterization [17], limiting the service life of the catheters.

There are multiple strategies to manage formation of thrombi and biofilms in clinical and research settings. Besides keeping hygienic practices and replacing impacted

catheters (which are associated with additional complications) [18], modifications to the catheters and concurrent procedures have been proposed to limit the risks. Current clinical practice to manage thrombosis is to use systemic anticoagulant delivery, the most common being heparin [19]. Systemic use of heparin are associated with risks of thrombocytopenia, hemorrhage, and arterial embolism [20]. Local deliveries are preferred, such as using heparin coating or covalent-linked heparin, but irreversible side effects can still happen [21] and the release kinetics do not support continuous use of more than one week [22]. Management of infection involves using antibiotic or antiseptic coating on the catheters or as locking solutions. Antimicrobial or antiseptic coating are effective in reducing infection rates, but not as effective to prevent severe infections such as sepsis [23]. Use of antibiotics are associated with reports of antibiotic resistance which carries serious complications, especially when the antibiotic used is vancomycin [24]. The evidence of using antiseptic coating, such as chlorhexidine-silver, is inconclusive, and *in vitro* studies to induce bacterial resistance to antiseptics has been successful [25].

NO is a potent antibacterial and antithrombotic agent [26, 27]. The presence of NO is natural to the body, as the vascular endothelial cells releases a small amount of NO to regulate vasodilation and prevent adhesion of platelets to the vessel wall [27]. Use of NO in catheters is challenging, however, since the half-life of NO in blood is short and is estimated to be in the millisecond to second range [28, 29], the surface of the catheter might be too far for NO to reach. Therefore, catheters that use NO as the antibacterial and antithrombotic agent will have to carry their own NO source. Various strategies of NO release from catheters are being researched, but this thesis will focus on two methods: impregnating the catheter with a NO-releasing compound, S-Nitroso-N-acetylpenicillamine (SNAP) into a variety of biocompatible

polymers [30, 31, 32], or using electrochemically modulated NO release from nitrites [33, 34]. We will simulate NO release from these two configurations using the novel convection-diffusion solver we developed.

1.3 Organization of Part 1

Part 1 of this thesis is organized as follows:

- Chapter II (A Second Order Stable Solver for the Convection-Diffusion Equation in Domains with Boundaries of Flow) will focus on delivering the numerical methods for the novel convection-diffusion equation solver. This solver is a finite volume method (FVM)-based solver and is formulated for both 2D and 3D using a body-fitted grid. The convection part of the equation is solved by a Godunov-type scheme and the diffusion fluxes by a multi-point flux approximation (MPFA) method. The solvers are verified to have second order accuracy. Implementations of the solvers will be briefly covered.
- Chapter III (Simulation Results of a Nitric Oxide-Releasing Catheter) will focus on applying the solver to two catheter configurations: catheters impregnated with a NO source, and catheters that release NO electrochemically. The possible implications of the simulated results will be discussed.
- Chapter IV (Conclusion and Future Directions) summarizes the overall results, discusses the potential limitations of the current work and provide guidance to future work.

Bibliography

[1] G. A. Truskey, F. Yuan, and D. F. Katz, *Transport phenomena in biological systems, 2nd edition*. Pearson/Prentice Hall Upper Saddle River, NJ, USA:, 2009.

[2] P. Muller, "Glossary of terms used in physical organic chemistry (iupac recommendations 1994)," *Pure and Applied Chemistry*, vol. 66, no. 5, pp. 1077–1184, 1994.

[3] S. R. Lynch, N. Nama, J. Zu, C. J. Arthurs, O. Sahni, and C. A. Figueroa, "Numerical considerations for advection-diffusion problems in cardiovascular hemodynamics," *arXiv preprint arXiv:1910.08165*, 2019.

[4] M. Ferrari, "Frontiers in cancer nanomedicine: directing mass transport through biological barriers," *Trends in biotechnology*, vol. 28, no. 4, pp. 181–188, 2010.

[5] W. M. Pardridge, "Transport of protein-bound hormones into tissues in vivo," *Endocrine reviews*, vol. 2, no. 1, pp. 103–123, 1981.

[6] K. Weil, *Thinking animals: Why animal studies now?* Columbia University Press, 2012.

[7] T. M. Morrison, M. L. Dreher, S. Nagaraja, L. M. Angelone, and W. Kainz, "The role of computational modeling and simulation in the total product life cycle of peripheral vascular devices," *Journal of medical devices*, vol. 11, no. 2, 2017.

[8] M. C. Frost, M. M. Reynolds, and M. E. Meyerhoff, "Polymers incorporating nitric oxide releasing/generating substances for improved biocompatibility of blood-contacting medical devices," *Biomaterials*, vol. 26, no. 14, pp. 1685–1693, 2005.

[9] A. Barzaghi, M. Dell'Orto, A. Rovelli, C. Rizzari, A. Colombini, and C. Uderzo, "Central venous catheter clots: incidence, clinical significance and catheter care in patients with hematologic malignancies," *Pediatric hematology and oncology*, vol. 12, no. 3, pp. 243–250, 1995.

[10] C. J. van Rooden, M. E. Tesselaar, S. Osanto, F. R. Rosendaal, and M. V. Huisman, "Deep vein thrombosis associated with central venous catheters–a review," *Journal of Thrombosis and Haemostasis*, vol. 3, no. 11, pp. 2409–2419, 2005.

[11] M. Horattas, D. Wright, A. Fenton, D. Evans, M. Oddi, R. Kamienski, and E. Shields, "Changing concepts of deep venous thrombosis of the upper extremity–report of a series and review of the literature.," *Surgery*, vol. 104, no. 3, pp. 561–567, 1988.

[12] I. I. Raad, M. F. Sabbagh, K. H. Rand, and R. J. Sherertz, "Quantitative tip culture methods and the diagnosis of central venous catheter-related infections," *Diagnostic microbiology and infectious disease*, vol. 15, no. 1, pp. 13–20, 1992.

[13] T. Elliott, H. Moss, S. Tebbs, I. Wilson, R. Bonser, T. Graham, L. Burke, and M. Faroqui, "Novel approach to investigate a source of microbial contamination of central venous catheters," *European Journal of Clinical Microbiology and Infectious Diseases*, vol. 16, no. 3, pp. 210–213, 1997.

[14] K. Lewis, "Riddle of biofilm resistance," *Antimicrobial agents and chemotherapy*, vol. 45, no. 4, pp. 999–1007, 2001.

[15] C. S. Hollenbeak, "The cost of catheter-related bloodstream infections: implications for the value of prevention," *Journal of Infusion Nursing*, vol. 34, no. 5, pp. 309–313, 2011.

[16] E. Zimlichman, D. Henderson, O. Tamir, C. Franz, P. Song, C. K. Yamin, C. Keohane, C. R. Denham, and D. W. Bates, "Health care–associated infections: a meta-analysis of costs and financial impact on the us health care system," *JAMA internal medicine*, vol. 173, no. 22, pp. 2039–2046, 2013.

[17] D. C. McGee and M. K. Gould, "Preventing complications of central venous catheterization," *New England journal of medicine*, vol. 348, no. 12, pp. 1123–1133, 2003.

[18] N. P. O'grady, M. Alexander, L. A. Burns, E. P. Dellinger, J. Garland, S. O. Heard, P. A. Lipsett, H. Masur, L. A. Mermel, M. L. Pearson, *et al.*, "Guidelines for the prevention of intravascular catheter-related infections," *Clinical infectious diseases*, vol. 52, no. 9, pp. e162–e193, 2011.

[19] M. B. Gorbet and M. V. Sefton, "Biomaterial-associated thrombosis: roles of coagulation factors, complement, platelets and leukocytes," *Biomaterials*, vol. 25, no. 26, pp. 5681–5703, 2004.

[20] R. E. WEISMANN and R. W. TOBIN, "Arterial embolism occurring during systemic heparin therapy," *AMA archives of surgery*, vol. 76, no. 2, pp. 219–227, 1958.

[21] J. Laster and D. Silver, "Heparin-coated catheters and heparin-induced thrombocytopenia," *Journal of vascular surgery*, vol. 7, no. 5, pp. 667–672, 1988.

[22] Y. Wo, *S-Nitroso-N-acetylpenicillamine (SNAP)-Based Antithrombotic and Antimicrobial Polymers for Biomedical Applications: Nitric Oxide (NO) to the Rescue*. PhD thesis, 2017.

[23] S. Tennenberg, M. Lieser, B. McCurdy, G. Boomer, E. Howington, C. Newman, and I. Wolf, "A prospective randomized trial of an antibiotic-and antiseptic-coated central venous catheter in the prevention of catheter-related infections," *Archives of Surgery*, vol. 132, no. 12, pp. 1348–1351, 1997.

[24] D. Yahav, B. Rozen-Zvi, A. Gafter-Gvili, L. Leibovici, U. Gafter, and M. Paul, "Antimicrobial lock solutions for the prevention of infections associated with intravascular catheters in patients undergoing hemodialysis: systematic review and meta-analysis of randomized, controlled trials," *Clinical infectious diseases*, vol. 47, no. 1, pp. 83–93, 2008.

[25] L. A. Mermel, "Prevention of intravascular catheter–related infections," *Annals of internal medicine*, vol. 132, no. 5, pp. 391–402, 2000.

[26] N. Barraud, M. V. Storey, Z. P. Moore, J. S. Webb, S. A. Rice, and S. Kjelleberg, "Nitric oxide-mediated dispersal in single-and multi-species biofilms of clinically and industrially relevant microorganisms," *Microbial biotechnology*, vol. 2, no. 3, pp. 370–378, 2009.

[27] J. Freedman and J. Loscalzo, "Nitric oxide and its relationship to thrombotic disorders," *Journal of Thrombosis and Haemostasis*, vol. 1, no. 6, pp. 1183–1188, 2003.

[28] T. Hakim, K. Sugimori, E. Camporesi, and G. Anderson, "Half-life of nitric oxide in aqueous solutions with and without haemoglobin," *Physiological measurement*, vol. 17, no. 4, p. 267, 1996.

[29] X. Liu, M. J. Miller, M. S. Joshi, H. Sadowska-Krowicka, D. A. Clark, and J. R. Lancaster, "Diffusion-limited reaction of free nitric oxide with erythrocytes," *Journal of biological chemistry*, vol. 273, no. 30, pp. 18709–18713, 1998.

[30] E. J. Brisbois, H. Handa, T. C. Major, R. H. Bartlett, and M. E. Meyerhoff, "Long-term nitric oxide release and elevated temperature stability with s-nitroso-n-acetylpenicillamine (snap)-doped elast-eon e2as polymer," *Biomaterials*, vol. 34, no. 28, pp. 6957–6966, 2013.

[31] Y. Wo, E. J. Brisbois, J. Wu, Z. Li, T. C. Major, A. Mohammed, X. Wang, A. Colletta, J. L. Bull, A. J. Matzger, *et al.*, "Reduction of thrombosis and bacterial infection via controlled nitric oxide (no) release from s-nitroso-n-acetylpenicillamine (snap) impregnated carbosil intravascular catheters," *ACS biomaterials science & engineering*, vol. 3, no. 3, pp. 349–359, 2017.

[32] X. Wang, A. Jolliffe, B. Carr, Q. Zhang, M. Bilger, Y. Cui, J. Wu, X. Wang, M. Mahoney, A. Rojas-Pena, *et al.*, "Nitric oxide-releasing semi-crystalline thermoplastic polymers: preparation, characterization and application to devise anti-inflammatory and bactericidal implants," *Biomaterials science*, vol. 6, no. 12, pp. 3189–3201, 2018.

[33] B. K. Oh and M. E. Meyerhoff, "Catalytic generation of nitric oxide from nitrite at the interface of polymeric films doped with lipophilic cu (ii)-complex: a potential route to the preparation of thromboresistant coatings," *Biomaterials*, vol. 25, no. 2, pp. 283–293, 2004.

[34] K. K. Konopińska, N. J. Schmidt, A. P. Hunt, N. Lehnert, J. Wu, C. Xi, and M. E. Meyerhoff, "Comparison of copper (ii)–ligand complexes as mediators for preparing electrochemically modulated nitric oxide-releasing catheters," *ACS applied materials & interfaces*, vol. 10, no. 30, pp. 25047–25055, 2018.

Chapter II

A Second Order Stable Solver for the Convection-Diffusion Equation in Domains with Boundaries of Flow

2.1 Introduction

Biological transport often involves domains including interfaces separating the presence of flow. Such is the case for transport in blood-contacting medical devices. Our interest is in designing a nitric oxide (NO) releasing intravascular catheter that releases NO from either S-nitroso-N-acetyl penicillamine (SNAP) crystals impregnated inside the catheter polymer [1, 2] or an electrochemical source that generates NO from nitrites [3]. Transport of nitric oxide involves three main routes, convection, diffusion, and reaction, as visualized in Figure 2.1. Convection transports NO with blood flow; diffusion preferably transport NO down the concentration gradient; reaction generates or consumes NO chemically.

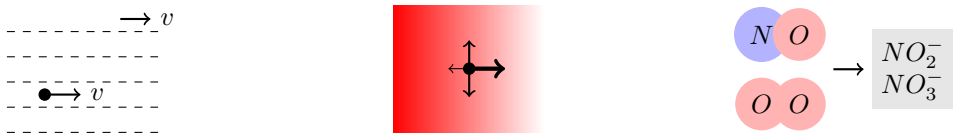

(a) Convection (b) Diffusion (c) Reaction

Figure 2.1: Three main mass transport routes: convection, diffusion, and reaction, visualized with nitric oxide as an example molecule.

In both methods of NO generation, NO is transported out of the solid phase of the catheter polymer through pure diffusion and meets blood flow. The abrupt addition

of convection to the transport quickly depletes NO and creates a large concentration gradient ("shock"), leading to negative and unstable solutions from commercial simulation packages during our early attempts, even with added numerical stabilization and without considerations for further depletion of NO by reaction. Negative solutions appear due to the nature of solving a differential equation numerically in a discrete domain. A proper numerical scheme is needed to accurately capture the shock and resolve the concentration profile of NO around the boundaries of flow. The developed numerical scheme would be applicable to other simulation problems involving a boundary of flow, especially in biology-inspired domains.

2.2 Convection-Diffusion Equation and Historical Discretization Efforts

Our numerical method is derived for the convection-diffusion equation that governs the mass transport for dilute species. The applicable form is shown in equation (2.1):

$$\frac{\partial c}{\partial t} = \nabla \cdot (\boldsymbol{K} \nabla c) - \nabla \cdot (\boldsymbol{v} c) + R, \tag{2.1}$$

where c is the concentration, t is the time, $\boldsymbol{K}$ is the permeability tensor, $\boldsymbol{v}$ is the velocity, and R is the rate of reaction. We will not consider the reaction term for the development of this solver, since reaction rates do not need special spatial discretization. In addition, we assume incompressibility in the flow field, which is typically true for liquid-phase flows. Often in homogeneous domains, the permeability tensor can be written as the diffusion coefficient D times the identity matrix $\boldsymbol{I}$:

$$\boldsymbol{K} = D\boldsymbol{I}. \tag{2.2}$$

After these simplifications, our convection-diffusion equation takes the following simplified form:

$$\frac{\partial c}{\partial t} = \nabla \cdot (D \nabla c) - \boldsymbol{v} \cdot \nabla c. \tag{2.3}$$

We need to discretize this equation 2.3 so that we can solve this equation numerically. The need for discretizing the convection-diffusion equation is unique that the equation 2.3 contains a first and a second order spatial derivative term, and the numerical methods will need to be able to handle both derivative terms. No existing numerical schemes have been formulated to solve the convection-diffusion equation in domains containing flow boundaries. However, some numerical schemes for the convection-diffusion equation exist and claims stability of the solution. We only consider second or higher order schemes due to the excessive need of fineness of the mesh to produce acceptable results using first-order accurate schemes. We will also restrict our discussion in formulations that are available in higher dimensions, as in 2D and 3D.

Most discretization strategies fall into one of two categories: finite element methods (FEM) and finite volume methods (FVM). Among finite element methods, discontinuous Galerkin methods are naturally formulated to solve for first-order differentials (hyperbolic) and the continuous Galerkin methods typically designed for second-order differentials (parabolic) [4]. Since FEM methods are designed to handle either differential, additional stabilization for the other differential is needed, such as Bassi-Rebay schemes BR1 [5] / BR2 [6] and internal penalty [7] methods for discontinuous Galerkin, and streamline upwind Petrov-Galerkin (SUPG) methods [8] for continuous Galerkin methods. Recently, Lynch et al. have proposed a SUPG method with additional shock capturing formulations to stabilize the oscillations near Neumann boundaries and obtained satisfactory results for Péclet numbers

up to 1.5×10^4 [9]. Finite element methods are typically more flexible in configuring for higher dimensions or higher orders of accuracy, but experimental parameters are often involved in stabilizing the solution and some FEM formulations can be computationally expensive.

Finite volume methods are less flexible on the orders of accuracy, but typically provides stabilization without the need for parameter tuning and occasionally accompanied by mathematically proven stability on one-dimension. Individual schemes for diffusion and convection can be chosen and combined to solve the whole equation. Higher-order upwind schemes, including approximate Riemann solvers such as the Roe solver [10] have be historically used, but the central schemes have received abundant attention due to their simpler formulations and lower computational costs without the need to solve for eigenvalue problems associated with Riemann solvers [11]. Early central schemes only offered directional-splitting extensions onto Cartesian grids [12]. Some schemes are further extended to be used in 3D unstructured tetrahedral grids, such as the Nessyahu-Tadmor Scheme [13].

All these solvers, however, do not satisfy the needs for simulating mass transport in discontinuous flow fields. Meshing of the domain is in at least 2D, but typically 3D and generally not on a Cartesian grid, where nodes are evenly placed on the x, y, and z axis on Cartesian coordinates. Combining cut cell methods with directional splitting of 1D schemes is challenging due to the cut cell methods generally have trouble handling a variety of boundary conditions [14]. Body-fitted grids typically require hexahedral elements to be padded around the boundary layers to accurately resolve the effects around them. To accurately solve the convection-diffusion equation in a domain containing a boundary of flow, we need a new numerical scheme.

2.3 Description of Our Numerical Scheme

Our numerical scheme is developed in Cartesian coordinates to allow complex domain configurations. Transport across solid-liquid interfaces creates diffusive boundary layers [15]. Inspired by the use of hexahedral elements in flow simulations [16], we use a single type of elements, quadrilateral for 2D and hexahedral for 3D, to construct a body-fitted mesh over the simulation domain to accurately resolve the boundary layers and to simplify the numerical methods. To solve the system, the diffusive flux, corresponding to the $\nabla \cdot (D\nabla c)$ term and the convective flux, corresponding to the $\boldsymbol{v} \cdot \nabla c$ term, need to be formulated numerically for quadrilateral and hexahedral mesh elements. Our formulation of the numerical fluxes falls into the family of FVM and is second order accurate.

The Kurganov-Tadmor (K-T) central scheme [12] is a second-order, Godonov-type, and Riemann-free solver for the convection-diffusion equation, but the scheme was developed on 1D domain and only extended to higher dimensions for Cartesian grids by directional splitting. A piecewise linear approximation is performed for each cell to achieve second-order accuracy. The authors used generalized minmod gradient limiting to achieve convective fluxes satisfying the property of total variation diminishing (TVD) for guaranteed stability. The diffusion flux is calculated using a two-point flux approximation (TPFA) method from two adjacent cells. For 2D and 3D meshes, calculating and limiting the gradient is not as straightforward as in 1D because the cell centers of three adjacent cells may not lie on a straight line. This situation is illustrated in Figure 2.2. The TPFA diffusion flux may contain mesh-independent $O(1)$ error since $\boldsymbol{K}$-orthogonality may not hold in general meshes [17]. This situation is shown in Figure 2.3.

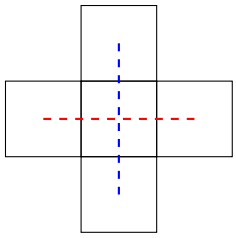

(a) A five-element stencil in a Cartesian grid

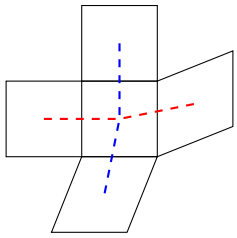

(b) Elements in general grids

Figure 2.2: An example in 2D: challenge in generating gradients for piecewise linear approximation in general meshes. Four estimates of the gradients within the central cell can be generated using four neighboring elements. In a Cartesian grid, two estimates (red) only contain the x-component of the gradient and can form an estimate for the x component after a gradient limiter; the y-estimate follows the same pattern (blue). In a general grid, all four estimates may contain both x and y-components and cannot be easily paired or limited to generate the gradient of a certain direction.

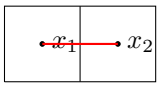

(a) $\boldsymbol{K}$-orthogonal

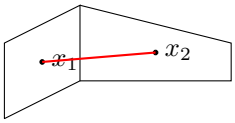

(b) Not $\boldsymbol{K}$-orthogonal

Figure 2.3: An example in 2D: when mesh-independent errors arise. Assuming isotropic diffusion $\boldsymbol{K} = D\boldsymbol{I}$, $\boldsymbol{K}$-orthogonality reduces to the orthogonality of the line connecting the cell centers x_1, x_2 with respect to the face. In a Cartesian grid, the $\boldsymbol{K}$-orthogonality is always satisfied for isotropic diffusion. This is not necessarily the case in general meshes. Mesh-independent errors will be present in the solution for more general meshes.

Our solution is to use a larger flux stencil for calculating the convection fluxes and use the multi-point flux approximation (MPFA) to calculate the diffusion fluxes. Below, we will present our extension of the K-T scheme to 2D and 3D for quadrilateral and hexahedral meshes.

2.4 The 2D Stable Numerical Scheme

The core of our extension is to find a proper convection stencil that enables us to calculate the gradients for the piecewise linear reconstruction during the calculation of the convective flux, and an accurate diffusion scheme that can replace the TPFA method used in the K-T scheme [12].

2.4.1 Convective Flux

The conservation element and solution element scheme, a separate scheme for Euler's equations, was extended to quadrilateral and hexahedral elements by Zhang et al. [18] by using a 5-element (2D) and 7-element (3D) stencil. The 2D stencil was then adapted by Huynh [19] with simplified expressions for gradient calculations in central schemes for convection equations. We will present our modification to Huynh's extension to allow arbitrary use of gradient limiters.

As illustrated in Figure 2.2, we have four estimates for the gradients in possibly four directions, so we need to formulate appropriate directions of gradients so that we can pair up two estimates and limit the gradients. A five-element stencil is constructed with the central element and its four immediate neighbors, as shown in Figure 2.4. The new element is an octagon, made up of four vertices of the central element $V_{1\ldots4}$ and the cell centers of the neighboring elements $O_{1\ldots4}$. Reconstruction of the new elements is performed for all elements within the domain. For this stencil shown in Figure 2.4, we denote the cell centers of the reconstructed elements of the neighboring cells to be $O^*_{1\ldots4}$, to differentiate from their original cell centers $O_{1\ldots4}$. The neighboring elements are then split into two pairs, "left (1) - right (2)" and "up (3) - down (4)".

We first need to find new cell values of the octagon elements. This is found by using a volume-weighed average, as shown in equation (2.4).

$$c_{O_0^*} = \frac{c_{O_0}A_{V_1V_2V_3V_4} + c_{O_1}A_{V_1V_4O_1} + c_{O_2}A_{V_2V_3O_2} + c_{O_3}A_{V_1V_2O_3} + c_{O_4}A_{V_3V_4O_4}}{A_{V_1V_2V_3V_4} + A_{V_1V_4O_1} + A_{V_2V_3O_2} + A_{V_1V_2O_3} + A_{V_3V_4O_4}}, \tag{2.4}$$

where c_{O_i} denotes the cell value of the original element with cell center O_i for $i = 0\ldots4$ and A denotes the area enclosed by the vertices in the subscript. Piecewise

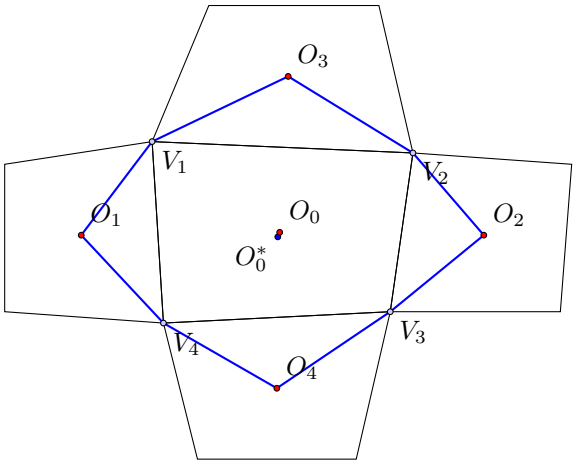

Figure 2.4: A central quadrilateral cell and its four immediate members. An "octagon" element is constructed by joining the vertices of the original element $V_{1\ldots4}$ with the neighboring cell centers $O_{1\ldots4}$. The cell center of the original element is O_0 and the cell center of the octagon element is O_0^*.

linear reconstruction takes place in each octagon cell with the following expression:

$$c(\vec{x}) = c_{O_0^*} + \nabla c \cdot (\vec{x} - \vec{x}_{O_0^*}). \tag{2.5}$$

Each pair of the neighboring cells will contribute one component to the gradients ∇c. Since O_0^* is the cell center of the new cell, O_1O_2 and O_3O_4 must pass through O_0^*. Therefore, we obtain an approximate direction of the gradient for each pair. For example, equation (2.6) demonstrates the calculation of the left gradient with unit vector $\vec{n}_{lr}$. We can use the same procedure to find the right, up, and down gradients.

$$\nabla c_{left} = (c_{O_0^*} - c_{O_1^*}) \frac{\overrightarrow{O_0^*O_1}}{|\overrightarrow{O_0^*O_1}|} = (c_{O_0^*} - c_{O_1^*}) \vec{n}_{lr}. \tag{2.6}$$

To obtain stable solutions and proper gradient estimates, we apply gradient limiters to the two gradients obtained in a pair. Without loss of generality, we assume the flow is from left to right. Therefore, the left element is an upstream element and the right element is downstream. The gradient limiting takes the following form as in equation (2.7) and can be similarly calculated for the up/down pair.

$$r_{lr} = \frac{\text{Upstream Gradient}}{\text{Downstream Gradient}} = \frac{\nabla c_{left}}{\nabla c_{right}}; \quad \nabla c_{lr} = g(r_{lr}) \nabla c_{right} \vec{n}_{lr}. \tag{2.7}$$

The flux limiter function $g(r)$ is generally chosen by the person who is performing the simulation, but a total variation diminishing (TVD) limiter is generally used for stability. See Section 2.6.1 for the gradient limiters we picked for our solver.

The unit vectors $\vec{n}$ are not necessarily the unit vectors for 2D Cartesian coordinates $\hat{x}$ and $\hat{y}$, so a Jacobian matrix is necessary to transform these gradients to the Cartesian coordinates:

$$\boldsymbol{J} = \begin{bmatrix} \vec{n}_{lr,x} & \vec{n}_{ud,x} \\ \vec{n}_{lr,y} & \vec{n}_{ud,y} \end{bmatrix}; \quad \begin{bmatrix} \nabla_{c,x} \\ \nabla_{c,y} \end{bmatrix} = \boldsymbol{J} \begin{bmatrix} \nabla c_{lr} \\ \nabla c_{ud} \end{bmatrix}, \tag{2.8}$$

We now use the semi-discrete K-T formulation [12] of the convective flux f shown in equation (2.9). The edge states c_+ and c_- are calculated at the shared edge center from the upstream and the downstream element using equation (2.4) with the gradients calculated from the previous step.

$$a = \vec{n} \cdot \boldsymbol{v}; \quad f = \frac{a}{2}(c_- + c_+) - \frac{|a|}{2}(c_+ - c_-). \tag{2.9}$$

Huynh's approximation of the gradients is a less flexible version of our extension with a van Albada 1 limiter [19]. Our method reduces to the directional splitting method by Kurganov et al. [12] on a Cartesian grid. TVD stability is guaranteed for Cartesian grids with any TVD limiter.

2.4.2 Diffusive Flux

We coupled our convection scheme with an existing diffusion scheme for general quadrilateral meshes, the multi-point flux approximation (MPFA) L-method. The MPFA scheme is a family of methods that use an expanded stencil to satisfy the $\boldsymbol{K}$-orthogonality required to obtain accurate solutions for diffusion [20]. The method we are using is a relative compact scheme within the MPFA scheme, the L-method [21].

The L-method is unique in such a way that each edge is split down the middle and the flux across half edges are calculated. A four-element stencil is used for calculating the flux across each half edge, as shown in Figure 2.5.

(a) Stencil 1 (b) Stencil 2

Figure 2.5: Two possible stencils for 2D MPFA L-Scheme. These stencils are for diffusion flux across the blue, bolded half edge. Each stencil spans three elements and is highlighted in red. The nodes making up the stencil, marked with small circles, are centers of the corresponding element or edge.

The derivation of the fluxes will be omitted in this thesis as it is covered in detail in Aavatsmark et al. [21]. We will simply give an expression for Stencil 2 in Figure 2.5. The definition of the normal vectors can be found in the following Figure 2.6.

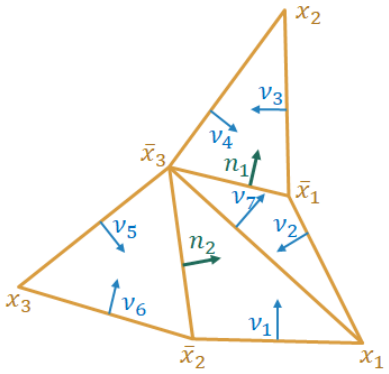

Figure 2.6: Definitions for the normal vectors in Stencil 2 of the MPFA L-Scheme. Tht total number of normal vectors is 9, including $\vec{n}_{1,2}$ and $\vec{v}_{1\ldots7}$. These normal vectors have magnitudes equal to the length of the corresponding edge. $x_{1,2,3}$ are cell centers of the corresponding cells; $\bar{x}_{1,2}$ are edge centers; $\bar{x}_3$ is the common node of the cells inside the stencil.

We need to define these additional quantities to obtain our expression for the diffusion flux [21]:

$$\boldsymbol{R} = \begin{bmatrix} 0 & 1 \\ -1 & 0 \end{bmatrix}; \quad T_j = \vec{\nu}_{2j-1}^T \vec{\nu}_{2j}; \quad \omega_{ijk} = \frac{1}{T_j} \vec{n}_i^T D_j \vec{\nu}_k; \quad \chi_{ijk} = \frac{1}{T_j} \vec{\nu}_i^T \boldsymbol{R} \vec{\nu}_k. \tag{2.10}$$

to write our expression for the transmissibility matrix $\boldsymbol{T}$ to obtain the flux vector $\boldsymbol{f}$ as in equation (2.11)

$$\boldsymbol{T}\boldsymbol{u} = \boldsymbol{f}; \quad \boldsymbol{T} = \boldsymbol{C}\boldsymbol{A}^{-1}\boldsymbol{B} + \boldsymbol{D}, \tag{2.11}$$

where [21]:

$$\begin{aligned}
\boldsymbol{A} &= \begin{bmatrix} \omega_{111} - \omega_{124} - \omega_{123}\chi_{711} & \omega_{112} - \omega_{123}\chi_{712} \\ \omega_{211} - \omega_{236}\chi_{711} & \omega_{212} - \omega_{235} - \omega_{236}\chi_{712} \end{bmatrix} \\
\boldsymbol{B} &= \begin{bmatrix} \omega_{111} + \omega_{112} + \omega_{123}(1 - \chi_{711} - \chi_{712}) & -\omega_{123} - \omega_{124} & 0 \\ \omega_{211} + \omega_{212} + \omega_{236}(1 - \chi_{711} - \chi_{712}) & 0 & -\omega_{235} - \omega_{236} \end{bmatrix} \\
\boldsymbol{C} &= \begin{bmatrix} -\omega_{111} & -\omega_{112} \\ -\omega_{211} & -\omega_{212} \end{bmatrix} \\
\boldsymbol{D} &= \begin{bmatrix} \omega_{111} + \omega_{112} & 0 & 0 \\ \omega_{211} + \omega_{212} & 0 & 0 \end{bmatrix}.
\end{aligned} \tag{2.12}$$

The resulting flux vector $\boldsymbol{f}$ from (2.11) has two components, $\boldsymbol{f} = [f_1 \ f_2]^T$. Our target in Stencil 2 is the edge with unit vector $\vec{n}_2$ as shown in Figure 2.5 and we take f_2 to be the diffusive flux across the edge. Both Stencil 1 and 2 generates a flux for the highlighted edge; we select the stencil that has smaller transmissibility from the central cell to the other cell across this edge according to the $\boldsymbol{T}$ matrix. [21]

2.4.3 Simulation and Verification

The only boundary condition we implemented in the 2D solver is the periodic boundary condition. We used the Dormand-Prince [22] as the time stepping method.

First, we used a convection problem to test the shock capturing capabilities of our solver. In a square 1×1 domain with periodic boundary conditions, the initial concentration is $c(t = 0) = (x > 0.5)$. Discontinuities are located at $x = 0.5$ and

$x = 1.0$ (0.0). The velocity field is $\boldsymbol{v} = [0.1\ 0.0]^T$ and the diffusion coefficient D is 0 everywhere. The mesh is a uniform mesh perturbed by up to 10% of its length. The results are shown in Figure 2.7 showing the solutions at $t = 0$, 5, 10. We can see that the shock is retained quite well and no overshoot or negative concentrations occurred.

Next, we tested the solver for performance in diffusion. On a 1×1 grid with periodic boundary conditions, we used a Gaussian wave $c(t = 0) = e^{-\frac{(x-0.5)^2+(y-0.5)^2}{0.004}}$ as the initial condition and a diffusion coefficient of $D = 10^{-3}$. No velocity field is applied and we are using the same mesh as in the above case. The results are shown in Figure 2.8 showing the "spreading-out" behavior expected from diffusion.

We then added diagonal convection to the above diffusion problem such that the Gaussian wave is transported back to the original position after $t = 1$, which means that $\boldsymbol{v} = [1.0\ 1.0]^T$. We used a van Albada 1 filter in this case to stabilize convection. The structure of the Gaussian wave is retained quite well and the solution is stable, as shown in Figure 2.9.

We also tested a few other problems with the 2D solver and tested for convergence rates of the solver. We used the 1-norm of the difference between the theoretical and the actual results, integrated through the whole domain, as the error measure:

$$error = \int_0^1 \int_0^1 ||c_{exact} - c_{actual}||_1 dA. \tag{2.13}$$

The convergence rates of the 1-norm error ranges from 0.98 to 1.82 in the situations depicted below in Figure 2.10. There are four types of studies, including three situations we mentioned above, and a pure convection of a sine wave. The tests are run on a uniform mesh or a perturbed uniform mesh, giving eight total studies. The solver readily achieved second-order accuracy on most problems except on the 1-norm of convection of a shock on a uniform mesh, which is an expected behavior

when the solution contains a shock.

These test problems have shown good shock-capturing abilities of our solver and acceptable orders of accuracy and pave the way for us to extend the scheme to 3D.

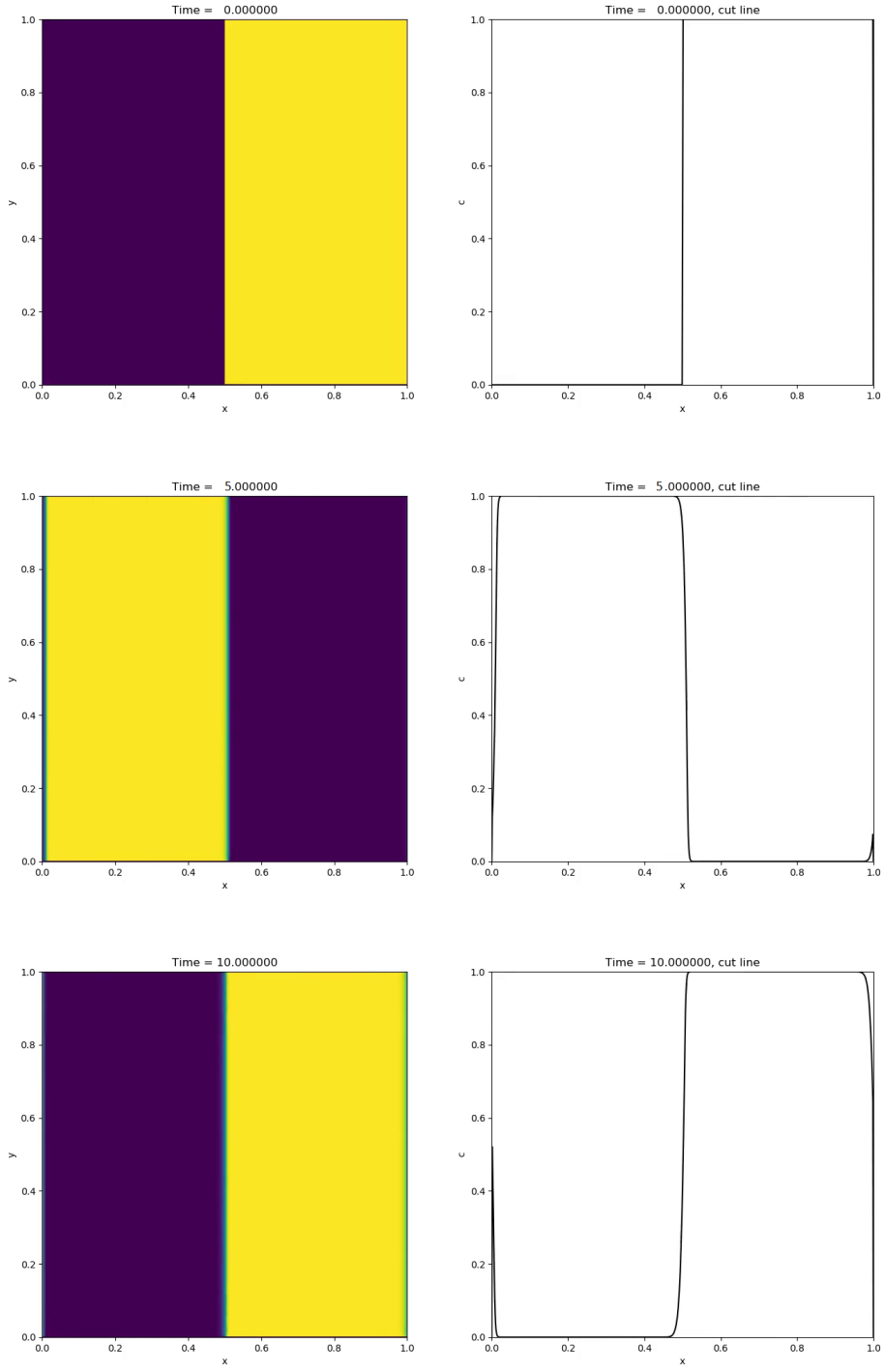

Figure 2.7: Solution: convection containing two discontinuities at $t = 0, 5, 10$ with horizontal velocity of 0.1. The left half of the graph is a surface plot of the solution, and the right half is the solution on a cut line $y = 0$. The solver was able to accurately retain the shock after one cycle of convection without introducing too much numerical dissipation. A van Albada 1 limiter was used on a 800×800 perturbed mesh.

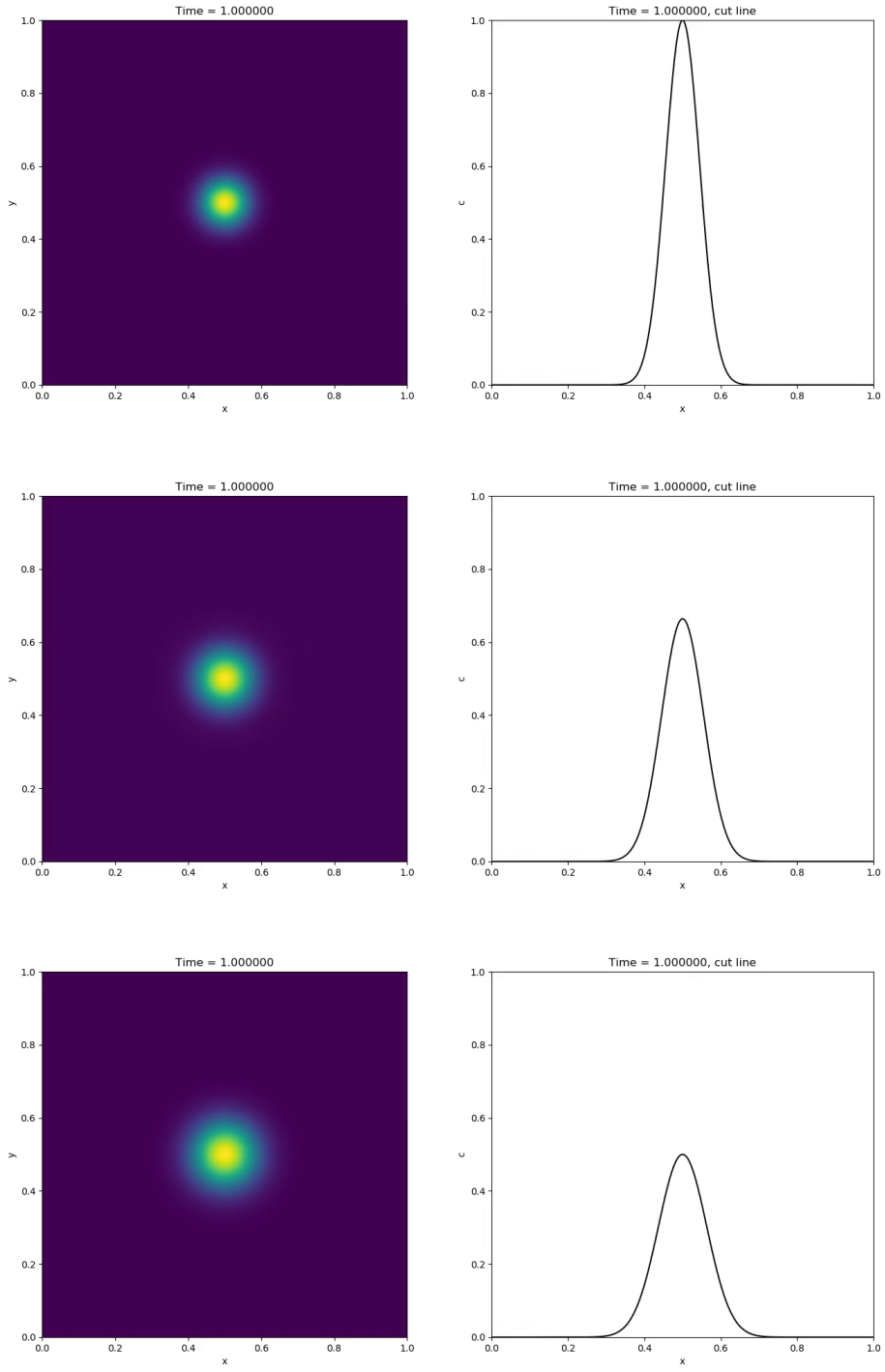

Figure 2.8: Solution: pure diffusion of a Gaussian wave $c(t=0) = e^{-\frac{(x-0.5)^2+(y-0.5)^2}{0.004}}$ at $t = 0, 0.5, 1$ with $D = 10^{-3}$. The left half of the graph is a surface plot of the solution, and the right half is the solution on a cut line $y = 0$. We can clearly see from the cut-line graph that the magnitude of the peak decreases with time due to diffusion. The mesh is a 800×800 perturbed mesh.

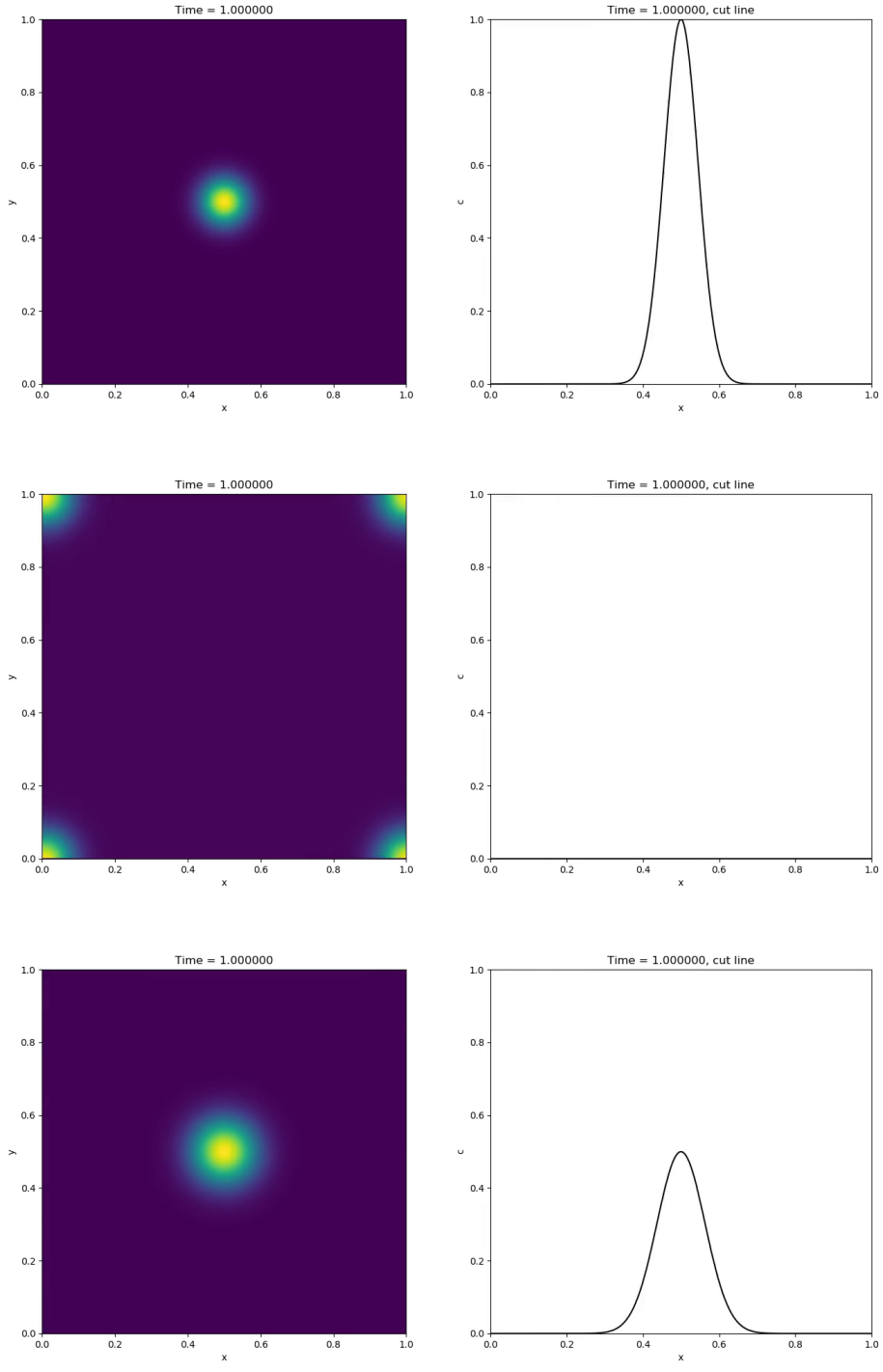

Figure 2.9: Solution: diffusion and convection of a Gaussian wave $c(t=0) = e^{-\frac{(x-0.5)^2+(y-0.5)^2}{0.004}}$ at $t = 0, 0.5, 1$ with $D = 10^{-3}$ and $v_x = v_y = 1.0$. The left half of the graph is a surface plot of the solution, and the right half is the solution on a cut line $y = 0$. The magnitude of the peak decreases and increases with respect to time due to the relative position of the peak and the location of the cut line. The final amplitude of the peak is lower than the initial condition due to diffusion The mesh is a 800×800 perturbed mesh and we used a van Albada 1 limiter.

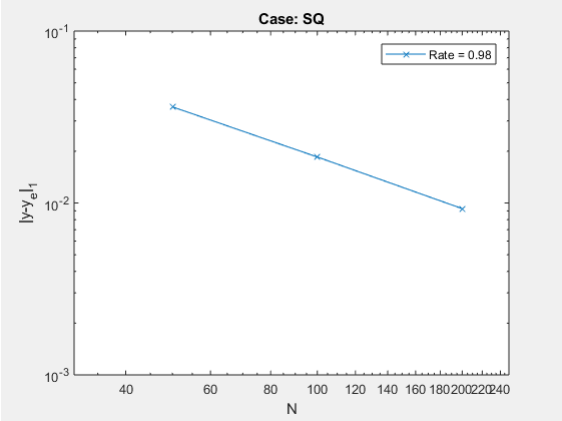

(a) Square convection, uniform mesh, 0.98

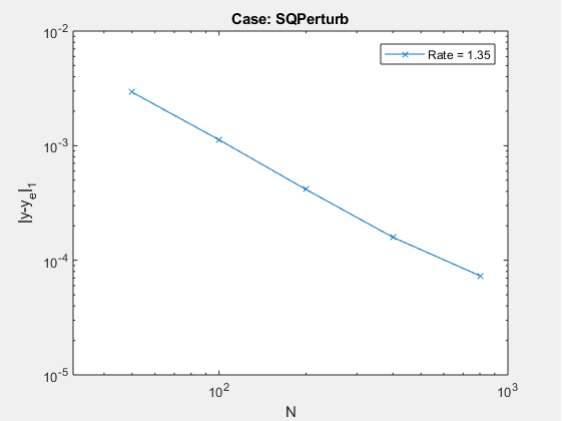

(b) Square convection, perturbed mesh, 1.35

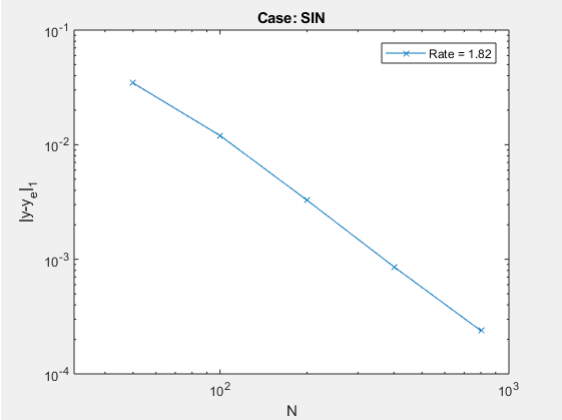

(c) Sine convection, uniform mesh, 1.82

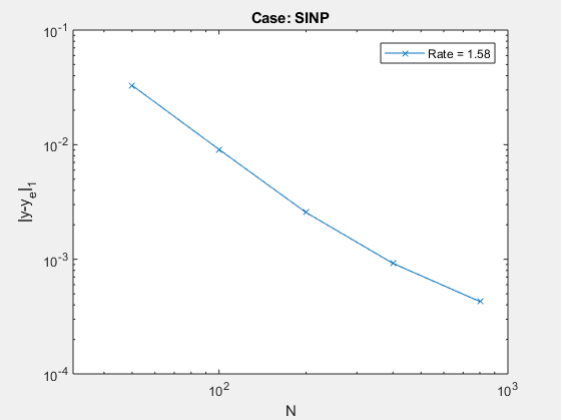

(d) Sine convection, perturbed mesh, 1.58

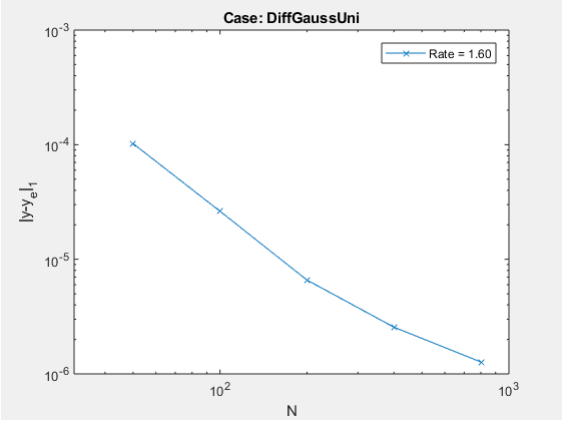

(e) Gaussian diffusion, uniform mesh, 1.60

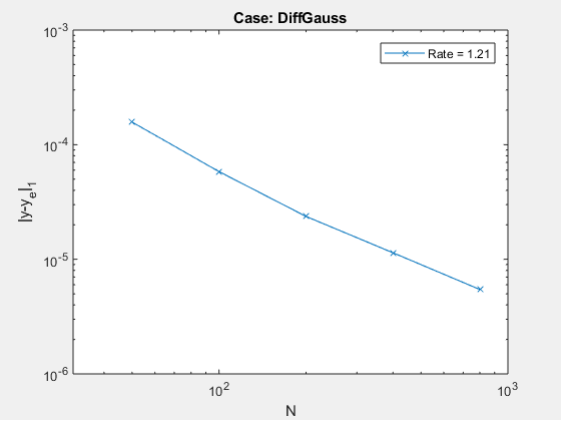

(f) Gaussian diffusion, perturbed mesh, 1.21

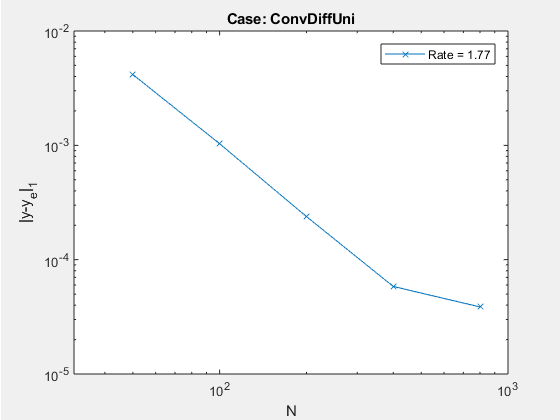

(g) Gaussian conv/diff, uniform mesh, 1.77

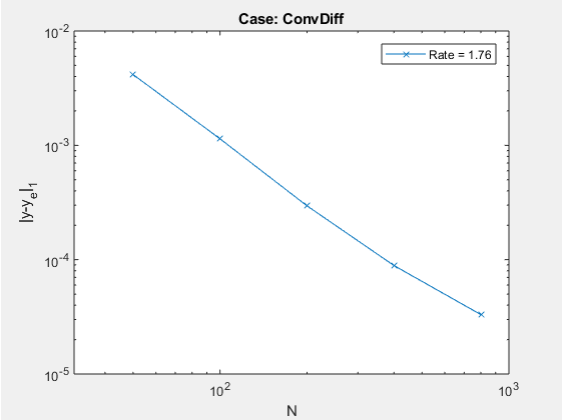

(h) Gaussian conv/diff, perturbed mesh, 1.76

Figure 2.10: Convergence rates for 8 model problems tested. Error measure is the 1-norm error. The cases in the left column (a, c, e, g) are studied using a uniform mesh. The cases in the right column (b, d, f, h) are studied with a perturbed mesh. The convergence rates are computed automatically with all points using a linear fit. Cases (a, b) are convection of a square wave. Cases (c, d) are convection of a sine wave. Cases (e, f) are diffusion of a Gaussian wave. Cases (g, h) are convection and diffusion of a Gaussian wave. These convergence rates generally show second-order convergence of our solver, except when a shock exists in the initial condition and final solution.

2.5 The 3D Stable Numerical Scheme

The 3D scheme is a further extension to the 2D scheme and allows us to solve simulation problems in real life. The method of finding gradients and diffusive fluxes are detailed below. The test problems for the 3D solver is more advanced than the 2D case and more closely resemble our use case.

2.5.1 Convective Flux

The gradients should be properly calculated and limited during calculation of the convective flux for stability of the solution. We further extended Huynh's formulation to 3D while using an alternative strategy of gradient limiting to enable the use of arbitrary gradient limiters. Our extension to K-T convective flux in hexahedral meshes is presented below.

We adopt a seven-element stencil, including the central element and the six neigh-

bor elements that share a face with the central element, to calculate the gradients in the central element. We divide the neighbor elements into three pairs: two elements in a pair share a face with the central element that is opposite to each other in the central element. The "left"/"right", "up"/"down", and "front"/"back" neighbors form the three pairs. We show one pair of the neighbor elements of the stencil in Figure 2.11.

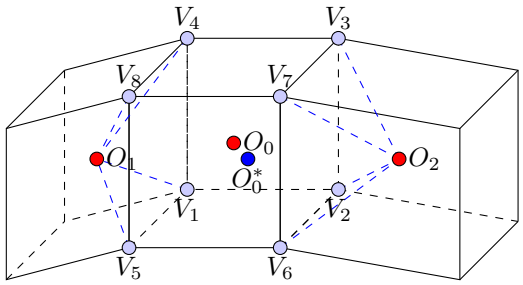

Figure 2.11: A central hexahedral element and a pair of neighbor elements in the seven-element stencil. A new 14-vertex, 24-faced element is formed by the cell centers of the six neighboring elements $O_{1...6}$ and eight vertices $V_{1...8}$ of the central element. The center of the original element is O_0 and the center of the new element is O_0^*. Only two neighboring elements shown to reduce cluttering.

For general meshes, the cell centers O_1, O_0, O_2 may not lie on the same straight line, creating difficulty in gradient limiting. Instead, we form new 24-faced elements from the seven-element stencil with 14 vertices, including six cell centers of the neighboring elements $O_{1...6}$ and eight vertices of the central element $V_{1...8}$. The new element consists of the central element and six pyramids formed by four vertices of the central element and the cell center of one neighboring element. An example of one such pyramid in Figure 2.11 is $O_1V_1V_4V_5V_8$. We denote the centroid of the 24-faced element as O_0^*. Similar 24-faced elements can be constructed for neighboring cells and the centroids are denoted as $O_{1...6}^*$. The cell value of the new element $c_{O_0^*}$ is found by a volume-weighed average, as shown in equation (2.14),

$$c_{O_0^*} = \frac{c_{O_0}V_{O_0} + \sum_{i=1}^{6} c_{O_i}V_{pyramid,i}}{V_{O_0} + \sum_{i=1}^{6} V_{pyramid,i}}, \tag{2.14}$$

where c_{O_i} is the cell value with cell center O_i, V_{O_0} is the cell volume of the central element, and $V_{pyramid,i}$ is the pyramid containing vertex O_i. The linear reconstruction $c(\vec{x})$ within the new cell can be written as follows in equation (2.15).

$$c(\vec{x}) = c_{O_0^*} + \nabla c \cdot (\vec{x} - \vec{x}_{O_0^*}). \tag{2.15}$$

To calculate the gradients ∇c, we first approximate the gradients with respect to the six neighbor elements using the new cell values. The direction is approximated using $\overrightarrow{O_0^* O_i}$, shown in equation (2.16).

$$\nabla c_{j,k} = (c_{O_0^*} - c_{O_{2j+k}^*}) \frac{\overrightarrow{O_0^* O_{2j+k}}}{|\overrightarrow{O_0^* O_{2j+k}}|}, \quad j = 0, 1, 2, \quad k = 0, 1. \tag{2.16}$$

Each of the three pairs of neighbors contribute one component to the gradient ∇c_j. We apply gradient limiting to each pair of the gradients with a suitable limiter function $g(r)$, as shown in equation (2.17). The following formulation assumes $c_{j,1}$ is calculated with the downstream neighbor element (such as, when flow is to the right in Figure 2.11).

$$r_j = \frac{\nabla c_{j,0}}{\nabla c_{j,1}}. \quad \nabla c_j = g(r_j) \nabla c_{j,1} \vec{n}_j, \quad j = 0, 1, 2. \tag{2.17}$$

The gradients are then transformed to Cartesian coordinates using the Jacobian matrix $\boldsymbol{J}$ obtained from the unit normal vectors $\vec{n}_j$, which is $\overrightarrow{O_0^* O_{2j+1}} / |\overrightarrow{O_0^* O_{2j+1}}|$. The transformation is shown in equation (2.18).

$$\boldsymbol{J} = \begin{bmatrix} \vec{n}_{0,x} & \vec{n}_{1,x} & \vec{n}_{2,x} \\ \vec{n}_{0,y} & \vec{n}_{1,y} & \vec{n}_{2,y} \\ \vec{n}_{0,z} & \vec{n}_{1,z} & \vec{n}_{2,z} \end{bmatrix}; \quad \begin{bmatrix} \nabla_{c,x} \\ \nabla_{c,y} \\ \nabla_{c,z} \end{bmatrix} = \boldsymbol{J} \begin{bmatrix} \nabla_{c,0} \\ \nabla_{c,1} \\ \nabla_{c,2} \end{bmatrix}. \tag{2.18}$$

We now use the semi-discrete K-T formulation [12] of the convective flux f using the gradients calculated from the previous steps, shown in equation (2.19). The edge

states c_+ and c_- are calculated at the same face center from the upstream and the downstream element using equation (2.15).

$$a = \vec{n} \cdot \boldsymbol{v}; \quad f = \frac{a}{2}(c_- + c_+) - \frac{|a|}{2}(c_+ - c_-). \tag{2.19}$$

Our extension reduces to the direction-splitting extension proposed in the original K-T method [12] in Cartesian grids when using a minmod limiter. The TVD property is guaranteed for this extension on Cartesian grids using any TVD limiter.

2.5.2 Diffusive Flux

We applied the Multi-Point Flux Approximation (MPFA) L-method in 3D [23] for diffusion. The MPFA L-method does not require the mesh to be $\boldsymbol{K}$-orthogonal and solves the diffusion fluxes accurately on general hexahedral meshes. We will only briefly explain the 3D MPFA L-method in this section.

Similar to the 2D case, each face now is divided into four quarter faces and each quarter face has four potential stencil configurations, which are shown in Figure 2.12.

The center element in the centered schemes is labeled as element 1 and the other elements labeled as element 2, 3, 4. In the non-centered scheme, elements 1, 2 border two other elements; element 1 shares a face with element 3; element 2 shares a face with element 4. We have the following notations:

- x_i, $i = 1 \ldots 4$: cell center of element i.
- $\bar{x}_1$: face center of shared face between elements 1 and 2.
- $\bar{x}_2$: face center of shared face between elements 1 and 3.
- $\bar{x}_3$: face center of shared face between elements 1 and 4 (centered) or 2 and 4 (non-centered).
- $\bar{x}_4$: edge center of shared edge between elements 1, 2, and 3.

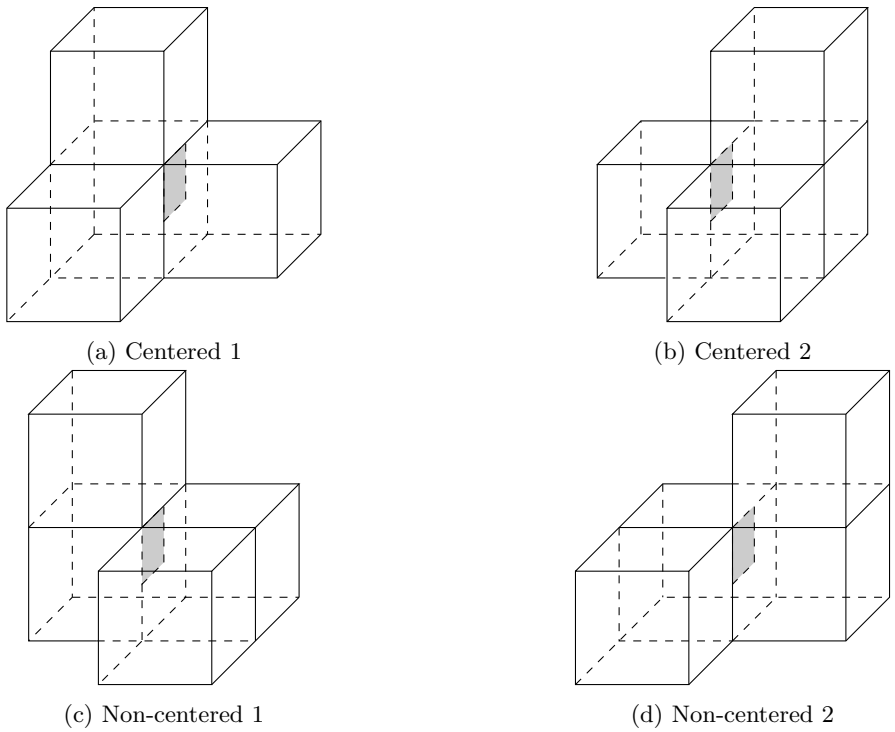

(a) Centered 1 (b) Centered 2

(c) Non-centered 1 (d) Non-centered 2

Figure 2.12: Four possible stencils for the MPFA L-Scheme: (a),(b) centered stencils and (c),(d) non-centered stencils. The shaded area is the quarter face that the flux is going to be computed for.

- $\bar{x}_5$: edge center of shared edge between elements 1, 2, and 4.
- $\bar{x}_6$: edge center of shared edge between elements 1, 3, and 4 (centered). For non-centered schemes, $\bar{x}_6$ is split into $\bar{x}_6$ and $\bar{x}_7$ on the edges that completes the quarter faces in the stencil, with $\bar{x}_6$ on the side of elements 1 and 3, and $\bar{x}_7$ on the side of elements 2 and 4.
- $\vec{n}_i$, $i = 1 \dots 3$ are the outward-pointing normal vectors of the quarter faces, with magnitude equal to the area of the quarter face.

The structure for getting the fluxes is similar to the 2D formulation, with the transmissibility matrix $\boldsymbol{T}$ formed by four sub-matrices:

$$\boldsymbol{T}\boldsymbol{u} = \boldsymbol{f}; \quad \boldsymbol{T} = \boldsymbol{C}\boldsymbol{A}^{-1}\boldsymbol{B} + \boldsymbol{D}. \tag{2.20}$$

We give one sample expression of the matrices $\boldsymbol{A}$, $\boldsymbol{B}$, $\boldsymbol{C}$, and $\boldsymbol{D}$, for a centered

stencil and a non-centered stencil. For a centered stencil,

(2.21)

$$\boldsymbol{A} = \begin{bmatrix} \omega_{111} - \omega_{121}r_{111} - \omega_{122} - \omega_{123}r_{112} & \omega_{112} - \omega_{121}r_{121} - \omega_{123}r_{122} & \omega_{113} - \omega_{121}r_{131} - \omega_{123}r_{132} \\ \omega_{211} - \omega_{231}r_{113} - \omega_{233}r_{111} & \omega_{212} - \omega_{231}r_{123} - \omega_{232} - \omega_{233}r_{121} & \omega_{213} - \omega_{231}r_{133} - \omega_{233}r_{131} \\ \omega_{311} - \omega_{341}r_{112} - \omega_{343}r_{113} & \omega_{312} - \omega_{341}r_{122} - \omega_{343}r_{123} & \omega_{313} - \omega_{341}r_{132} - \omega_{342} - \omega_{343}r_{133} \end{bmatrix}$$

$$\boldsymbol{B} = \begin{bmatrix} \sum_{k=1}^{3}\omega_{11k} + \omega_{121} + \omega_{123} - \sum_{j=1}^{3}(\omega_{121}r_{1j1} + \omega_{123}r_{1j2}) & -\sum_{k=1}^{3}\omega_{12k} & 0 & 0 \\ \sum_{k=1}^{3}\omega_{21k} + \omega_{231} + \omega_{233} - \sum_{j=1}^{3}(\omega_{231}r_{1j3} + \omega_{233}r_{1j1}) & 0 & -\sum_{k=1}^{3}\omega_{23k} & 0 \\ \sum_{k=1}^{3}\omega_{31k} + \omega_{341} + \omega_{343} - \sum_{j=1}^{3}(\omega_{341}r_{1j2} + \omega_{343}r_{1j3}) & 0 & 0 & -\sum_{k=1}^{3}\omega_{34k} \end{bmatrix}$$

$$\boldsymbol{C} = -\begin{bmatrix} \omega_{111} & \omega_{112} & \omega_{113} \\ \omega_{211} & \omega_{212} & \omega_{213} \\ \omega_{311} & \omega_{312} & \omega_{313} \end{bmatrix}$$

$$\boldsymbol{D} = \begin{bmatrix} \omega_{111} + \omega_{112} + \omega_{113} & 0 & 0 & 0 \\ \omega_{211} + \omega_{212} + \omega_{213} & 0 & 0 & 0 \\ \omega_{311} + \omega_{312} + \omega_{313} & 0 & 0 & 0 \end{bmatrix}.$$

For a non-centered stencil, we have

(2.22)

$$\boldsymbol{A} = \begin{bmatrix} \omega_{111} - \omega_{121} + c\omega_{113}(r_{231}r_{112} + r_{211}) \\ \quad -c\omega_{123}(r_{112} + r_{132}r_{211}) & c\omega_{113}r_{221} - \omega_{122} \\ & \quad -c\omega_{123}r_{211}r_{132} & \omega_{112} + c\omega_{113}r_{231}r_{122} \\ & & \quad -c\omega_{123}r_{122} \\ \omega_{221} - \omega_{233}r_{214} & & \\ c(\omega_{223} - \omega_{233}r_{234})(r_{112} + r_{132}r_{211}) & \omega_{222} - \omega_{233}r_{224} - \omega_{231} & \\ \quad -c\omega_{232}(r_{211} + r_{231}r_{112}) & \quad +c(\omega_{223} - \omega_{233}r_{234})r_{132}r_{221} & cr_{122}(\omega_{223} - \omega_{232}r_{231} - \omega_{233}r_{234}) \\ & \quad -c\omega_{232}r_{221} & \\ \omega_{311} - \omega_{343}r_{113} & & \\ c(\omega_{313} - \omega_{343}r_{133})(r_{211} + r_{231}r_{112}) & cr_{221}(\omega_{313} - \omega_{342}r_{132} - \omega_{343}r_{133}) & \omega_{312} - \omega_{341} - \omega_{343}r_{123} \\ \quad -cw_{342}(r_{112} + r_{132}r_{211}) & & \quad +c(\omega_{313} - \omega_{343}r_{133})r_{231}r_{122} \\ & & \quad -cw_{342}r_{122} \end{bmatrix}$$

$$\boldsymbol{B} = \begin{bmatrix} c(\omega_{123} - \omega_{113}r_{231})(1 - \sum_{j=1}^{3}r_{1j2}) & c(\omega_{123}r_{132} - w_{113})(1 - \sum_{j=1}^{3}r_{2j1}) & 0 & 0 \\ \quad + \sum_{k=1}^{3}\omega_{11k} & \quad - \sum_{k=1}^{3}\omega_{12k} & & \\ c(\omega_{233}r_{234} + \omega_{232}r_{231} - \omega_{223}) & \sum_{k=1}^{3}\omega_{22k} + \omega_{233}(1 - \sum_{j=1}^{3}r_{2j4}) & & \\ \quad \times(1 - \sum_{j=1}^{3}r_{1j2}) & \quad +c(-\omega_{223}r_{132} + \omega_{223}r_{234}r_{132} + \omega_{232}) & -\sum_{k=1}^{3}\omega_{23k} & 0 \\ & \quad \times(1 - \sum_{j=1}^{3}r_{2j1}) & & \\ c(\omega_{343}r_{133}r_{231} + \omega_{342} - \omega_{313}r_{231}) & c(-\omega_{313} + \omega_{343}r_{133} + \omega_{342}r_{132}) & & \\ \quad \times(1 - \sum_{j=1}^{3}r_{1j2}) + \sum_{k=1}^{3}\omega_{31k} & \quad \times(1 - \sum_{j=1}^{3}r_{2j1}) & 0 & -\sum_{k=1}\omega_{34k} \\ \quad +\omega_{343}(1 - \sum_{j=1}^{3}r_{11k}) & & & \end{bmatrix}$$

$$\boldsymbol{C} = -\begin{bmatrix} \omega_{111} + c\omega_{113}(r_{211} + r_{231}r_{112}) & c\omega_{113}r_{221} & \omega_{112} + c\omega_{113}r_{231}r_{122} \\ \omega_{221} + c\omega_{223}(r_{112} + r_{132}r_{211}) & \omega_{222} + c\omega_{223}r_{221}r_{132} & c\omega_{223}r_{122} \\ \omega_{311} + c\omega_{313}(r_{211} + r_{231}r_{112}) & c\omega_{313}r_{221} & \omega_{312} + c\omega_{313}r_{231}r_{122} \end{bmatrix}$$

$$\boldsymbol{D} = \begin{bmatrix} \sum_{k=1}^{3}\omega_{11k} - c\omega_{113}r_{231}(1 - \sum_{j=1}^{3}r_{1j2}) & -c\omega_{113}(1 - \sum_{j=1}^{3}r_{2j1}) & 0 & 0 \\ -c\omega_{223}(1 - \sum_{j=1}^{3}r_{1j2}) & \sum_{k=1}^{3}\omega_{22k} - c\omega_{223}r_{132}(1 - \sum_{j=1}^{3}r_{2j1}) & 0 & 0 \\ \sum_{k=1}^{3}\omega_{31k} - c\omega_{313}r_{231}(1 - \sum_{j=1}^{3}r_{1j2}) & -c\omega_{313}(1 - \sum_{j=1}^{3}r_{2j1}) & 0 & 0 \end{bmatrix}$$

$$c = \frac{1}{1 - r_{132}r_{231}}.$$

The definition of ω and r can be found in [23] or [24]. We applied Wolff et al.'s selection criteria [24] for selecting the proper stencil by selecting the maximum absolute sum of transmissibilities across the quarter interface.

2.5.3 Boundary Conditions

The boundary condition is handled as follows. For Dirichlet boundary conditions, a ghost cell is padded to the outside of the boundary element by reflecting the center of the boundary element with respect to the boundary face. For calculating the convective fluxes, we set one of the boundary states to be the boundary condition for calculating the flux in (2.19) while the diffusion flux uses a simple two-point flux approximation as in Wolff et al. [24]:

$$f = -\frac{D|\vec{n}|}{|x_f - x_c|}(c_f - c_c)|A|, \tag{2.23}$$

where the subscript f denotes face center and c denotes the cell center. The c_f is set to the boundary condition. A is the area of the boundary face.

Neumann boundaries are excluded from flux calculations and are added directly to the flux tally. Outflow boundary conditions are handled by setting the boundary value to the same as the boundary element and forcing zero diffusion flux. Inflow boundary condition is handled as a Dirichlet boundary condition.

2.5.4 Simulation and Verification

We chose an adaptive Dormand-Prince method for time marching [22]. We applied our solver to a convection-only and a diffusion-only model problem to verify that our solver is second-order accurate. These model problems are chosen because the capabilities of the solver are sufficiently evaluated and the analytical or very fine mesh solutions of these problems can be obtained. The convection problem is a diagonal transport of a gated Gaussian wave on a $1.0 \times 1.0 \times 1.0$ cubic domain, as shown in Figure 2.13a. The initial condition is a gated Gaussian wave centered at $(0.3, 0.65, 0.4)$ with the expression below in equation (2.24). $H(x)$ is the Heaviside step function. The convection velocity is $\boldsymbol{v} = [0.5, -0.375, 0.25]^T$ so that after $t = 0.4$

the gated wave is centered at $(0.5, 0.5, 0.5)$.

$$
\begin{aligned}
c(0) =& 10e^{-200((x-0.3)^2+(y-0.65)^2+(z-0.4)^2)} \cdot [H(x-0.2) - H(x-0.4)] \\
& \cdot [H(y-0.55) - H(y-0.75)] \cdot [H(z-0.3) - H(z-0.5)]
\end{aligned} \tag{2.24}
$$

The diffusion problem is set up in a concentric cylinder with inner diameter 0.5, outer diameter 1.0, and length 1.0, as shown in Figure 2.13b. The initial condition is a high-concentration band at $1/3 < r < 0.4$. The diffusion coefficient is $D = 0.01$ over the whole domain. All boundaries are zero-flux Neumann boundaries. The simulation stops at $t = 0.5$.

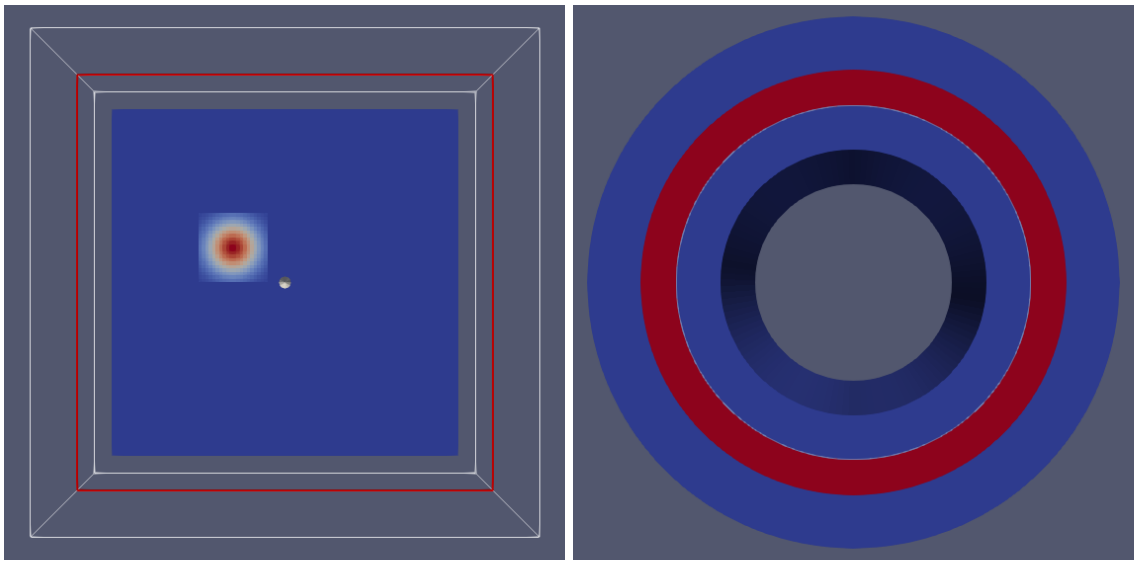

(a) Initial conditions of the convection problem. (b) Initial conditions of the diffusion problem.

Figure 2.13: Initial conditions of the 3D convection-only and diffusion-only problems, cut at the $z = 0.4$ plane. The convection problem is transport of a gated Gaussian wave with velocity components in all three directions, and the diffusion problem is diffusion of a high-concentration band in a cylindrical domain.

We performed convergence studies on the model problems shown above in Figure 2.13. We chose the l_2 difference between the exact solution and the obtained solution, integrated through the whole domain, as our error measure. The expression of the error measure e is shown in equation (2.25).

$$
e = \iiint_V ||c_{exact} - c_{sol}||_2 dV. \tag{2.25}
$$

The convergence graphs are shown in Figure 2.14. We find 2.7th order of convergence in convection and second order of convergence in diffusion. The extra order of convergence may have come from an L2-projection of the initial conditions during the initialization step. We integrated the initial condition using high-order accurate Gaussian quadrature over each element to obtain the initial values of the element. Similar treatments in Discontinuous Galerkin methods using linear basis functions have reported higher than 2.5th order convergence on 2-norms [25]. The exact reasons for superconvergence are subject to further investigation. We also calculated the order of convergence using the 1-norm as stated in (2.13), and the order of convergence is 1.35 for convection problem and 1.99 for diffusion. The superconvergence disappears when using the 1-norm.

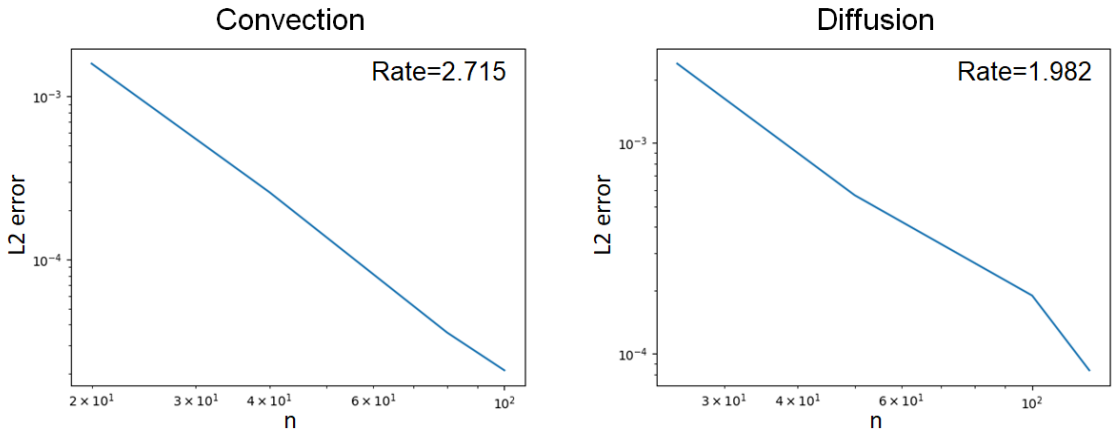

Figure 2.14: Convergence rates for the model problems for l_2 error norm. The convergence rate is 2.715 for convection and 1.982 for diffusion.

We then applied the solver towards a test case that contains convection and diffusion inside a domain separated by boundary of flow. The simulation domain is the same concentric cylinder as in Figure 2.13b. The initial condition is a high concentration band at $0.3 < r < 0.4$ and $0.1 < z < 0.2$. A Dirichlet inflow condition of $c = 0$ is set to the near end of the domain at $z = 0$ and an outflow boundary

condition is set to the boundary at $z = 1$. All other boundary conditions are no flux Neumann boundaries. The flow is present at $r > 0.4$ only with a velocity of 1.0 in the $+z$ direction. The diffusion coefficient is $D = 10^{-4}$. The simulation stops at $t = 0.6$. Using the definition of the characteristic length as the ratio of the volume and the surface of the domain, we find the Péclet number Pe to be 4.67×10^3 where flow is present, as shown in equation (2.26).

$$Pe = \frac{Lu}{D} = \frac{\frac{4}{3}\pi(0.5^3 - 0.25^3) \times 1.0}{\pi(0.5^2 + 0.25^2) \times 10^{-4}} = 4.67 \times 10^3. \tag{2.26}$$

Slices cut at $x = 0$, or equivalently, $\theta = 0$, at $t = 0$ and $t = 0.6$ can be seen in Figure 2.15 on a $125 \times 125 \times 125$ mesh with a van Leer limiter. The r-position of the trail where flow is present increases with increased z, indicating contributions from both convection and diffusion in the transport process. When flow is not present, the transport process is purely diffusion.

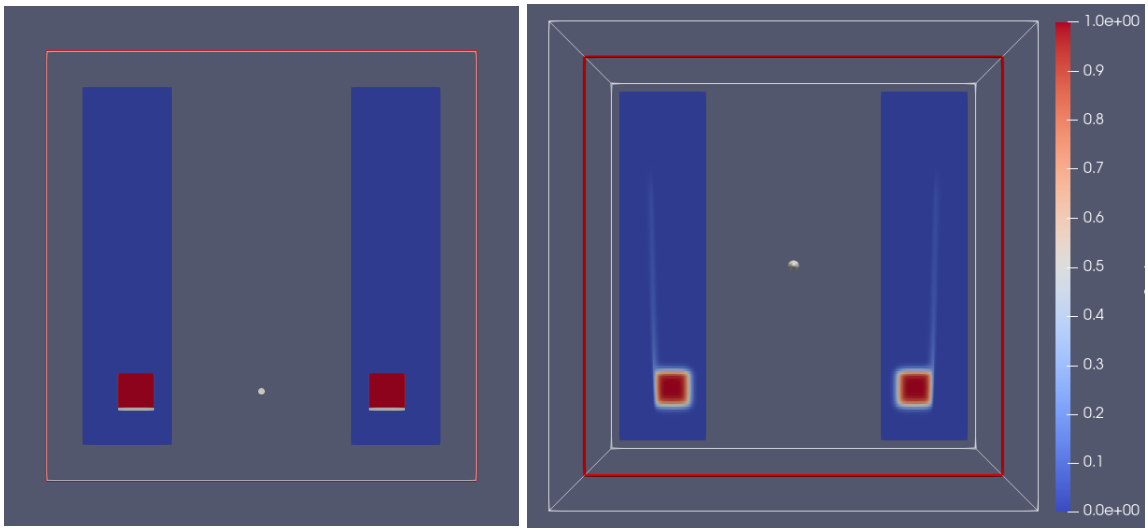

(a) $t = 0$ (b) $t = 0.6$

Figure 2.15: $t = 0$ and $t = 0.6$ solutions of the test convection-diffusion problem in domain separated by boundaries of flow, cut at the $x = 0$ plane.

The shock happens at the interface when convection is suddenly added to the transport process, in other words, at $r = 0.4$. Figure 2.16 shows a c vs. r plot on

a cut line through $\theta = 0$ and $z = 0.15$. We can see that even though the solution dropped many orders of magnitude, the solution is stable and no negative values are found along the cut line.

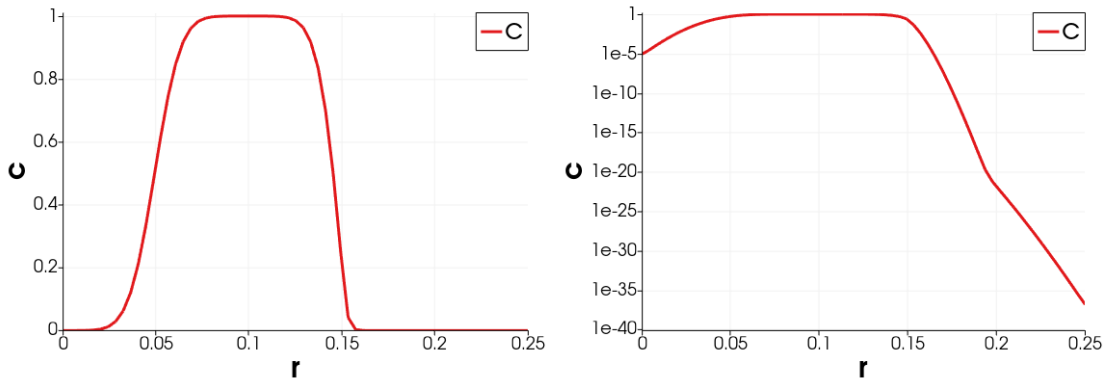

(a) Linear scale

(b) Log scale

Figure 2.16: Cut line of at $\theta = 0$ and $z = 0.15$ for solution of the test convection-diffusion problem in domain separated by boundary of flow at $t = 0.6$.

2.6 Implementation Details

This section covers the implementation details that were not discussed in the main numerical methods.

2.6.1 Flux Limiters

We adopted the following TVD and symmetric ($g(r) = g(1/r)$) flux limiters for both the 2D and 3D solver.

- minmod [26]:

$$g(r) = \max(0, \min(1, r)) \tag{2.27}$$

- superbee [26]:

$$g(r) = \max(0, \min(2r, 1), \min(r, 2)) \tag{2.28}$$

- van Leer [27]:

$$g(r) = \frac{r + |r|}{1 + |r|} \tag{2.29}$$

- van Albada 1 [28]:

$$g(r) = \frac{r^2 + r}{r^2 + 1} \tag{2.30}$$

- Sweby [29]:

$$g(\beta, r) = \max(0, \min(\beta r, 1), \min(r, \beta)). \tag{2.31}$$

2.6.2 Computing Environment

The main solver is programmed using C++ and compiled with the Intel C++ compiler 19.1 (Intel, Santa Clara, CA) with C++ 17 and OpenMP support. Visualization is done by pure Python for the 2D solver, but the 3D solver uses an open source visualization package vtk and visualization software Paraview (Kitware, Clifton Park, NY). Data serialization for mesh elements used the language-neutral protocol buffer developed by Google (Mountain View, CA).

All the test problems are run on an Intel i7-8700 processor with /O2 and optimization flags for the Coffee Lake structures turned on. The runtime for 2D sample problems on 800×800 meshes is about 25 minutes. The runtime 3D sample problems on $100 \times 100 \times 100$ meshes is about 40 minutes.

The codes for both the 2D and 3D solvers, with some sample results, are hosted on private GitHub and GitLab repositories. If access is granted, the codes can be obtained from:

- 2D solver: `https://github.com/micw523/FVQuadSolver`;

  `https://gitlab.com/bioxusn/FVQuadSolver`.

- 3D solver: `https://github.com/micw523/HexMeshFV`;

  `https://gitlab.com/bioxusn/HexMeshFV`.

Bibliography

[1] E. J. Brisbois, R. P. Davis, A. M. Jones, T. C. Major, R. H. Bartlett, M. E. Meyerhoff, and H. Handa, "Reduction in thrombosis and bacterial adhesion with 7 day implantation of s-nitroso-n-acetylpenicillamine (snap)-doped elast-eon e2as catheters in sheep," *Journal of Materials Chemistry B*, vol. 3, no. 8, pp. 1639–1645, 2015.

[2] Y. Wo, E. J. Brisbois, J. Wu, Z. Li, T. C. Major, A. Mohammed, X. Wang, A. Colletta, J. L. Bull, A. J. Matzger, *et al.*, "Reduction of thrombosis and bacterial infection via controlled nitric oxide (no) release from s-nitroso-n-acetylpenicillamine (snap) impregnated carbosil intravascular catheters," *ACS biomaterials science & engineering*, vol. 3, no. 3, pp. 349–359, 2017.

[3] H. Ren, A. Colletta, D. Koley, J. Wu, C. Xi, T. C. Major, R. H. Bartlett, and M. E. Meyerhoff, "Thromboresistant/anti-biofilm catheters via electrochemically modulated nitric oxide release," *Bioelectrochemistry*, vol. 104, pp. 10–16, 2015.

[4] R. S. Falk, "Analysis of finite element methods for linear hyperbolic problems," in *Discontinuous Galerkin Methods*, pp. 103–112, Springer, 2000.

[5] F. Bassi and S. Rebay, "A high-order accurate discontinuous finite element method for the numerical solution of the compressible navier–stokes equations," *Journal of computational physics*, vol. 131, no. 2, pp. 267–279, 1997.

[6] F. Bassi and S. Rebay, "Gmres discontinuous galerkin solution of the compressible navier-stokes equations," in *Discontinuous Galerkin Methods*, pp. 197–208, Springer, 2000.

[7] K. Shahbazi, "An explicit expression for the penalty parameter of the interior penalty method," *Journal of Computational Physics*, vol. 205, no. 2, pp. 401–407, 2005.

[8] P. B. Bochev, M. D. Gunzburger, and J. N. Shadid, "Stability of the supg finite element method for transient advection–diffusion problems," *Computer methods in applied mechanics and engineering*, vol. 193, no. 23-26, pp. 2301–2323, 2004.

[9] S. R. Lynch, N. Nama, J. Zu, C. J. Arthurs, O. Sahni, and C. A. Figueroa, "Numerical considerations for advection-diffusion problems in cardiovascular hemodynamics," *arXiv preprint arXiv:1910.08165*, 2019.

[10] P. L. Roe, "Approximate riemann solvers, parameter vectors, and difference schemes," *Journal of computational physics*, vol. 43, no. 2, pp. 357–372, 1981.

[11] H. Nessyahu and E. Tadmor, "Non-oscillatory central differencing for hyperbolic conservation laws," 1988.

[12] A. Kurganov and E. Tadmor, "New high-resolution central schemes for nonlinear conservation laws and convection–diffusion equations," *Journal of Computational Physics*, vol. 160, no. 1, pp. 241–282, 2000.

[13] P. Arminjon and A. St-Cyr, "Nessyahu–tadmor-type central finite volume methods without predictor for 3d cartesian and unstructured tetrahedral grids," *Applied Numerical Mathematics*, vol. 46, no. 2, pp. 135–155, 2003.

[14] J. H. Seo and R. Mittal, "A sharp-interface immersed boundary method with improved mass conservation and reduced spurious pressure oscillations," *Journal of computational physics*, vol. 230, no. 19, pp. 7347–7363, 2011.

[15] B. B. Jørgensen and N. P. Revsbech, "Diffusive boundary layers and the oxygen uptake of sediments and detritus 1," *Limnology and oceanography*, vol. 30, no. 1, pp. 111–122, 1985.

[16] J. P. Steinbrenner, "Construction of prism and hex layers from anisotropic tetrahedra," in *22nd AIAA Computational Fluid Dynamics Conference*, p. 2296, 2015.

[17] I. Aavatsmark, "An introduction to multipoint flux approximations for quadrilateral grids," *Computational Geosciences*, vol. 6, no. 3-4, pp. 405–432, 2002.

[18] Z.-C. Zhang, S. J. Yu, and S.-C. Chang, "A space-time conservation element and solution element method for solving the two-and three-dimensional unsteady euler equations using quadrilateral and hexahedral meshes," *Journal of Computational Physics*, vol. 175, no. 1, pp. 168–199, 2002.

[19] H. Huynh, "Analysis and improvement of upwind and centered schemes on quadrilateral and triangular meshes," in *16th AIAA Computational Fluid Dynamics Conference*, p. 3541, 2003.

[20] J. Droniou, "Finite volume schemes for diffusion equations: introduction to and review of modern methods," *Mathematical Models and Methods in Applied Sciences*, vol. 24, no. 08, pp. 1575–1619, 2014.

[21] I. Aavatsmark, G. Eigestad, B. Mallison, and J. Nordbotten, "A compact multipoint flux approximation method with improved robustness," *Numerical Methods for Partial Differential Equations: An International Journal*, vol. 24, no. 5, pp. 1329–1360, 2008.

[22] J. R. Dormand and P. J. Prince, "A family of embedded runge-kutta formulae," *Journal of computational and applied mathematics*, vol. 6, no. 1, pp. 19–26, 1980.

[23] I. Aavatsmark, G. T. Eigestad, B.-o. Heimsund, B. Mallison, J. M. Nordbotten, E. Øian, *et al.*, "A new finite-volume approach to efficient discretization on challenging grids," *SPE Journal*, vol. 15, no. 03, pp. 658–669, 2010.

[24] M. Wolff, Y. Cao, B. Flemisch, R. Helmig, and B. Wohlmuth, "Multi-point flux approximation l-method in 3d: numerical convergence and application to two-phase flow through porous media," *Radon Ser. Comput. Appl. Math., De Gruyter*, vol. 12, pp. 39–80, 2013.

[25] Y. Cheng and C.-W. Shu, "Superconvergence and time evolution of discontinuous galerkin finite element solutions," *Journal of Computational Physics*, vol. 227, no. 22, pp. 9612–9627, 2008.

[26] P. L. Roe, "Characteristic-based schemes for the euler equations," *Annual review of fluid mechanics*, vol. 18, no. 1, pp. 337–365, 1986.

[27] B. Van Leer, "Towards the ultimate conservative difference scheme. ii. monotonicity and conservation combined in a second-order scheme," *Journal of computational physics*, vol. 14, no. 4, pp. 361–370, 1974.

[28] G. D. Van Albada, B. Van Leer, and W. W. Roberts, "A comparative study of computational methods in cosmic gas dynamics," in *Upwind and high-resolution schemes*, pp. 95–103, Springer, 1997.

[29] P. K. Sweby, "High resolution schemes using flux limiters for hyperbolic conservation laws," *SIAM journal on numerical analysis*, vol. 21, no. 5, pp. 995–1011, 1984.

Chapter III

Simulation Results of a Nitric Oxide-Releasing Catheter

With a solver capable of resolving sharp concentration gradients caused by a separation of flow, we are ready to tackle simulation problems inspired by real life. This chapter covers detailed methods and results of simulations involving NO-releasing catheters.

3.1 Introduction

Intravascular catheters are essential for long-term vascular access in both diagnosis and treatment. However, these catheters can trigger the thrombotic pathway since the blood recognizes them as foreign surface. Bacteria can also adhere to the surface of these catheters and form biofilms. [1] Malfunctioning catheters due to clotting and infections will have to be replaced. In particular, malfunctioning catheters interrupts the life sustaining clearance dialysis offers, diminishes the quality of life for end stage renal disease patients is burdensome for both patients and caregivers. Catheter replacement are burdensome for both patients and physicians and are occasionally associated with additional complications [2]. Even though the recommended guidelines are followed, catheter-related infections can still occur and claim lives.

Nitric oxide (NO) is a potent antimicrobial and antithrombotic agent. Although healthy vascular endothelial cells release NO into the bloodstream, the effective con-

centration of NO may be too low to exhibit physiological effects around the surface of intravascular catheters. [3] Higher local concentration is needed to activate the desired physiological properties of NO to be used in catheters, requiring the catheter to provide a source of NO.

Recent approaches to provide a source of NO in the catheters include electrochemical reactions [4] or impregnation of the catheter with a NO-releasing compound [5]. Evidence can be seen through bench and animal models associated with these approaches. However, the release profile of NO in animals is largely inaccessible in situ and the measurements are mostly performed post-experiment, showing a significant different result compared to lab bench models largely due to convection by blood flow. Even if a *in vivo* NO sensor is developed, the sensor may still disrupt the flow field and obtain different results compared to real-life situations.

Catheters are typically thin tubes made of biocompatible materials. The sizes of commercial catheters are typically presented in the French scale [6], with 1 French (Fr) corresponding to 0.33 mm in the outer diameter of the catheter. Depending on the clinical need, the diameter of the catheters can range from 3 Fr [7] to 30 Fr [8]. The axial cavities of the catheters are called lumens and are used for vascular access. More than one lumen may be present for multiple needs during clinical intervention. For example, in dual-lumen catheters, the two lumens can be used to draw and return blood during dialysis sessions [9]. Infection rates may vary between different number of lumens present in a catheter [10]. Attempts to validate NO release for all configurations of catheters will require a very large of animals and would be unfeasible.

Computer simulation provides a cost-effective solution to estimate the release profile of NO inside the animal. The simulated results can also be used as a platform

to design optimal shapes of the catheter, placement of the NO source, and NO release profiles without dedicating excessive resources and efforts to performing animal experiments.

We will simulate two methods of NO release in this chapter: NO release from a SNAP-doped catheter in a single-lumen catheter and from a dual lumen catheter with a dedicated lumen for generating NO electrochemically.

3.2 Methods

The solver used in the simulation is discussed in Chapter II, specifically designed to capture the concentration drop across interfaces separated by boundaries of flow. [11] We will be using this solver to simulate two scenarios of NO release.

3.2.1 Doped Catheter in a Concentric Cylinder Domain

The first category is a SNAP-doped catheter. SNAP is synthesized from N-acetyl penicillamine, which is an FDA-approved drug for heavy metal poisoning. [1] SNAP has been successfully doped into CarboSil (silicone polycarbonate polyurethane) [12, 13], Elast-eon (silicone polyurethane) [5, 14], and silicone catheters [15, 16]. SNAP is typically doped at a 1 to 15 weight % during fabrication of the catheters by soaking the catheter in the polymer solution containing SNAP in regular intervals, and a new layer of SNAP-doped polymer is applied to the catheter after evaporating the solvent [12]. The doping process is repeated until the catheter reaches the desired diameter. The SNAP-doped active layers are often covered by non-doped polymers to avoid spikes in NO release. Recently, dedicated lumens of SNAP-containing material have been used as another design choice [17].

SNAP is a very good candidate for NO release because of its stability under heat, humidity, and ethylene oxide sterilization [12]. It only releases NO when both

humidity and temperature are elevated [12]. SNAP also exists as solid crystals in the catheters [12] and the reaction kinetics of SNAP releasing NO is not clear. To avoid this problem, we will attempt using the weight % of SNAP as the initial NO concentration in the doped region and characterize the results.

We will simulate an Elast-eon doped single-lumen catheter in this chapter with configurations in Brisbois et al. [5]. The catheter consists of three layers: an active layer doped with SNAP sandwiched by two inactive layers. The relative width of these layers is 1 (inactive): 5 (active): 1 (inactive), as shown in Figure 3.1.

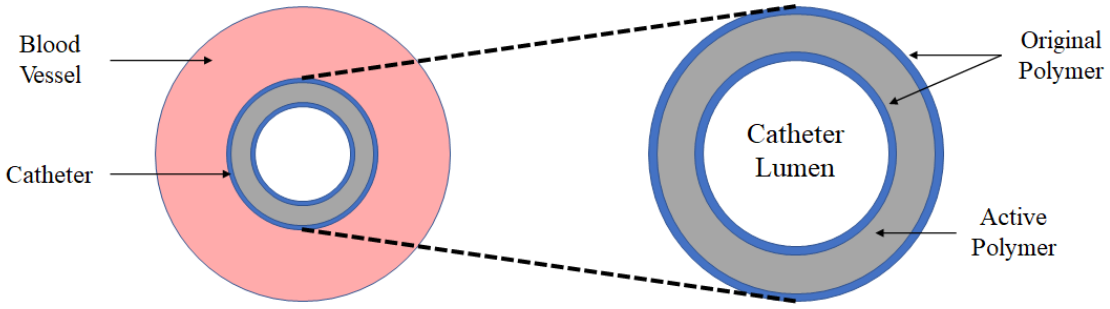

Figure 3.1: A cross-section diagram of the simulation domain. The catheter is placed at the center of a blood vessel as shown on the left side. The composition of the simulated catheter, zoomed in, is shown on the right. The catheter has a 1 (active): 5 (active): 1 (inactive) configuration. The 1:5:1 ratio is reflected in the width of the layers.

We placed this catheter inside a jugular vein. We assume the flow inside a jugular vein is Newtonian and non-oscillatory. We also assume that the catheter is placed at the center of the vein, so that the equation for the Poiseuille flow inside a concentric cylinder can be imposed. Available clinical data measurements are average flow rates and the geometries of the vein. We can use equation (3.1) to derive for the flow field inside the domain. Convection only exists between the catheter and the vessel wall, and inside the catheter only diffusion is present.

$$
\begin{aligned}
p_x &= -\frac{8\mu Q}{\pi}\left(r_2^4 - r_1^4 - \frac{(r_2^2 - r_1^2)^2}{\ln(r2/r1)}\right)^{-1} \\
u(r) &= -\frac{p_x}{4\mu}(r_1^2 - r^2) - \frac{p_x}{4\mu}(r_2^2 - r_1^2)\frac{\ln(r/r_1)}{\ln(r_2/r_1)}.
\end{aligned} \tag{3.1}
$$

Indeed, the situation above is a simplified model of a catheter placed inside a jugular vein of length 30 cm. The real situation is likely that the catheter is in a winding pattern and bounces off the vessel walls. However, we would like to call into attention that, if the catheter is placed closer to the vessel wall, NO concentration would increase due to the vessel wall endothelial cells being a source of NO [18] with comparable NO generation rates with respect to NO-releasing catheters [5].

Relevant parameters related to the simulation is presented in Table 3.1. For initial conditions, we set the NO concentration in the active layer to be $3.0 \times 10^{-5}\text{mol/cm}^3$, which is approximately the solid concentration of the NO releasing compound in the catheter [5]. We simulated the problem for up to 720 seconds on a $55 \times 55 \times 55$ domain. Meshing of this domain is straightforward, with nodes evenly distributed on the r, θ, and z axes.

Table 3.1: Symbols, physical meanings, and values used in the simulation of the SNAP-doped single-lumen catheters

Symbol	Physical Meaning	Value	Source
Q	Flow rate (jugular vein)	$18.168\text{cm}^3/\text{s}$	[19]
μ	Blood viscosity	3.8 cP	[20]
r_2	Radius (jugular vein)	0.324 cm	[19]
r_1	Radius (catheter, outer)	0.165 cm	[5]
r_{in}	Radius (catheter, inner)	0.104 cm	[5]
D_w	Diffusion coefficient, NO in water	2.21×10^{-5} cm^2/s	[21]
D_p	Diffusion coefficient, NO in catheter polymer	8.5×10^{-6} cm^2/s	[21]

No NO is assumed to be present in the vein at $t = 0$. The r-boundaries, including the outer surface of the vein and the inner surface of the catheter, are set to Neumann boundary conditions with no flux. The z-boundaries are set to inflow and outflow boundary conditions. The concentration of the inflow is set to 0. No reaction is considered in this simulation. The initial state of the problem is shown in Figure 3.2.

The Péclet number, characterizing the relative strength of convective to diffusive transport in this case is shown in equation (3.2). We estimate the Péclet number

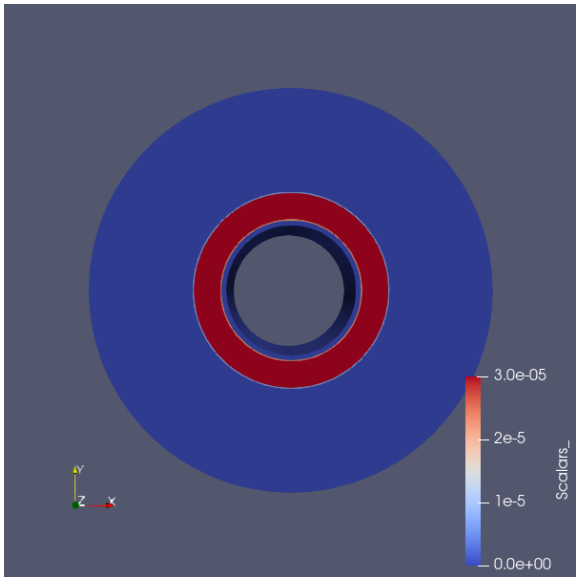

Figure 3.2: Initial condition of the SNAP-doped catheter. The active layer is shown in red has an initial concentration of $c(NO) = 3.0 \times 10^{-5}\text{mol/cm}^3$.

using the maximum velocity in the flow field:

$$Pe = \frac{Lu}{D} = \frac{\frac{4}{3}\pi(0.324^3 - 0.165^3) \times 111.8}{\pi(0.324^2 + 0.165^2) \times 2.21 \times 10^{-5}} = 1.506 \times 10^6. \tag{3.2}$$

3.2.2 Catheter with Continuous Electrochemical NO Source

Generating NO electrochemically is a relatively novel solution with one key advantage: the ability to modulate the NO release by controlling the current through the electrochemical source [22]. These catheters use copper electrodes coupled with nitrite solutions to generate nitric oxide and has shown to be able to continuously generate NO [4, 23]. We will simulate NO release in a 7-Fr dual-lumen catheter with flux values documented in Ren et al. [21]. A schematic for this catheter is shown in Figure 3.3.

Relevant parameters related to this simulation is included in Table 3.2. Similarly, we placed the catheter, length 30 cm, at the center of the jugular vein. We set the initial concentration of NO in blood to be 6pmol/L according to the estimation by Liu et al. [3]. The z-boundaries are set to inflow and outflow boundary conditions.

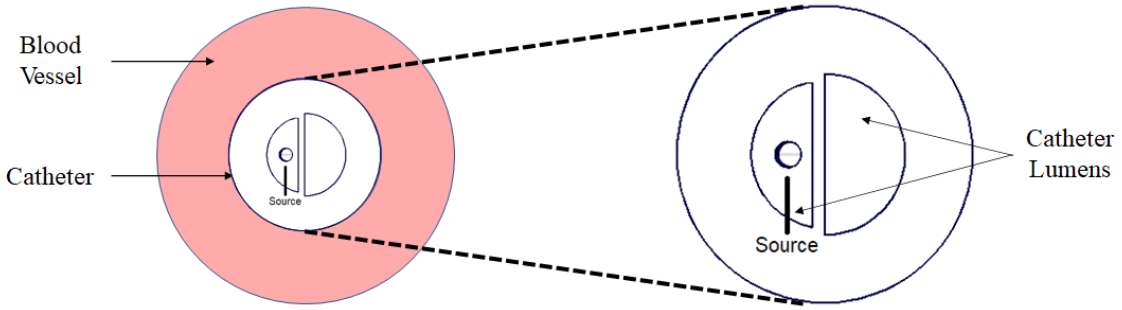

Figure 3.3: A dual-lumen catheter with an electrochemical NO source placed in one lumen. The dual-lumen catheter is placed at the center of a blood vessel.

The inflow boundary condition takes the same value as the initial condition. The vessel wall is assumed to be a no-flux boundary. Again, we did not consider reaction in this model.

Table 3.2: Symbols, physical meanings, and values used in the simulation of the electrochemical dual-lumen catheters

Symbol	Physical Meaning	Value	Source
Q	Flow rate (jugular vein)	$18.168\text{cm}^3/\text{s}$	[19]
μ	Blood viscosity	3.8 cP	[20]
r_2	Radius (jugular vein)	0.327 cm	[19]
r_1	Radius (catheter, outer)	0.117 cm	[21]
r_{in}	Radius (source, 0.03 cm off center)	0.006 cm	Estimate
f	Source NO flux	$1.067 \times 10^{-10}\text{mol/cm}^3$	[21]
D_w	Diffusion coefficient, NO in water	2.21×10^{-5} cm^2/s	[21]
D_p	Diffusion coefficient, NO in catheter polymer	8.5×10^{-6} cm^2/s	[21]

Meshing of this domain is challenging, since the NO source is 3 mm off center and we need to preserve the cylindrical boundary layer shapes at the surface of the catheter. The nodes on z direction are still placed in regular intervals, but the $r-\theta$ plane are meshed in three domains. We used a $64 \times 48 \times 48$ mesh for this problem, and the the r nodes are split into 28, 4, and 32 layers. Meshing of the first 28 layers involves placing nodes evenly on a circle with moving centers, until the center gets moved to the center of the outer domain (vein). The expression of the circle is:

$$(x + r_{in}\frac{i_r}{28})^2 + y^2 = (r_1 - r_{in}\frac{i_r}{28})^2, \tag{3.3}$$

where i_r is the index of layers in the r-direction. The second four layers place the

nodes evenly until reaching the surface of the catheter, and the rest of the layers evenly map out the domain where flow is present. The initial condition as well as an illustration of the mesh can be seen in Figure 3.4.

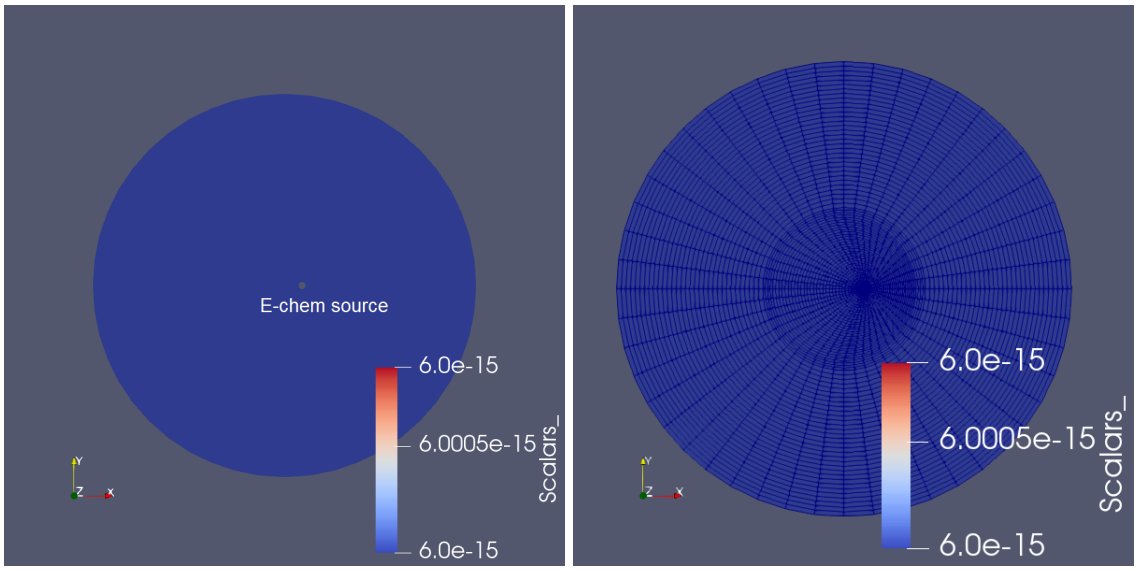

(a) Initial condition (b) Three-layered mesh

Figure 3.4: Initial condition and mesh illustration of a catheter with an electrochemical NO source

The Péclet number for this transport problem can be calculated similarly, using the maximum velocity as an estimate:

$$Pe = \frac{Lu}{D} = \frac{\frac{4}{3}\pi(0.327^3 - 0.117^3) \times 95.88}{\pi(0.327^2 + 0.117^2) \times 2.21 \times 10^{-5}} = 1.597 \times 10^6. \tag{3.4}$$

3.3 Results

3.3.1 Doped Catheter in a Concentric Cylinder Domain

As a side-to-side comparison, we present a model with no flow inside the domain, as well as our proposed model. The result at $t = 180$s is shown below to illustrate the effect of convection.

As shown in Figure 3.5, significant amount of NO is carried out of the domain by convection. To illustrate this behavior, we present a line cut at $z = 15$cm of the

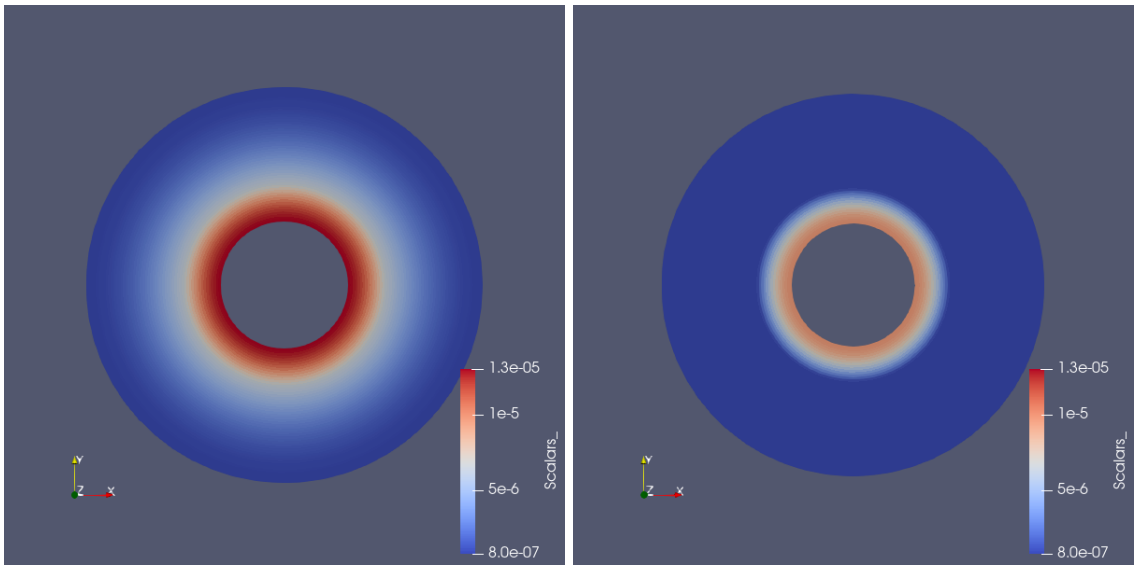

(a) Diffusion Only (b) Diffusion and Convection

Figure 3.5: (a) Diffusion only (b) diffusion and convection models for a catheter with a NO reservoir at $t = 180$s. The overall concentration of NO decreases in the model with convection, and the concentration drops quickly around where flow is present.

solution with respect to the radial distance r in both linear and log scales, as shown in Figure 3.6.

Next, we illustrate the effect of the z-location on the concentration of NO. Going further along the catheter, more NO is accumulated by convection from the earlier parts. We cut the solution at $r = 0.1651$cm, which is 10^{-4} cm from the surface of the catheter at $r = 0.165$cm. Figure 3.7 shows this behavior.

Lastly we present the time-dependent behavior by characterizing the amount of NO remaining in the catheter with respect to time. The result is shown in Figure 3.8. We can see that the amount of NO remaining decreases to below 10% after 360 seconds, and below 1% after 720 seconds.

3.3.2 Catheter with Continuous Electrochemical NO Source

We are mostly interested in two measures in this scenario: the time for NO release to reach steady-state, and the concentration of NO around the surface of the catheter

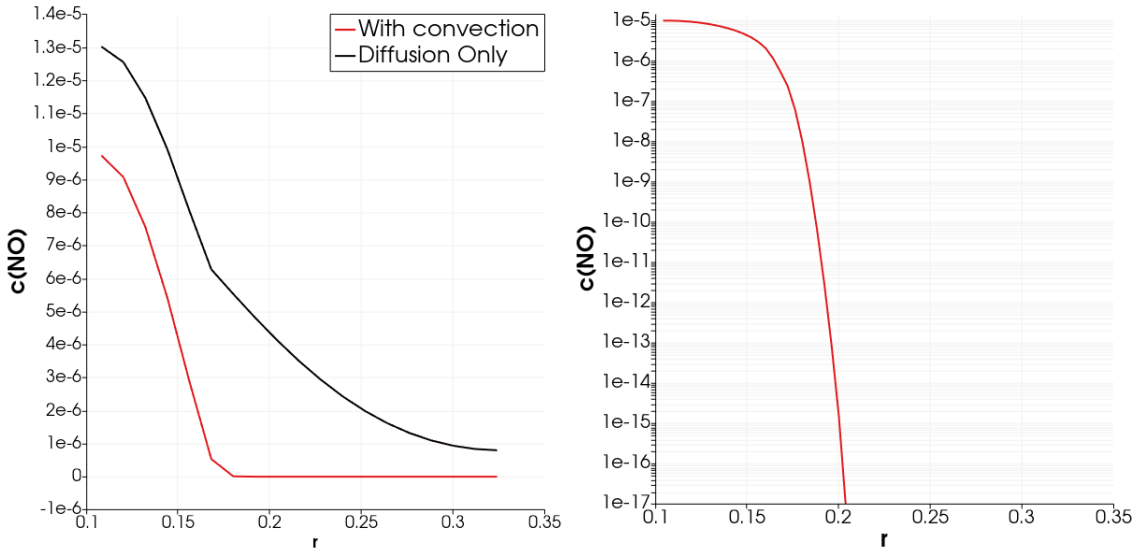

(a) Linear plot

(b) Log plot, convection only

Figure 3.6: Linear and log plots of the solution cut at $z = 15$cm with respect to the radial coordinate r. The linear plot shows both cases whether convection is present or not. The log plot only shows the case when convection is present. The concentration curve for the convection case is fully below the pure diffusion case. The kink in the solution curve is caused by a change in diffusion coefficient at the surface of the catheter.

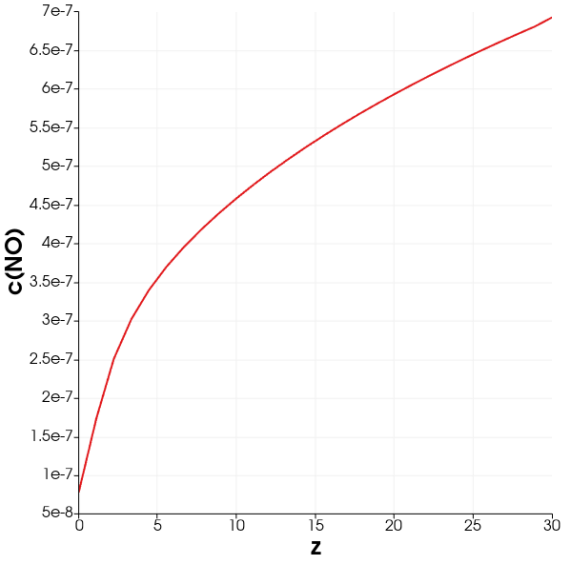

Figure 3.7: The concentration of NO versus z coordinates with a NO reservoir. Increased z coordinates receives NO from earlier regions by convection, thus increasing the concentration.

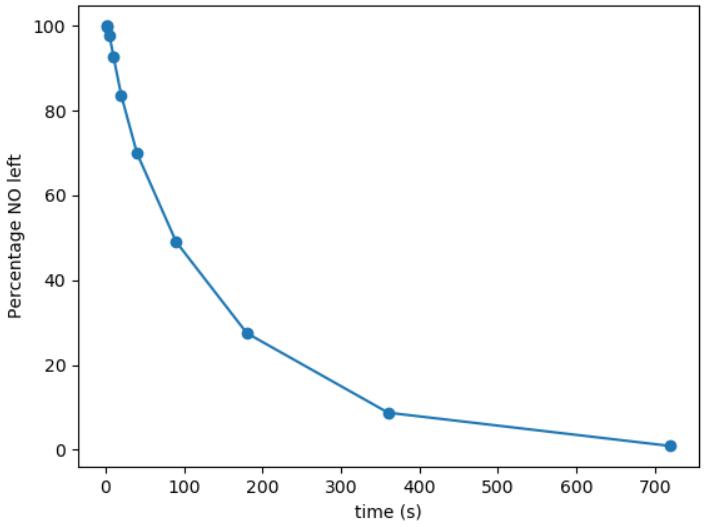

Figure 3.8: NO consumption in a catheter with a NO reservoir by convection. More than 99% of the NO initially present in the catheter is depleted after 720 seconds.

at the steady-state. First, we will present the time-dependent solution of the NO release, as shown in Figure 3.9. The solution shown contains a surface plot of the concentration at $z = 15$cm. It also includes a line cut on the x axis to show the concentration levels across the catheter. On the line cut we can easily notice that the solution on two sides of the catheter show different behaviors due to the off-center placement of the source, with the side closer to the source showing higher concentration levels.

To further illustrate the difference of the concentration behavior on both sides, a line-cut solution on Figure 3.10 shows the relationship between the concentration of NO with respect to z at 10^{-4} cm outside of the catheter. The concentration is above 10^{-11}mol/cm^3 or 10^{-8}mol/L for almost all z. The difference in the concentration is about 2.6 times, even though the catheter is only 0.03cm off center (about 25% of the catheter radius).

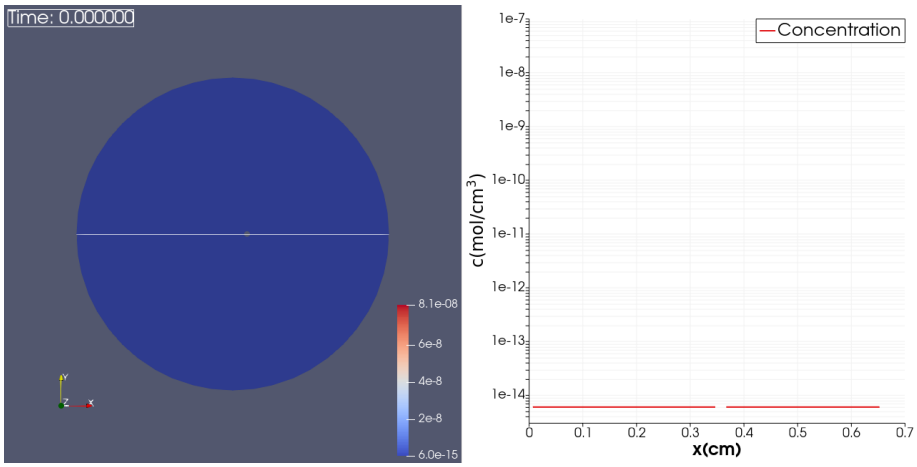

(a) $t = 0$s

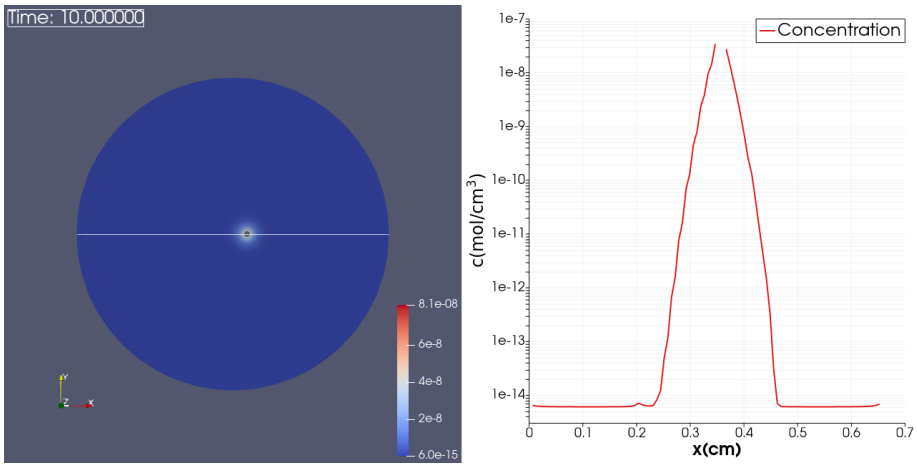

(b) $t = 10$s

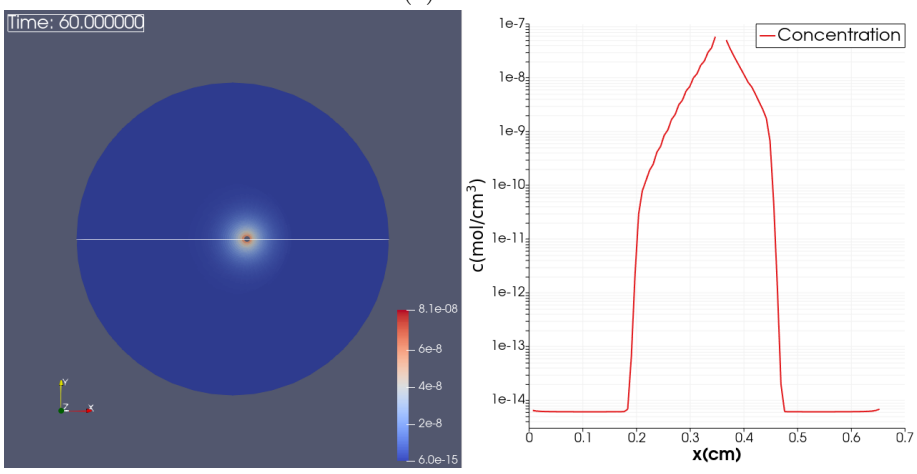

(c) $t = 60$s

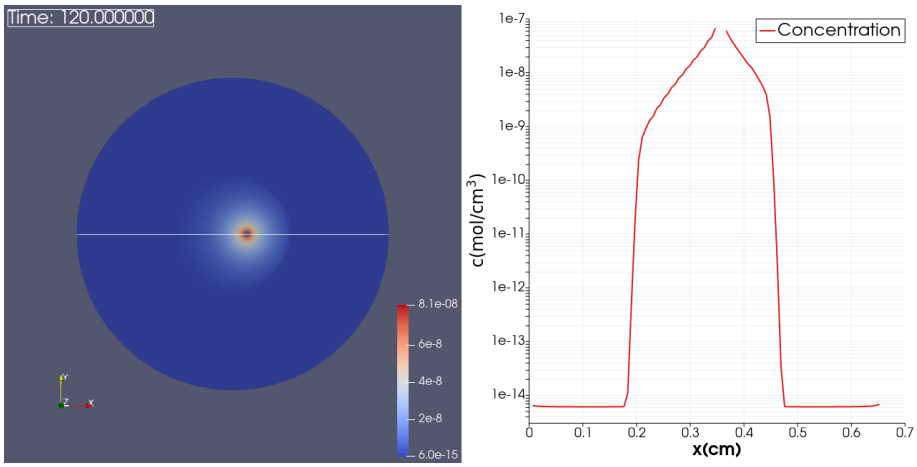

(d) $t = 120$s

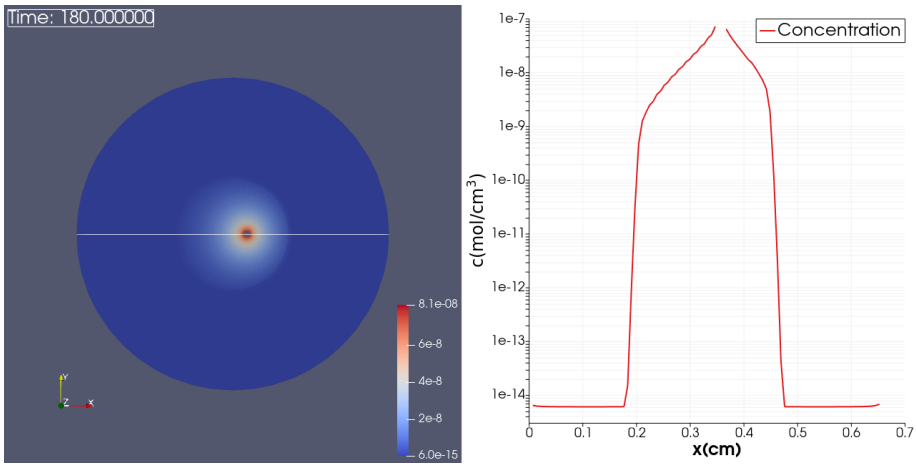

(e) $t = 180$s

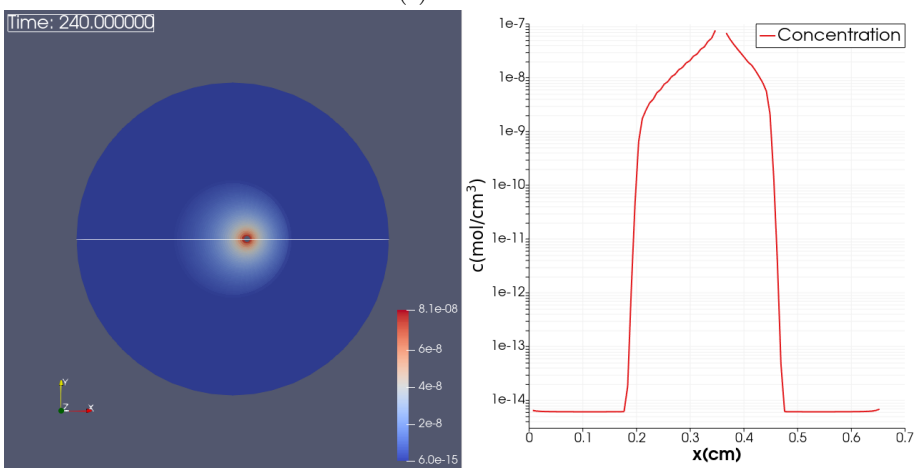

(f) $t = 240$s

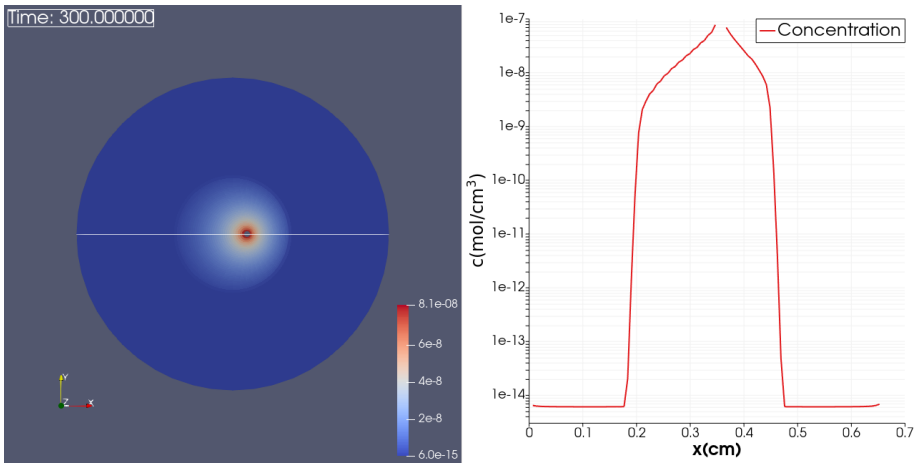

(g) $t = 300$s

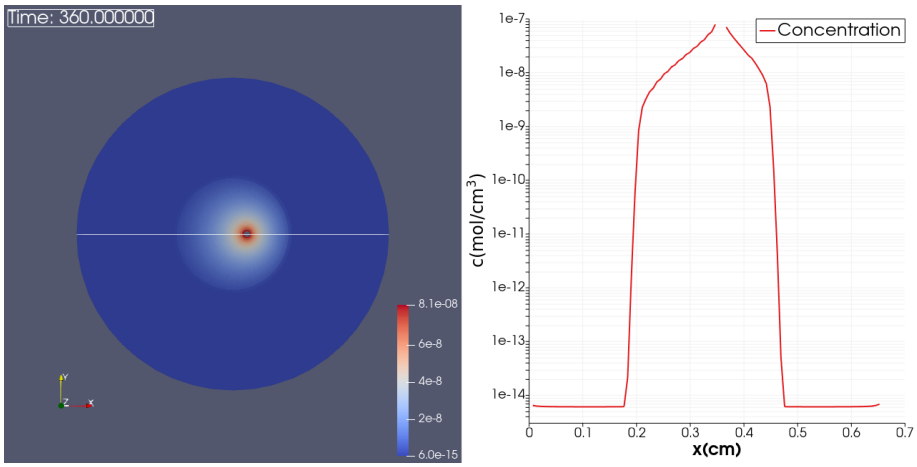

(h) $t = 360$s

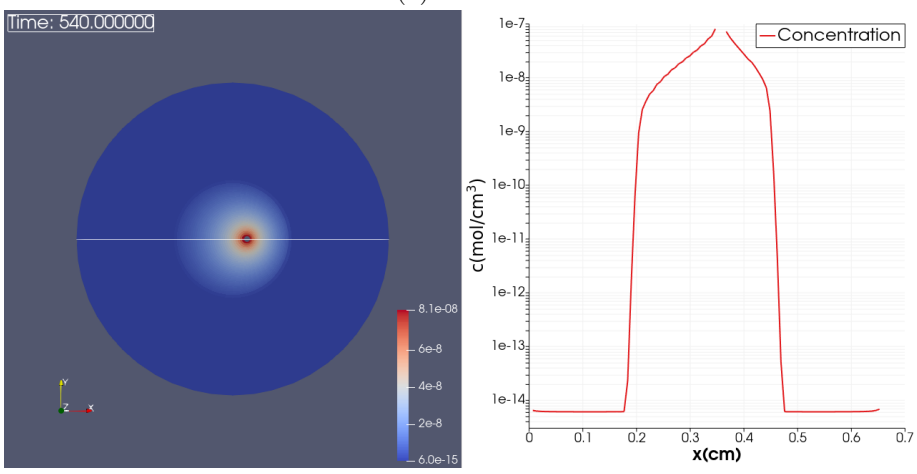

(i) $t = 540$s

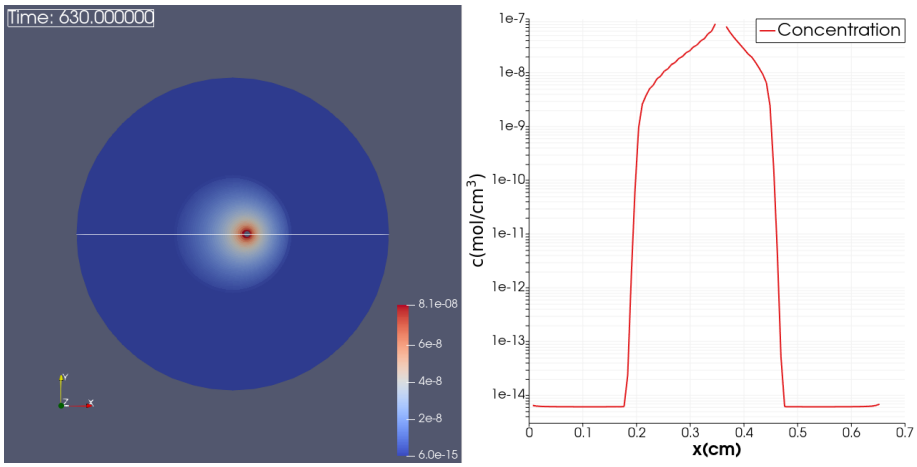

(j) $t = 630$s

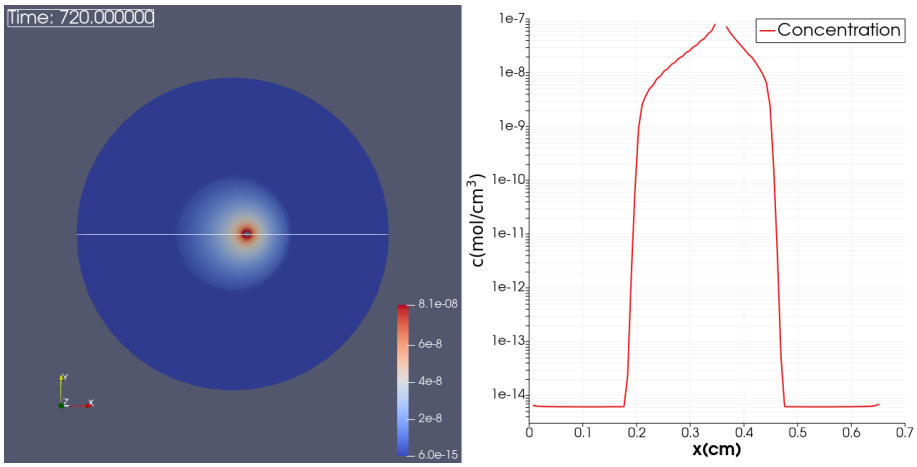

(k) $t = 720$s

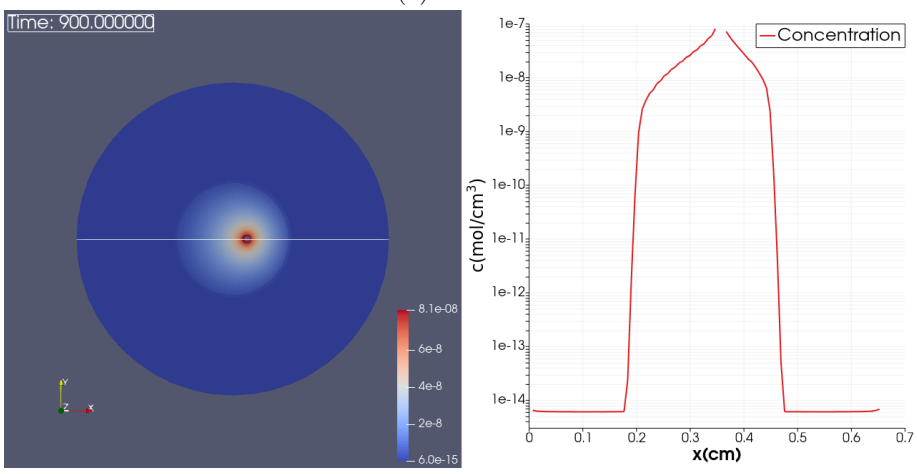

(l) $t = 900$s

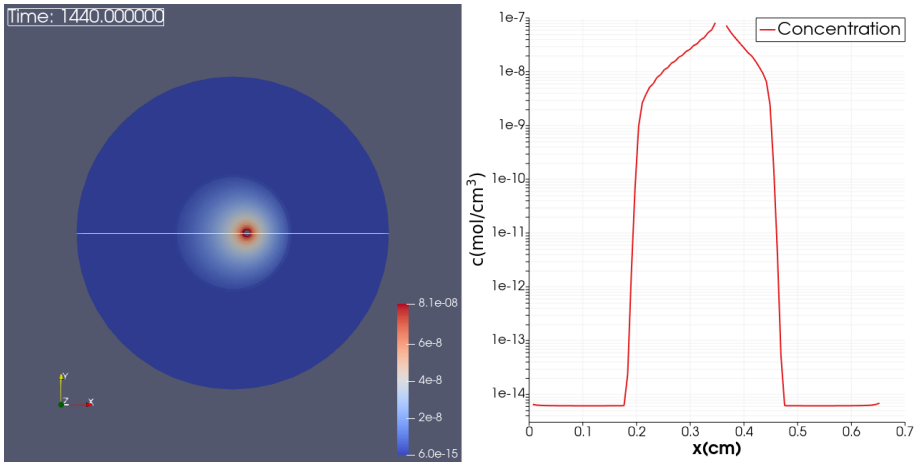

(m) $t = 1440$s

Figure 3.9: Time-dependent solutions of NO concentration for a NO-releasing catheter with an electrochemical NO source. For each time point, the figure on the left shows the surface concentration at $z = 15$cm. The figure on the right shows the concentration along a cut line on the x axis, shown as a white line on the left figure. The solution reaches steady state after around 630 seconds.

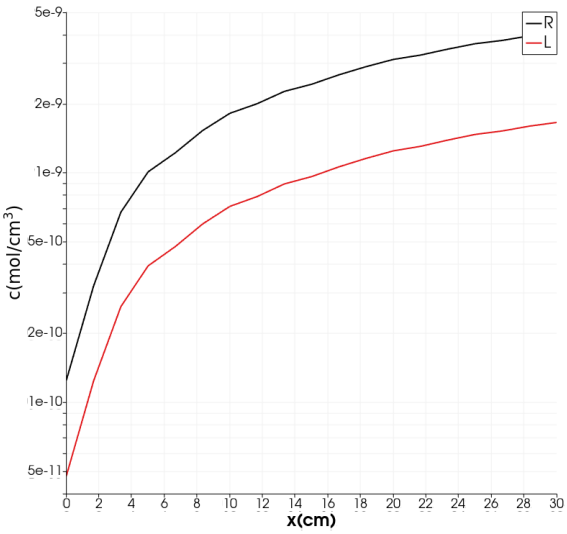

Figure 3.10: The concentration of NO versus z coordinates for the electrochemical catheter. Increased z coordinates receives NO from earlier regions by convection, thus increasing the concentration. Due to the off-center placement of the NO source, the plot "L" and "R" depicts the lowest and highest possible levels of NO on the $r = 0.1168$cm surface, which is 10^{-4} cm from the surface of the catheter.

3.4 Discussion

The treatment of SNAP-doped catheter as a NO reservoir is clearly incorrect, based on the fact that 99.9% of NO has leaked out after three minutes of simulation, which is clearly in contrast to experimental results that the catheter could work for more than 7 hours *in vivo* [12]. Therefore, we should avoid drawing excessive conclusions from the first model. We will need to have further understanding of NO-releasing kinetics of SNAP before making suggestions to designs. However, the model does illustrate the effect of convection to NO transport and suggests that NO is quickly cleared, in around 12 minutes, from the catheters when NO sources are depleted.

The situation with an electrochemical NO source provides us with more insight. The concentration of NO is likely above nM range, which should be sufficient in suppressing most biofilm formations [24, 25, 26]. The time to reach to the steady state concentration is about 10.5 minutes, which is reasonably quick.

Both situations demonstrated that the concentration of NO is the lowest near the insertion site. The catheter near the insertion site should be closely monitored to control infection.

One major issue with this simulation is that reaction is not considered. NO tends to be consumed relatively slowly when gas-phase oxygen is present, but quickly in whole blood. An estimate of the half-life of NO in whole blood is about 1.8 ms [27] and we can calculate the corresponding reaction rate constant k

$$k = \frac{\ln 2}{t_{1/2}} = 385 s^{-1}. \tag{3.5}$$

NO can be quickly consumed by reaction if convection is not present. We can calculate the relative strength of reaction with respect to diffusion using the second

Damköhler number in equation (3.6). In this discussion, we will analyze the case of a SNAP-doped catheter and use an estimate of the length to be the width of the inactive layers.

$$Da = \frac{kL}{D} = \frac{385 \times (0.165 - 0.104)/7}{8.5 \times 10^{-6}} = 3.94 \times 10^5. \tag{3.6}$$

The Damköhler estimate is slightly smaller then the Péclet number we calculated in (3.2), hinting the effect of the reactions might not be as significant. However, it is difficult to estimate the relative strength of the reactions with respect to convection, since calculation of the first Damköhler's number requires a control volume for a convective time scale. Locally NO is continuously generated along the surface of the catheter and such a control volume does not exist. As of now, we do not know if added reaction will affect the simulation outcome and will require further investigation.

The flow field was treated as a concentric cylinder Poiseuille flow. These two problems have very similar settings, with the second problem having a slightly higher Péclet number (or, a longer characteristic length). We estimate the maximum Reynolds number as:

$$Re = \frac{\rho u L}{\mu} = \frac{1.07 \cdot 95.88 \cdot 0.3688}{0.038} = 996. \tag{3.7}$$

Turbulence effects should be minimal at this level of Reynolds number [28] and our imposed flow field should be valid. Depending on the placement and location of the catheter, the flow field may vary and additional simulations may be required. In addition, when the catheter is used to draw or administer fluids, flow exists inside the catheter and NO will be consumed by convection by convection inside the catheter lumen.

Bibliography

[1] Y. Wo, E. J. Brisbois, R. H. Bartlett, and M. E. Meyerhoff, "Recent advances in thromboresistant and antimicrobial polymers for biomedical applications: just say yes to nitric oxide (no)," *Biomaterials science*, vol. 4, no. 8, pp. 1161–1183, 2016.

[2] N. P. O'grady, M. Alexander, L. A. Burns, E. P. Dellinger, J. Garland, S. O. Heard, P. A. Lipsett, H. Masur, L. A. Mermel, M. L. Pearson, *et al.*, "Guidelines for the prevention of intravascular catheter-related infections," *Clinical infectious diseases*, vol. 52, no. 9, pp. e162–e193, 2011.

[3] X. Liu, Q. Yan, K. L. Baskerville, and J. L. Zweier, "Estimation of nitric oxide concentration in blood for different rates of generation evidence that intravascular nitric oxide levels are too low to exert physiological effects," *Journal of Biological Chemistry*, vol. 282, no. 12, pp. 8831–8836, 2007.

[4] H. Ren, J. Wu, C. Xi, N. Lehnert, T. Major, R. H. Bartlett, and M. E. Meyerhoff, "Electrochemically modulated nitric oxide (no) releasing biomedical devices via copper (ii)-tri (2-pyridylmethyl) amine mediated reduction of nitrite," *ACS applied materials & interfaces*, vol. 6, no. 6, pp. 3779–3783, 2014.

[5] E. J. Brisbois, R. P. Davis, A. M. Jones, T. C. Major, R. H. Bartlett, M. E. Meyerhoff, and H. Handa, "Reduction in thrombosis and bacterial adhesion with 7 day implantation of s-nitroso-n-acetylpenicillamine (snap)-doped elast-eon e2as catheters in sheep," *Journal of Materials Chemistry B*, vol. 3, no. 8, pp. 1639–1645, 2015.

[6] K. V. Iserson, "J.-f.-b. charrière: the man behind the "french" gauge," *The Journal of emergency medicine*, vol. 5, no. 6, pp. 545–548, 1987.

[7] J. Theron, P. Courtheoux, F. Alachkar, G. Bouvard, and D. Maiza, "New triple coaxial catheter system for carotid angioplasty with cerebral protection.," *American journal of neuroradiology*, vol. 11, no. 5, pp. 869–874, 1990.

[8] G. Baudin, M. Chassang, E. Gelsi, S. Novellas, G. Bernardin, X. Hébuterne, and P. Chevallier, "Ct-guided percutaneous catheter drainage of acute infectious necrotizing pancreatitis: assessment of effectiveness and safety," *American Journal of Roentgenology*, vol. 199, no. 1, pp. 192–199, 2012.

[9] P. Blake, S. Huraib, G. Wu, and P. Uldall, "The use of dual lumen jugular venous catheters as definitive long term access for haemodialysis," *The International journal of artificial organs*, vol. 13, no. 1, pp. 26–31, 1990.

[10] C. Dezfulian, J. Lavelle, B. K. Nallamothu, S. R. Kaufman, and S. Saint, "Rates of infection for single-lumen versus multilumen central venous catheters: a meta-analysis," *Critical care medicine*, vol. 31, no. 9, pp. 2385–2390, 2003.

[11] X. Wang, M. Meyerhoff, and J. Bull, "A second-order method for convection-diffusion equation across interfaces separated by boundaries of flow," *Bulletin of the American Physical Society*, vol. 64, 2019.

[12] Y. Wo, Z. Li, E. J. Brisbois, A. Colletta, J. Wu, T. C. Major, C. Xi, R. H. Bartlett, A. J. Matzger, and M. E. Meyerhoff, "Origin of long-term storage stability and nitric oxide release behavior of carbosil polymer doped with s-nitroso-n-acetyl-d-penicillamine," *ACS applied materials & interfaces*, vol. 7, no. 40, pp. 22218–22227, 2015.

[13] Y. Wo, E. J. Brisbois, J. Wu, Z. Li, T. C. Major, A. Mohammed, X. Wang, A. Colletta, J. L. Bull, A. J. Matzger, *et al.*, "Reduction of thrombosis and bacterial infection via controlled

nitric oxide (no) release from s-nitroso-n-acetylpenicillamine (snap) impregnated carbosil intravascular catheters," *ACS biomaterials science & engineering*, vol. 3, no. 3, pp. 349–359, 2017.

[14] E. J. Brisbois, H. Handa, T. C. Major, R. H. Bartlett, and M. E. Meyerhoff, "Long-term nitric oxide release and elevated temperature stability with s-nitroso-n-acetylpenicillamine (snap)-doped elast-eon e2as polymer," *Biomaterials*, vol. 34, no. 28, pp. 6957–6966, 2013.

[15] A. Colletta, J. Wu, Y. Wo, M. Kappler, H. Chen, C. Xi, and M. E. Meyerhoff, "S-nitroso-n-acetylpenicillamine (snap) impregnated silicone foley catheters: a potential biomaterial/device to prevent catheter-associated urinary tract infections," *ACS biomaterials science & engineering*, vol. 1, no. 6, pp. 416–424, 2015.

[16] E. J. Brisbois, T. C. Major, M. J. Goudie, R. H. Bartlett, M. E. Meyerhoff, and H. Handa, "Improved hemocompatibility of silicone rubber extracorporeal tubing via solvent swelling-impregnation of s-nitroso-n-acetylpenicillamine (snap) and evaluation in rabbit thrombogenicity model," *Acta biomaterialia*, vol. 37, pp. 111–119, 2016.

[17] E. J. Brisbois, M. Kim, X. Wang, A. Mohammed, T. C. Major, J. Wu, J. Brownstein, C. Xi, H. Handa, R. H. Bartlett, *et al.*, "Improved hemocompatibility of multilumen catheters via nitric oxide (no) release from s-nitroso-n-acetylpenicillamine (snap) composite filled lumen," *ACS applied materials & interfaces*, vol. 8, no. 43, pp. 29270–29279, 2016.

[18] Y. Hattori, M. Suzuki, S. Hattori, and K. Kasai, "Globular adiponectin upregulates nitric oxide production in vascular endothelial cells," *Diabetologia*, vol. 46, no. 11, pp. 1543–1549, 2003.

[19] K. Marr, D. Jakimovski, M. Mancini, E. Carl, and R. Zivadinov, "Jugular venous flow quantification using doppler sonography," *Ultrasound in medicine & biology*, vol. 44, no. 8, pp. 1762–1769, 2018.

[20] P. W. Rand, E. Lacombe, H. E. Hunt, and W. H. Austin, "Viscosity of normal human blood under normothermic and hypothermic conditions," *Journal of Applied Physiology*, vol. 19, no. 1, pp. 117–122, 1964.

[21] H. Ren, J. L. Bull, and M. E. Meyerhoff, "Transport of nitric oxide (no) in various biomedical grade polyurethanes: measurements and modeling impact on no release properties of medical devices," *ACS biomaterials science & engineering*, vol. 2, no. 9, pp. 1483–1492, 2016.

[22] L. Höfler, D. Koley, J. Wu, C. Xi, and M. E. Meyerhoff, "Electromodulated release of nitric oxide through polymer material from reservoir of inorganic nitrite salt," *RSC advances*, vol. 2, no. 17, pp. 6765–6767, 2012.

[23] H. Ren, A. Colletta, D. Koley, J. Wu, C. Xi, T. C. Major, R. H. Bartlett, and M. E. Meyerhoff, "Thromboresistant/anti-biofilm catheters via electrochemically modulated nitric oxide release," *Bioelectrochemistry*, vol. 104, pp. 10–16, 2015.

[24] N. Barraud, M. V. Storey, Z. P. Moore, J. S. Webb, S. A. Rice, and S. Kjelleberg, "Nitric oxide-mediated dispersal in single-and multi-species biofilms of clinically and industrially relevant microorganisms," *Microbial biotechnology*, vol. 2, no. 3, pp. 370–378, 2009.

[25] N. Barraud, "Nitric oxide-mediated differentiation and dispersal in bacterial biofilms," *School of Biotechnology and Biomolecular Sciences*, 2007.

[26] N. Barraud, D. J. Hassett, S.-H. Hwang, S. A. Rice, S. Kjelleberg, and J. S. Webb, "Involvement of nitric oxide in biofilm dispersal of pseudomonas aeruginosa," *Journal of bacteriology*, vol. 188, no. 21, pp. 7344–7353, 2006.

[27] X. Liu, M. J. Miller, M. S. Joshi, H. Sadowska-Krowicka, D. A. Clark, and J. R. Lancaster, "Diffusion-limited reaction of free nitric oxide with erythrocytes," *Journal of biological chemistry*, vol. 273, no. 30, pp. 18709–18713, 1998.

[28] T. Ishida, Y. Duguet, and T. Tsukahara, "Transitional structures in annular poiseuille flow depending on radius ratio," *Journal of Fluid Mechanics*, vol. 794, 2016.

Chapter IV

Conclusion and Future Directions

4.1 The Convection-Diffusion Equation Solver

The solver offers significant improvement to simulation outcomes of the convection-diffusion equation over existing commercial solvers in domains separated by boundaries of flow. Stable solutions can be obtained around the area of interest for high Péclet numbers. It also offers freedom of choosing arbitrary flux limiters depending on amount of stabilization required. We envision this solver to play an irreplaceable role in our design of anti-infection catheters and we hope that the numerical methods described in this paper can assist other researchers that are exploring similar problems that involves a boundary of flow and experiencing difficulties in resolving large gradients in the solution. There are a few areas of potential improvements detailed below.

This solver does not guarantee absolute stability or the TVD property. Solutions have a chance of going negative due to the following reasons. First, the MPFA L-method does not limit its gradients. This may produce negative interpolated values in some elements when using extended stencils. Second, the unit vectors used in approximating the gradients in the convection flux stencil may not be exact and may result in instability. Third, we used the single instruction, multiple data (SIMD)

operations in calculating floating point operations in our implementation for speed, which may result in a small amount of uncertainty in the calculations. We are trading off some accuracy for higher parallelization and speed for this solver, but advanced programming techniques such as the use of MPI library in conjunction with high performance computing clusters will allow us to use more precise floating point routines.

Directional limiting, such as the methods we proposed in this paper, is relatively fast to implement and easy to compute, but can be too restrictive on limiting the gradients. Berger et al. [1] have proposed a linear programming method that finds the optimal gradients by solving an optimization problem. In the future, we plan to investigate the effects using alternative gradient limiting strategies or stencils, such as the one proposed by Berger et al. However, we did not implement this strategy. Solving optimization problems requires significantly more resource then attempting to attempting to resolve a fixed stencil and can potentially drag down the performance of the solver.

The flux calculation is only formulated for explicit time stepping and we used the Dormand-Prince method. The time stepping is highly accurate, but can restrict the size of the time step we take due to the Courant-Friedrichs-Lewy (CFL) condition [2]. With high velocity flows relatively to the problem size, resolution of the solution in the direction of flow might be traded off for higher computing speed. An implicit time stepping method could be used to avoid small time steps in case of high velocity flows.

The current solver requires quadrilateral meshes for 2D and hexagonal meshes for 3D. These meshes are difficult to generate automatically so hand meshing is our current choice. This trade off is to favor the resolution of boundary layers in

the system. To improve the user-friendliness of this solver, some semi-automatic routines, such as the blockmesh utility provided in the OpenFOAM [3] packages, could be useful.

4.2 Simulations of NO-Releasing Catheters

The importance of the simulations are mainly twofold: providing access of NO in a NO-releasing catheter in an *in vivo* setting; complimenting the experimental results from animal studies and replacing large-scale animal studies with simulations. We have shown that more than 99% of stock NO will be cleared from the solution without a stable NO source in 12 minutes. We have additionally determined that the time for NO to reach steady-state in a 7-Fr dual lumen catheter is about 10.5 minutes.

Significant difficulties exist in simulating a NO-releasing catheter using the strategy of SNAP impregnation, due to the fact that the release kinetics of SNAP is not well understood. Release of NO corresponds to the humidity level and temperature [4], but no quantitative studies have been performed to determine the relationship of NO release with respect to humidity, temperature, and wt % of SNAP inside the catheter. Experimental studies will be important as a precursor to simulating the NO profile in this case.

Simulations with respect to generating NO electrochemically has obtained some success. In these simulations, one distinct advantage of this strategy has not been touched yet: the NO source can be turned on or off. Future simulations should attempt to construct an optimal periodic operating profile of NO so that the device life can be extended to maximum while delivering the minimum amount of NO possible to achieve the antithrombotic and antibacterial effects.

As we have touched in Chapter III, the most severe restriction to our simulation

is the lack of modeled reactions. Further simulations should incorporate the effect of NO being consumed by red blood cells. To avoid adding additional complexity to the simulation, we suggest modeling the reaction between the red blood cells and NO to be a first order reaction with $k = 385\text{s}^{-1}$ as stated in Section 3.5. Nitric oxide can also be consumed by oxygen inside the polymer domain due to high solubility of oxygen [5], but the kinetics of such reactions are less clearly characterized.

The current implementation of the solver assumes isotropic diffusion in each domain and uniform partition coefficients. Transport of NO does involve partition coefficients [6] and can be studied, but will require slight modifications to the solver.

We mainly discuss potential future design considerations for NO release with an electrochemical source. Catheters come in many geometries with various diameters and number of lumens [6]. The diameter of the catheters are often standardized in the French scale [7] and is less flexible during design of such catheters. However, the diameter of the catheter is very important since the concentration of NO decreases exponentially with the distance from the source due to diffusion. The concentration field between a 7-Fr catheter that we simulated in this thesis and a 4-Fr catheter may be significantly different and may require different doses of NO. Future simulations should take into account different sizes of the catheter.

When using multi-lumen catheters, it is highly likely that the NO source may be placed off center. If the location of the source were to be changed from the simulations proposed by this thesis, or another design of the catheter were to be proposed, it would be necessary to perform another simulation using the updated geometries to accurately access the maximum and minimum points of NO concentration at the surface of the catheter to ensure that sufficient therapeutic level of NO is achieved.

The simulation proposed in this thesis consider the liquid in the lumen(s) to

be a locking solution: i.e., when the catheter is not in use for delivering fluids or drawing blood. When flow exists in the lumen(s), additional flow components must be considered and the concentration field may look very different. Such will be the case during intravenous delivery or during dialysis sessions.

To get more accurate results, additional parameters, such as additional viscosity models, various location placement of the catheters in blood vessels, and pulsatile flow fields could be considered depending on the intended use of the catheter.

Experimental verification of the models will be difficult, partly due to the difficulty of having a NO sensor that can be used *in vivo*, and partly because the addition of a sensor might impact the flow field. The biological system is more complex and blood vessels take many shapes, so the modeled geometries may not match the ones in vivo. To experimentally verify these models, one could attempt to build a NO sensor such as using carbon fibers [8] or micro-electrodes [9] onto the surface of the catheter while retaining its original shape and attempt to collect data. Instead, one could also try scaling up the system while keeping important dimensionless parameters, such as the Péclet number intact, and measure the system using particle imaging velocimetry for the flow field and electrochemical sensors [10] for NO concurrently.

Bibliography

[1] M. Berger, M. Aftosmis, and S. Muman, "Analysis of slope limiters on irregular grids," in *43rd AIAA Aerospace Sciences Meeting and Exhibit*, p. 490, 2005.

[2] R. Courant, K. Friedrichs, and H. Lewy, "On the partial difference equations of mathematical physics," *IBM journal of Research and Development*, vol. 11, no. 2, pp. 215–234, 1967.

[3] H. Jasak, A. Jemcov, Z. Tukovic, *et al.*, "Openfoam: A c++ library for complex physics simulations," in *International workshop on coupled methods in numerical dynamics*, vol. 1000, pp. 1–20, IUC Dubrovnik Croatia, 2007.

[4] Y. Wo, Z. Li, E. J. Brisbois, A. Colletta, J. Wu, T. C. Major, C. Xi, R. H. Bartlett, A. J. Matzger, and M. E. Meyerhoff, "Origin of long-term storage stability and nitric oxide release behavior of carbosil polymer doped with s-nitroso-n-acetyl-d-penicillamine," *ACS applied materials & interfaces*, vol. 7, no. 40, pp. 22218–22227, 2015.

[5] Y. Wang, M. Gupta, and D. A. Schiraldi, "Oxygen permeability in thermoplastic polyurethanes," *Journal of Polymer Science Part B: Polymer Physics*, vol. 50, no. 10, pp. 681–693, 2012.

[6] H. Ren, J. L. Bull, and M. E. Meyerhoff, "Transport of nitric oxide (no) in various biomedical grade polyurethanes: measurements and modeling impact on no release properties of medical devices," *ACS biomaterials science & engineering*, vol. 2, no. 9, pp. 1483–1492, 2016.

[7] K. V. Iserson, "J.-f.-b. charrière: the man behind the "french" gauge," *The Journal of emergency medicine*, vol. 5, no. 6, pp. 545–548, 1987.

[8] J.-K. Park, P. H. Tran, J. K. Chao, R. Ghodadra, R. Rangarajan, and N. V. Thakor, "In vivo nitric oxide sensor using non-conducting polymer-modified carbon fiber," *Biosensors and Bioelectronics*, vol. 13, no. 11, pp. 1187–1195, 1998.

[9] Y. Kitamura, T. Uzawa, K. Oka, Y. Komai, H. Ogawa, N. Takizawa, H. Kobayashi, and K. Tanishita, "Microcoaxial electrode for in vivo nitric oxide measurement," *Analytical chemistry*, vol. 72, no. 13, pp. 2957–2962, 2000.

[10] Y. Lee, B. K. Oh, and M. E. Meyerhoff, "Improved planar amperometric nitric oxide sensor based on platinized platinum anode. 1. experimental results and theory when applied for monitoring no release from diazeniumdiolate-doped polymeric films," *Analytical chemistry*, vol. 76, no. 3, pp. 536–544, 2004.

Part 2

Automatic Quantification of Lung Ultrasound Comets by Machine Learning

Chapter V

Introduction

5.1 Lung Ultrasound Comet: What, How, and Why?

Lung comets, or "B-lines", are visualized comet-tail like artifacts seen on ultrasound images [1]. As an acoustic reverberation artifact, they typically emanate from the surface of the lung and extends towards the bottom of the image. An example is shown in Figure 5.1. Since they likely originate from alveolar edema at the lung periphery, there have been many studies documenting the clinical utilities of lung comets, including differential diagnosis of cardiogenic dyspnea [2], guiding diagnosis of respiratory distress syndrome [3], assessing the ultrafiltration (UF) volume [4], as well as predicting mortality and heart failure in end-stage renal disease (ESRD) patients [5].

Use of lung comets is highly attractive as a non-invasive, non-radioactive way to manage fluid status [1]. Such measures would be beneficial for ESRD patients, as the importance of fluid management is gaining attention [6, 7, 8]. The importance of fluid management is strikingly shown by recognizing that across the 350,000 patients in the United States about 280,000 episodes per year develop due to fluid overload, over 80% of which require hospitalization from congestive heart failure, fluid overload and pulmonary edema, and costs the US around $1.7 billion annually. Management

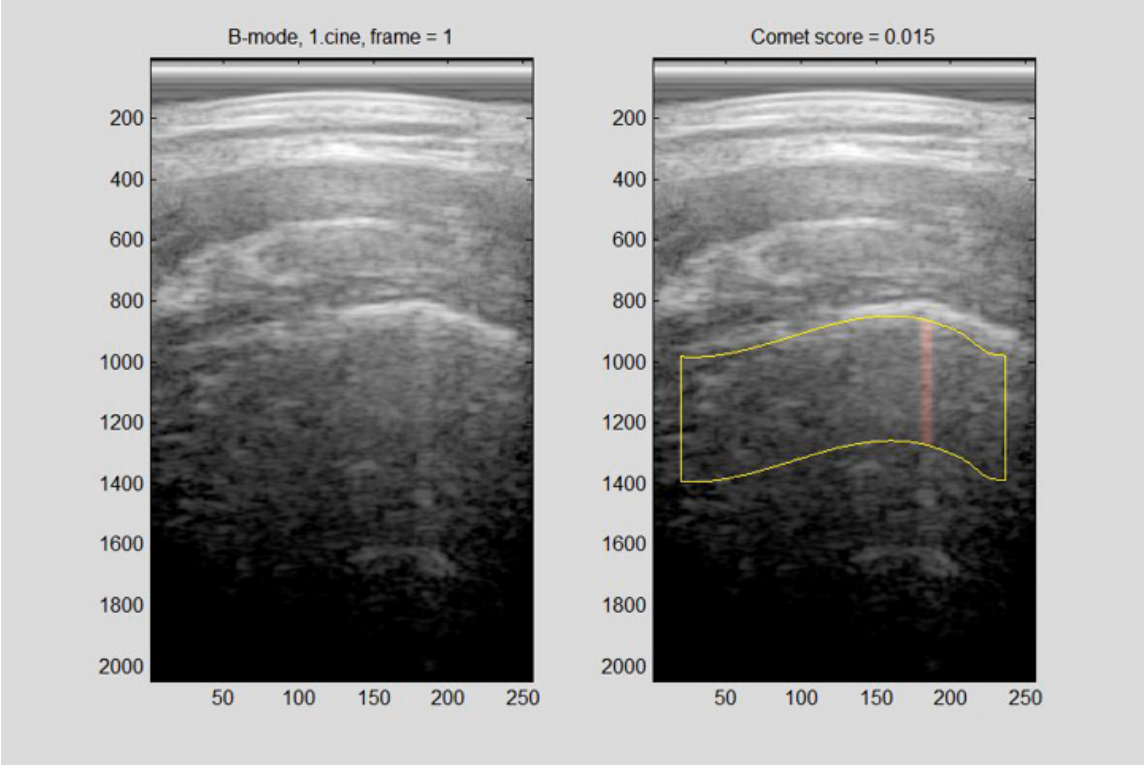

Figure 5.1: An ultrasound image with a single lung comet, highlighted in red, on the right half of the figure. Picture is from our own comet database.

of patients with our extracorporeal therapies, while avoiding hypovolemia during dialysis, and preventing fluid overload between dialysis treatments is a complicated task [9, 10, 11]. There is clear need for an improved, accurate method to analyze the fluid status in ESRD patients.

Contrasting evidence exists for using lung comets to quantify lung edema or to guide fluid management. Positive results have been widely reported by [12, 5, 13]; however, Seibel et al. [14] concluded that lung comets is currently at best semi-quantitative and not ready for bedside use as of yet. Some questioned the validity of lung comets further, by saying that lung ultrasound comets move in and out during real-time ultrasound acquisition and cannot be easily quantified [15]. The clinical data we collected also supports the point above, but this should not void the validity of lung comets and instead calls for the need to capture real-time information of the

lung comets.

It is important that we cover how lung comets are currently being quantified. The current (mostly) clinically acceptable method is to have physicians review frames at different time/location combinations and count each lung comet as if they were objects [16]. It is not difficult to notice the void in the quantifying protocol: there is no standard for lung ultrasound collection, including the device and the protocol [17]. There is substantial subjectivity in the quantifying efforts, such that the lung comets "B-lines" can be confused with "Z-lines" (an artifact emanating from the lung surface but does not extend to the edge of the image) [18]. People also question whether the lung comets should be quantified as an ordinal measure or a rating [19, 20].

To improve the clinical usefulness of lung comets, a standard for clinical collection of lung comets should be formulated, since the choice of probe, level of expertise, and length of the ultrasound cine loop affect the counting result [17]. More importantly, excessive ultrasound energy to the lungs have shown to cause lung injury in animal models and creates lung comets due to hemorrhage [21]. However, this is out of the scope of our discussion.

Intra-class correlation (ICC) is typically used to access the reliability between measurements. When the comets are counted as objects, Anderson et al. [22] reported the absolute ICC ranges from 0.85 to 0.89; however, a reader study by Gullett et al. [20] pictured a significant different story such that the inter-observer ICC of the same images ranges from 0.372 to 0.820 depending on the zone, and reinterpretation of one single set of images in randomized fashion by two experts yielded ICCs of 0.697 and 0.647. Reliable measurements typically require an ICC of 0.750 or higher [23]. An objective measure to quantify the lung comets is needed to decrease the

subjectivity contained in the measurements.

This part of the thesis will cover the efforts we have made to establish such an objective measure, including image processing and different machine learning methods. We will also provide our insight to the path of a more objective and consistent measure of lung comets.

5.2 Organization of Part 2

Part 2 of this thesis is organized as follows:

- Chapter VI (Data Collection of Lung Ultrasound Images and Initial Image Processing Analysis) covers the image processing methods we have attempted to quantify the comets and various assessment scores we have used towards quantifying lung comets.
- Chapter VII (Quantifying Lung Ultrasound Comets with a Convolutional Neural Network: Initial Clinical Results) describes our initial efforts to use an AlexNet-like neural network that outputs a single number (the number of comets) with a given input image. It also describes the first labeled lung comet database that we generated.
- Chapter VIII (Automatic Segmentation of Lung Ultrasound Comets by Machine Learning: An Attempt) records the current approaches that we take to quantify lung comets - by using a segmentation neural network based on a U-Net. It describes a second labeled lung comet database that we collected. At the end of the chapter, we will offer visions for future directions towards quantifying lung comets.

Bibliography

[1] Z. Jambrik, S. Monti, V. Coppola, E. Agricola, G. Mottola, M. Miniati, and E. Picano, "Usefulness of ultrasound lung comets as a nonradiologic sign of extravascular lung water," *The American journal of cardiology*, vol. 93, no. 10, pp. 1265–1270, 2004.

[2] L. Gargani, F. Frassi, G. Soldati, P. Tesorio, M. Gheorghiade, and E. Picano, "Ultrasound lung comets for the differential diagnosis of acute cardiogenic dyspnoea: A comparison with natriuretic peptides," *European journal of heart failure*, vol. 10, no. 1, pp. 70–77, 2008.

[3] R. Copetti, L. Cattarossi, F. Macagno, M. Violino, and R. Furlan, "Lung ultrasound in respiratory distress syndrome: a useful tool for early diagnosis," *Neonatology*, vol. 94, no. 1, pp. 52–59, 2008.

[4] X.-K. Liang, L.-J. Li, X.-H. Wang, X.-X. Wang, Y.-D. Wang, and Z.-F. Xu, "Role of lung ultrasound in adjusting ultrafiltration volume in hemodialysis patients," *Ultrasound in medicine & biology*, vol. 45, no. 3, pp. 732–740, 2019.

[5] C. Zoccali, C. Torino, R. Tripepi, G. Tripepi, G. D'Arrigo, M. Postorino, L. Gargani, R. Sicari, E. Picano, F. Mallamaci, *et al.*, "Pulmonary congestion predicts cardiac events and mortality in esrd," *Journal of the American Society of Nephrology*, vol. 24, no. 4, pp. 639–646, 2013.

[6] A. K. Cheung, M. J. Sarnak, G. Yan, M. Berkoben, R. Heyka, A. Kaufman, J. Lewis, M. Rocco, R. Toto, D. Windus, *et al.*, "Cardiac diseases in maintenance hemodialysis patients: results of the hemo study," *Kidney international*, vol. 65, no. 6, pp. 2380–2389, 2004.

[7] J. P. Kooman, F. M. van der Sande, and K. M. Leunissen, "Role of sodium and volume in the pathogenesis of hypertension in dialysis patients," *Blood purification*, vol. 22, no. 1, pp. 55–59, 2004.

[8] S. A. Morse, A. Dang, V. Thakur, R. Zhang, and E. Reisin, "Hypertension in chronic dialysis patients: pathophysiology, monitoring, and treatment," *The American journal of the medical sciences*, vol. 325, no. 4, pp. 194–201, 2003.

[9] T. J. Arneson, J. Liu, Y. Qiu, D. T. Gilbertson, R. N. Foley, and A. J. Collins, "Hospital treatment for fluid overload in the medicare hemodialysis population," *Clinical Journal of the American Society of Nephrology*, vol. 5, no. 6, pp. 1054–1063, 2010.

[10] E. Saad, B. Charra, and D. S. Raj, "Hypertension in hemodialysis patients: Hypertension control with daily dialysis," in *Seminars in dialysis*, vol. 17, pp. 295–298, Wiley Online Library, 2004.

[11] J. Q. Jaeger and R. L. Mehta, "Assessment of dry weight in hemodialysis: an overview," *Journal of the American Society of Nephrology*, vol. 10, no. 2, pp. 392–403, 1999.

[12] V. Panuccio, G. Enia, R. Tripepi, C. Torino, M. Garozzo, G. G. Battaglia, C. Marcantoni, L. Infantone, G. Giordano, M. L. De Giorgi, *et al.*, "Chest ultrasound and hidden lung congestion in peritoneal dialysis patients," *Nephrology Dialysis Transplantation*, vol. 27, no. 9, pp. 3601–3605, 2012.

[13] F. Mallamaci, F. A. Benedetto, R. Tripepi, S. Rastelli, P. Castellino, G. Tripepi, E. Picano, and C. Zoccali, "Detection of pulmonary congestion by chest ultrasound in dialysis patients," *JACC: Cardiovascular Imaging*, vol. 3, no. 6, pp. 586–594, 2010.

[14] A. Seibel, P. Zechner, A. Berghold, M. Holter, P. Braß, G. Michels, N. Leister, G. Gemes, R. Donauer, R. Giebler, *et al.*, "B-lines for the assessment of extravascular lung water: just focused or semi-quantitative?," *Acta Anaesthesiologica Scandinavica*, 2020.

[15] G. Soldati, R. Copetti, and S. Sher, "Can lung comets be counted as "objects"?," *JACC: Cardiovascular Imaging*, vol. 4, no. 4, pp. 438–439, 2011.

[16] V. E. Noble, A. F. Murray, R. Capp, M. H. Sylvia-Reardon, D. J. Steele, and A. Liteplo, "Ultrasound assessment for extravascular lung water in patients undergoing hemodialysis: time course for resolution," *Chest*, vol. 135, no. 6, pp. 1433–1439, 2009.

[17] E. Pivetta, F. Baldassa, S. Masellis, F. Bovaro, E. Lupia, and M. M. Maule, "Sources of variability in the detection of b-lines, using lung ultrasound," *Ultrasound in medicine & biology*, vol. 44, no. 6, pp. 1212–1216, 2018.

[18] K. See, V. Ong, S. Wong, R. Leanda, J. Santos, J. Taculod, J. Phua, and C. Teoh, "Lung ultrasound training: curriculum implementation and learning trajectory among respiratory therapists," *Intensive care medicine*, vol. 42, no. 1, pp. 63–71, 2016.

[19] J.-J. Rouby, C. Arbelot, Y. Gao, M. Zhang, J. Lv, Y. An, W. Chunyao, D. Bin, C. S. Valente Barbas, F. L. Dexheimer Neto, *et al.*, "Training for lung ultrasound score measurement in critically ill patients," *American journal of respiratory and critical care medicine*, vol. 198, no. 3, pp. 398–401, 2018.

[20] J. Gullett, J. P. Donnelly, R. Sinert, B. Hosek, D. Fuller, H. Hill, I. Feldman, G. Galetto, M. Auster, and B. Hoffmann, "Interobserver agreement in the evaluation of b-lines using bedside ultrasound," *Journal of critical care*, vol. 30, no. 6, pp. 1395–1399, 2015.

[21] D. L. Miller, Z. Dong, C. Dou, and K. Raghavendran, "Pulmonary capillary hemorrhage induced by different imaging modes of diagnostic ultrasound," *Ultrasound in medicine & biology*, vol. 44, no. 5, pp. 1012–1021, 2018.

[22] K. L. Anderson, J. M. Fields, N. L. Panebianco, K. Y. Jenq, J. Marin, and A. J. Dean, "Inter-rater reliability of quantifying pleural b-lines using multiple counting methods," *Journal of Ultrasound in Medicine*, vol. 32, no. 1, pp. 115–120, 2013.

[23] D. V. Cicchetti, "Guidelines, criteria, and rules of thumb for evaluating normed and standardized assessment instruments in psychology.," *Psychological assessment*, vol. 6, no. 4, p. 284, 1994.

Chapter VI

Data Collection of Lung Ultrasound Images and Initial Image Processing Analysis

6.1 Introduction

Lung ultrasound (USN) has recently been reported to be useful in evaluating pulmonary edema [1, 2, 3]. Acoustic reverberations, identified visually as lung water "comets", due to pulmonary edema have been correlated with mortality, incidence of cardiac events, and hospitalization [3], and patients with severe congestion exhibited a 4.2× higher mortality and 3.2× increased risk of cardiac morbidity compared to patients without lung congestion. At the same time, the validity of using lung comets as a quantitative tool is disputed [4] . The current common practice of estimating comets has relied on the observation of still frame ultrasound images; yet our own clinical observations and others [4] are that lung comets vary during the real time ultrasound lung examination. We therefore sought to develop and test an objective and quantitative image-processing method that would estimate comet count and comet signal strength captured over a series of frames stored in standard ultrasound cine loops. We further sought to investigate if this objective algorithmic approach would detect clinically meaningful associations between lung comet counts and parameters associated with fluid status in hemodialysis outpatients.

6.2 Methods

6.2.1 Clinical Data Collection

Twenty stable hemodialysis outpatients (17 men and 3 women) were enrolled at the University of Michigan Dialysis outpatient program after Institutional Review Board approval and informed consent. Lung ultrasound was performed using a commercially available ultrasound device (7.5 MHz, vascular or small parts probe, Interson Corporation, Pleasanton, Calif., USA). Ultrasound scanning was performed through the intercostal (IC) spaces in the anterior and lateral chest for the right and left hemi-thorax at the beginning and end of dialysis treatment using data collection methods modeled after [3] . Patients were recumbent in their dialysis reclining chairs during the ultrasound examination. To preserve modesty, privacy curtains were drawn in the dialysis unit for all subjects and data collection was limited to the anterior apex of the chest for women subjects. The ultrasound data were collected and saved as 2 s cine loops (video loops) at 16 frames per second, or 32 frames for each IC space (generally 32 IC spaces for men and 12 for women). Early in the study, abundant lung comets were observed in the apical and parasternal IC spaces; therefore, to construct a uniform dataset for analysis from men and women, the bilateral parasternal IC spaces 1 through 4 bilaterally (eight IC spaces per subject) were used for clinical study data analysis. Thus, the total ultrasound dataset for this analysis were 16 cine loops per subject (eight at the beginning and end of dialysis per subject) for 20 subjects totaling 320 cine loops per observer for two observers (640 cine loops), consisting of 32 frames per loop or a total of 20,480 frames of ultrasound data. Additional cine loops were archived for future analysis.

Clinical data collected for evaluation were prescribed and delivered Ultrafiltration (UF), beginning dialysis BP, dialysis treatment, blood volume monitoring data using

the CritLine® Monitor (CLM, Fresenius Medical Care North America) and if present in subject's clinical data echocardiographic ejection fraction (EF); EF was present for 13 of the 20 subjects. Since blood volume monitoring data were stable (no C profiles) in this clinically stable outpatient population, the percent blood volume (%BV) data collected for analysis used for analysis were the final BV reduction (final BV) and the mean BV reduction per hour (BV slope). The lung comet score (comet count, comet fraction) was generated in MATLAB (Mathworks, Natick, Mass., USA) with our laboratory image-processing algorithms. The pre-dialysis comet scores were analyzed against the clinical parameters available by multiple linear regression. In addition, the pre-dialysis comet scores were compared to the post-dialysis comet scores using a two-sided t test.

6.2.2 Image Processing and ROI Collection

The image-processing architecture was developed using Matlab (Mathworks, Natick, Mass., USA) and image loops were processed offline, after ultrasound acquisition. The acquired B-mode images were stored in the polar format (i.e., range, beam coordinates), before scan conversion. This is advantageous for comet detection since the resolution is spatially invariant in this representation, resulting in consistent comet widths regardless of lateral position or depth. Figure 6.1a shows the relationship between polar coordinates (right) and physical pixel (left) locations. To acquire image data, the Interson system mechanically sweeps a single element transducer across the $\pm 30^o$ field of view and back. As the transducer moves, it transmits and receives ultrasound signals at a regular rate to form image frames. The mechanical acquisition results in slower sweep speeds near the edges of the field of view compared to the center, producing spatially varying beam spacing. Correction of this distortion is necessary to properly measure comet strength, size, and position. Using analytically

determined beam positions provided by the manufacturer, a uniform beam sampling is produced by linear interpolation of B-mode images.

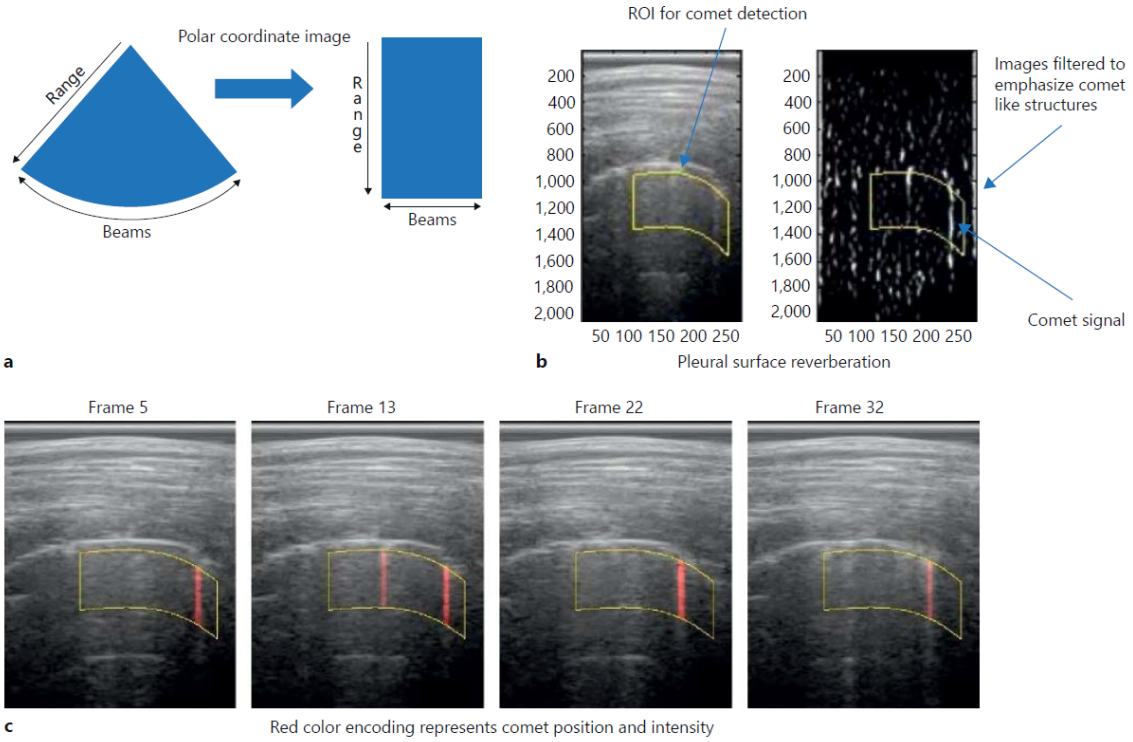

Figure 6.1: (a) Polar coordinate representation of image; (b) Image filtering for comet detection; Combined B-mode and comet detection; (c) images for visualization and assessment.

Comet detection is performed in a user-defined region of interest (ROI). In this system, the operator defines points on the lung surface. A spline is generated as the upper border of the ROI from the input points. The spline is extended by 1 cm or 1.5 cm below the upper border for 5 and 10 cm scan depth.. The same contour shape is used in Figure 6.1b. The operator also sets the lateral (i.e., across beam) extent of the ROI. ROI processing is critical to accommodate image quality variation. For example, the lung surface may occupy only a portion of the image field of view. In addition, lung border definition is the only user input needed for the comet assessment method presented here, which can improve reproducibility and consistency compared to techniques relying on the comet counting by the user. Also,

the ROI allows for consistent analysis of multi-frame data, an improvement of the previous, single frame analysis techniques. The ROI are stored locally to avoid re-defining the ROI for repeated analysis. The machine learning algorithm detailed in Chapter VII also used this ROI data.

Distortion-corrected B-mode image loops are processed to detect comets. This is accomplished by applying spatial and temporal matched filters designed with comet-like features in the image loop. The spacial filter is a size 5×100 moving average filter in the across-beam direction with the assumption of a 5-beam wide comet being at least 100 pixels long. The spatial filter requires the comet shape to be long and narrow. The temporal filter is an average filter across three frames. The image is then normalized with respect to the standard deviation. An example of B-mode and filtered images is presented in Figure 6.1b. The right (filtered) image is shown using a positive dynamic range. As seen by the processed image, comet-like structures are emphasized by the spatial and temporal filtering. Notice also in Figure 6.1b that the horizontal line appearing approximately at depth 1,700 from width 100–175 is the pleural surface reverberation seen when a comet is not present, and the comet B-line extending down approximately from depth 1,000 through 1,700 occurs with loss of the horizontal A-line, findings typically described as features of lung comets [2]. The horizontal A-lines are also seen to disappear below the vertical comets highlighted in Figure 6.1c.

A threshold was applied to the processed image, producing a binary image representing location and frames of strong comets. The detected comet signals can be mapped onto B-mode images for comet visualization as shown in the series of images in Figure 6.1c. In this case, the comet position and size is indicated by the red color-encoding derived from the thresholded binary image. This kind of image

output could potentially guide real-time acquisition and comet assessment.

6.3 Measurement Scores

The comet fraction is the fraction of the comet-positive pixels with respect to the number of pixels present in the ROI of the thresholded image. The comet count is then derived from the detected comet-positive pixels. Only discrete comet-positive pixels will be counted as comets: that is, either a thick comet or a thin comet will be counted as one comet. Both the comet fraction and comet count were displayed by the program used for analysis. We also briefly analyzed a third quantifying measure, the average comet width (comet width) in the number of beams and defined by:

$$\text{comet width} = \frac{\text{comet fraction}}{\text{comet count}} \times 256. \tag{6.1}$$

6.4 Results

Early in the study we confirmed the observation that B-scan images show considerable variation in comet character and number with slight motion due to transducer movement or breathing during the real time ultrasound examination (Figure 6.2).

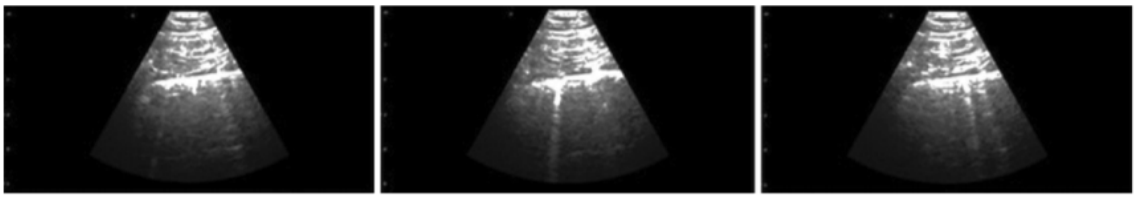

Figure 6.2: The three images show consistent character of the ultrasound speckle pattern from stable tissue above the pleural line, indicating very slight motion due to transducer movement or breathing, and the high degree of variation of the comet character, location, and number below the pleural line during a few seconds duration lung exam.

From the consistent character of the ultrasound speckle pattern, stable tissue is observed above the pleural line. This indicates that very slight motion of the transducer or slight motion with normal respiration is associated with a high degree of

variation of the comet character, location, and number below the pleural line. So comets, while somewhat distinct, are shown to be not completely "discrete" phenomena; they vary in brightness/intensity, width, length, and reverberation pattern. We adjusted for the ambiguity on comet counting and interpretation with the algorithm-based approach outlined in the methods section above. All of the twenty patients were able to successfully complete the ultrasound scanning during their standard dialysis treatment. The demographic and clinical parameters of the twenty patients are included in Table 6.1.

Table 6.1: Demographic and clinical data

Clinical Parameter	Range (Mean ± SD)
Age (years)	53±14
Weight (kg)	96±24
BMI	31.5±7.6
Male Sex%	85% (17/20)
Diabetes %	55% (11/20)
Hypertension Documented %	95% (19/20)
Congestive Heart Failure Documented %	5% (1/20)
Coronary Artery Disease Documented %	20% (4/20)
Diastolic Blood Pressure (mmHg)	75±11
Systolic Blood Pressure (mmHg)	134±29
Ejection Fraction %	51±17

The output of the analysis program was stored in a plain text file and then analyzed using OriginPro 9 (OriginLab Corporation, Northampton, Mass., USA) for correlation. A series of relationships between comet count and clinical parameters were examined. The pre-dialysis comet count was analyzed against the following parameters using linear regression: blood pressure (BP), ejection fraction (EF), subject body weight, subject age, BMI, and blood volume (BV) indicators during the course of dialysis such as final BV reduction (final BV), and mean BV reduction per hour (BV slope). Among these parameters, diastolic blood pressure (Figure 6.3a: $r = 0.534$, $p = 0.015$), and subject age (Figure 6.3b: $r = -0.446$, $p = 0.049$) showed significance at the 0.05 level. A combination of Final %BV and EF (Final

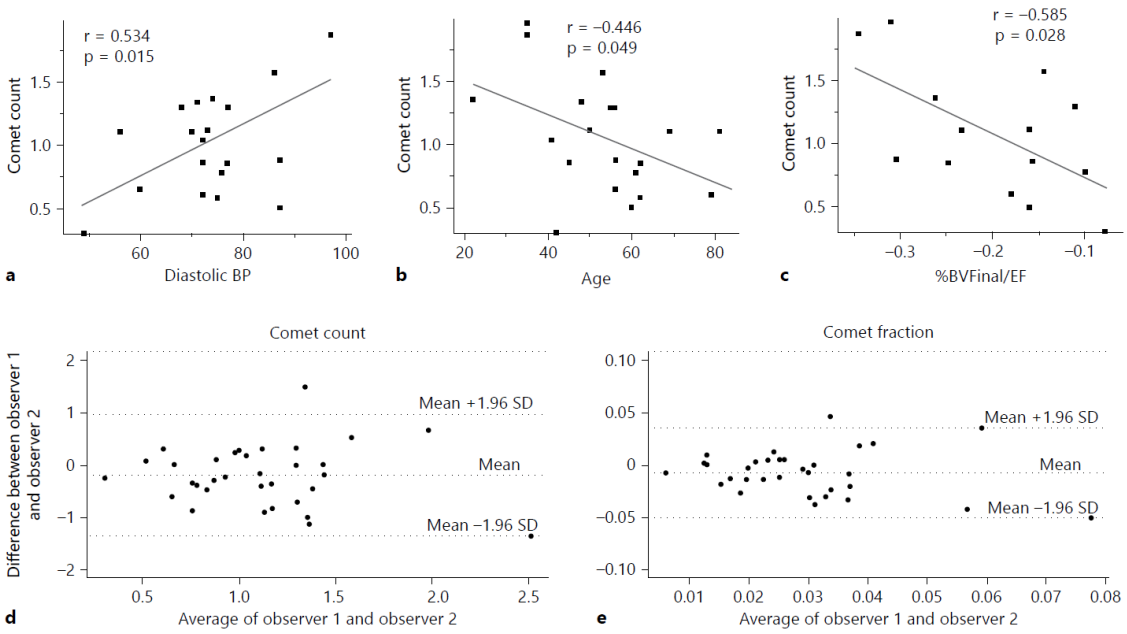

Figure 6.3: Correlation between pre-dialysis comet count and clinical parameters diastolic BP (a), age (b), ratio %BVFinal to EF (c), Bland-Altman plot of two observers for comet count (d), and comet fraction (e).

BV divided by EF) was also found significant (Figure 6.3c: $r = -0.585$, $p = 0.028$), although Final BV ($r = -0.427$, $p = 0.061$) and EF ($r = -0.377$, $p = 0.184$) both showed borderline significance. The rest factors were not found to be significant.

Comet fraction and comet count were closely correlated as a result of the inherent inter-relationship between these two metrics ($r = 0.973$, $p < 0.001$). Therefore, comet fraction yielded similar results. Diastolic blood pressure ($r = 0.570$, $p = 0.009$), subject age ($r = -0.461$, $p = 0.041$), and Final %BV/EF ($r = -0.602$, $p = 0.023$) were found to be significant. Other parameters mentioned above were not found to be significant with comet fraction.

To examine if comet counts or fractions changed during dialysis, a two-sided, paired t test was performed. The results were negative with $p = 0.921$ for comet count, and $p = 0.874$ for comet fraction. A separate linear regression model suggested the decrease in comet count during the dialysis period (defined as the comet count

at the beginning of dialysis minus the comet count at the end of dialysis) strongly correlates neither with the UF achieved ($r = 0.109$, $p = 0.522$) nor with the change in mean arterial BP ($r = 0.035$, $p = 0.843$). The full results of the analysis can be found in Table 6.2.

Table 6.2: Full results of comet analysis: comet count and comet fraction versus clinical parameters. BP: Blood Pressure. %BV: Percent blood volume change. Significance levels: *: $p < 0.05$; **: $p < 0.01$; ***: $p < 0.001$.

Comet Score	Clinical Parameter	Unit	Range	R-value	p-value	Sig.
	Diastolic BP	mmHg	75±11	0.534	0.015	*
	Systolic BP	mmHg	134±29	0.249	0.289	(NS)
	Final %BV	percent	-8.5±4.7	-0.427	0.061	(NS)
	Mean BV/h	percent/h	-2.2±1.2	-0.360	0.119	(NS)
	Ejection Fraction	-	51±17	-0.377	0.184	(NS)
Pre-Dialysis	Final %BV/EF	-	-	-0.585	0.028	*
Comet Count	Subject Dry Weight	kg	96±24	0.294	0.208	(NS)
	Subject Age	years old	53±14	-0.446	0.049	*
	Subject BMI	kg/m2	31.5±7.6	0.217	0.358	(NS)
	Diastolic BP	mmHg	75±11	0.570	0.009	**
	Systolic BP	mmHg	134±29	0.268	0.253	(NS)
	Final %BV	percent	-8.5±4.7	-0.355	0.124	(NS)
	Mean BV/h	percent/h	-2.2±1.2	-0.283	0.226	(NS)
	Ejection Fraction	-	51±17	-0.447	0.109	(NS)
Pre-Dialysis	Final %BV/EF	-	-	-0.602	0.023	*
Comet Fraction	Subject Dry Weight	kg	96±24	0.279	0.234	(NS)
	Subject Age	years old	53±14	-0.461	0.041	*
	Subject BMI	kg/m2	31.5±7.6	0.167	0.480	(NS)
Comet Fraction	Comet Count	-	-	0.973	< 0.001	***
Decreased	UF Achieved	L	3.1±1.7	0.109	0.522	(NS)
Comet Count	Mean BP Change	mmHg	2.23±11.55	0.035	0.843	(NS)
Pre vs. Post Dialysis Comet Count		-	-	-	0.921	(NS)
Pre vs. Post Dialysis Comet Fraction		-	-	-	0.874	(NS)

The comet width correlates positively with both comet fraction ($p < 0.001$, Adj. $R^2 = 0.70$) and comet count ($p < 0.001$, Adj. $R^2 = 0.58$), which is reasonable due to the comet width being a derived property of the two measures. It is also positively correlated with diastolic BP ($p = 0.026$, $r = 0.498$) and negatively correlated with the ejection fraction ($p = 0.036$, $r = -0.564$).

To examine the amount of error introduced by different observers, an inter-observer analysis was performed. The correlation coefficient between the two ob-

servers did not show a high agreement on either comet count ($r = 0.368$) or comet fraction ($r = 0.310$) and the Bland-Altman plot of the observers is shown in Figure 6.3de. The inter-observer variation for both comet count and comet fraction observations were within two standard deviations for most measurements, even though the inter-observer variation was high.

6.5 Discussion

There is increasing evidence for the potential value of ultrasound lung comets in assisting with pulmonary fluid status assessment [1, 2, 3, 5, 6]. However, the variation and fluctuation of comet character as well as questions about using them as a quantitative measure [4] highlight the need for automated and objective tools such as the algorithm in this study. Fundamentally, lung water comets result from acoustic reverberation caused by acoustic impedance mismatches [5, 6, 7, 8]. This reverberation results in multiple 'comet tail' artifacts generated in the image at the lung surface; water-thickened interlobular septa near the pleural surface may be the source of this reverberation pattern in the ultrasound images [5, 6, 7, 8].

However, this explanation of comet generation does not necessarily mean that some "quantity" of comet number or character can be translated directly into a quantitative measure of pulmonary edema. Additional fundamental work is yet to establish the basis for lung water quantification and to relate this quantity to ultrasound comet generation, and to clinical findings. Notwithstanding this observation, the clinical ultrasound data and correlations with clinical findings that we observed points to the fact that further work be performed using this or similar approaches.

In this pilot project, our purpose was to develop and clinically test an objective measurement algorithm-based approach to detect comet patterns in standard

DICOM ultrasound B-mode cine loops (video sequences) and calculate various metrics associated with these artifacts. This type of approach allows the processing of considerably more data than can be performed manually by the clinician. For example, in this study more than 20,000 frames of data were processed for these 20 subjects, offering the possibility of extracting considerably more information from a rich ultrasound dataset that may be routinely collected in a short lung ultrasound examination. While algorithm-based quantification standardizes ultrasound comet analysis and allows for large amounts of data to be incorporated into the examination, additional sources of measurement variation remain. Bland-Altman analysis showed comparable measurements between observers, yet the inter-observer spread indicated differences in image acquisition between observers likely from small differences in probe position. The comet fluctuation during the measurements we observed and the inter-observer variation do suggest that standardization of acquisition will improve quantification. The user-defined ROI may also be a source of measurement variation although this appeared more consistent during the analysis. Both of these variables require more study.

We had hypothesized that if the lung ultrasound comets were related directly to lung fluid content that there would be a detectable difference from beginning to end of dialysis using this approach. However, we did not detect such a difference in this stable patient population. This is in contrast with other investigators' findings that comets were reduced with fluid removal during dialysis [9] in hospitalized patients. One possible explanation is this smaller pilot study was underpowered to detect this change in this stable outpatient population. We have started a study in hospitalized dialysis patients to investigate this further. The positive findings are interesting in that lower cardiac ejection fraction accompanied by higher-end dialy-

sis reduction in intravascular blood volume was associated with greater pre-dialysis comets counts. This occurred in the absence of greater ultrafiltration targets for these patients. Patients with low ejection fraction may have reduced redistribution of fluids from extravascular compartments, including lungs and extremities, and manifest this as greater intra-dialytic reduction in relative blood volume during dialysis. This is interesting to consider in light of the greater mortality associated with greater lung water comets independently observed [3]. More study is needed to better understand the relationship between fluid compartments and the rate at which fluid shifts between compartments. Similarly, elevated blood pressure is associated with increased fluid, and this is supported by these findings of greater lung comet counts and comet fractions in patients with predialysis diastolic hypertension. The reason lower cometcounts were seen in patients with increasing age is uncertain. Future studies may benefit from intravascular or other volume status monitoring to determine how much reduction in lung water will occur with what degree of intravascular contraction during dialysis in different patient populations.

6.6 Conclusion

Algorithm-based ultrasound signal-processing methods may help objectively quantify lung ultrasound comets. This initial analysis suggests that such approaches to lung comet measurement allow operator-independent objective processing of large amounts of video ultrasound (cine loop) data; so while inter-observer ultrasound data collection remains a variable, the data analysis step may be objectively conducted. Our pilot data from this small series of stable dialysis outpatients did not detect a change in comets during single dialysis sessions, but lung comets were associated with clinically relevant cardiovascular and fluid status parameters. Further

studies are required to both explain the quantitative relationship between comets and lung water and to determine the role of lung ultrasound in the clinical setting for dialysis patients.

Bibliography

[1] V. Panuccio, G. Enia, R. Tripepi, C. Torino, M. Garozzo, G. G. Battaglia, C. Marcantoni, L. Infantone, G. Giordano, M. L. De Giorgi, *et al.*, "Chest ultrasound and hidden lung congestion in peritoneal dialysis patients," *Nephrology Dialysis Transplantation*, vol. 27, no. 9, pp. 3601–3605, 2012.

[2] F. Mallamaci, F. A. Benedetto, R. Tripepi, S. Rastelli, P. Castellino, G. Tripepi, E. Picano, and C. Zoccali, "Detection of pulmonary congestion by chest ultrasound in dialysis patients," *JACC: Cardiovascular Imaging*, vol. 3, no. 6, pp. 586–594, 2010.

[3] C. Zoccali, C. Torino, R. Tripepi, G. Tripepi, G. D'Arrigo, M. Postorino, L. Gargani, R. Sicari, E. Picano, F. Mallamaci, *et al.*, "Pulmonary congestion predicts cardiac events and mortality in esrd," *Journal of the American Society of Nephrology*, vol. 24, no. 4, pp. 639–646, 2013.

[4] G. Soldati, R. Copetti, and S. Sher, "Can lung comets be counted as "objects"?," *JACC: Cardiovascular Imaging*, vol. 4, no. 4, pp. 438–439, 2011.

[5] Z. Jambrik, S. Monti, V. Coppola, E. Agricola, G. Mottola, M. Miniati, and E. Picano, "Usefulness of ultrasound lung comets as a nonradiologic sign of extravascular lung water," *The American journal of cardiology*, vol. 93, no. 10, pp. 1265–1270, 2004.

[6] E. Picano, F. Frassi, E. Agricola, S. Gligorova, L. Gargani, and G. Mottola, "Ultrasound lung comets: a clinically useful sign of extravascular lung water," *Journal of the American Society of Echocardiography*, vol. 19, no. 3, pp. 356–363, 2006.

[7] D. Lichtenstein, G. Meziere, P. Biderman, A. Gepner, and O. Barre, "The comet-tail artifact: an ultrasound sign of alveolar-interstitial syndrome," *American journal of respiratory and critical care medicine*, vol. 156, no. 5, pp. 1640–1646, 1997.

[8] D. Lichtenstein and G. Mezière, "A lung ultrasound sign allowing bedside distinction between pulmonary edema and copd: the comet-tail artifact," *Intensive care medicine*, vol. 24, no. 12, pp. 1331–1334, 1998.

[9] V. E. Noble, A. F. Murray, R. Capp, M. H. Sylvia-Reardon, D. J. Steele, and A. Liteplo, "Ultrasound assessment for extravascular lung water in patients undergoing hemodialysis: time course for resolution," *Chest*, vol. 135, no. 6, pp. 1433–1439, 2009.

Chapter VII

Quantifying Lung Ultrasound Comets with a Convolutional Neural Network: Initial Clinical Results

7.1 Introduction

Lung ultrasound comets, or "B-Lines", are "comet-tail" artifacts that emanate from the lung surface [1]. Various lung ultrasound findings are receiving increasing attention for detecting or ruling out several lung pathologies [2, 3, 4, 5, 6]. In particular, observations of lung ultrasound comets have been related to the presence of extravascular lung water [1]. Recent evidence further suggests that these comet artifacts may useful in evaluating pulmonary edema [7, 8, 9, 10] and have the potential to predict patient outcomes [7]. These ultasound findings may be partcicularly helpful in the end stage renal disease setting where patients suffer from fluid overload and pulmonary edema [7, 9].

The current practice of identifying lung ultrasound comets, which involves physicians observing still ultrasound images, has two major limitations. The number and location of lung comets can vary during the time span of an ultrasound motion picture (cine) loop [11], meaning that the identification of comets from a single image is likely not representative of the region imaged [9]. In addition, the evaluation of lung comets can vary from observer to observer and between initial interpretation and reinterpretation by a single observer [12].

Initial steps have been taken to address the limitations by adopting an automated computer algorithm with varied degree of clinical success [9, 13, 14, 15, 16]. These previous approaches assume lung comets are pure line features and apply line detection methods on the ultrasound images. Traditional filtering and feature extraction methods were used on some of these approaches [9, 13, 14]. These methods do not sufficiently differentiate B-lines from the other line-type artifacts in the images. Validation results comparing computer counting to human counting is scarce to non-existent in many of these methods. More recently, B-line detection has been formulated as an inverse problem [15, 16]. The approach by Anantrasirichai et al. [16] has shown significant promise with a reported F1-score of 0.94 for individual comets in a 100-image pediatric ultrasound image set acquired from array transducers, but it is unclear how the approach will perform when extended to adult ultrasound images or when applied to images acquired by single element transducers.

Artificial neural networks are well established and have been successfully adapted for computer vision and classification in machine learning [17]. Unlike traditional image processing methods, neural networks would not assume lung comets as lines and hidden features from an observer may be extracted. With adequate training data support, artificial neural networks can yield a satisfactory level of accuracy in classification of images. Training these networks often require high-performance GPUs but interpretation can be computationally inexpensive. Because the accuracy of a neural network model can be determined by comparison of the output of the neural network with the observed findings by human, the performance of the algorithm can be evaluated using the human observations as the reference.

Our goal is to guide patient diagnosis and quantify lung edema by applying real-time lung comet quantification using machine learning with a portable low-cost USB

ultrasound probe in a point-of-care setting. This study is the initial step towards our goal. In this pilot study, we used a convolutional neural network as the primary algorithm to identify lung ultrasound comets to evaluate the use of neural networks in future lung ultrasound comet studies.

7.2 Methods

The data was collected under our institutional review board (IRB) approved study HUM 79017 in 2013-14 with informed consent from the subjects. A database of lung ultrasound images along with their comet counts were constructed from the collected data. The lung ultrasound measurements were performed using a commercially available USB-based portable transducer with single element mechanical scanning (7.5 MHz, small parts probe, Interson Corporation, Pleasanton, CA). Ultrasound scanning was performed through the intercostal (IC) spaces in the anterior and lateral chest for the right and left hemi-thorax using data collection methods previously reported [7, 9]. Uniform gain and power settings were used throughout the ultrasound image acquisition. The database was then used for training and testing the performance of the neural network models. The accuracy of comet count was used as the primary measure of performance of the system; in addition, the ability of the system to classify an ultrasound image as "negative, mild, or severe" was used as another measure of performance. The neural network is also deployed on a small scale of clinical data to establish its clinical significance. The clinical dataset is composed of 152 lung ultrasound loops with 32 frames each, for a total of 4864 images. These cine loops were obtained under the protocol documented in our previous paper. [9] The original study involved 20 stable hemodialysis patients, 17 men and 3 women, with two sessions of scans before and after the patients undergo dialysis. Each set of scan

contains 12 to 32 loops. [9] The methods documented below covers the construction of the database, the structure of the neural network, the considerations to address overfitting, and the computing environment.

7.2.1 Database Construction

The 152 cine loops were randomly selected from a pool of more than 500 loops, composed of the first to thirteenth cine loop from each scan session. Locations #1-13 were chosen because these loops were found to be relatively comet rich. A total of 4864 ultrasound images were obtained during the above process. These images are then randomly pooled into three sets: a training set (3584 images, 73.7%), a cross-validation set (640 images, 13.2%) and a test set (640 images, 13.2%). The images were imported into an in-house GUI for data collection and were labeled per the number of comets present. The region of interest (ROI), recycled from our previous study [9], defines a 10 millimeter region just below the lung border, where the lung comets are typically present. The available labels for each image ranges are every integer between 0 and 6, for a total of seven available labels because 6 is the observed maximum number of comets present in the image database. Due to the author's intention of performing a feasibility study, the lung comets were not segmented and labeled individually; instead, the images were labeled with the number of comets present in the ROI stored as the label. The observer had no knowledge of the clinical parameters of the subject, the comet counts from the previous study, or which set the image would fall into. The ROI was stored instead of the whole picture because the ROI is the most comet rich and the number of pixels contained in the ROI (410×256) is much smaller than the whole image (2048×256). The ROI was then rescaled to a resolution of 128×128 for a further reduction in dimensionality of input. The comets are seen in the original image as 5-10 pixels long and hundreds of pixels

wide according to the observer, so they can still be seen after resizing. All images are in grayscale. A workflow of the labeling process is available in Figure 7.1.

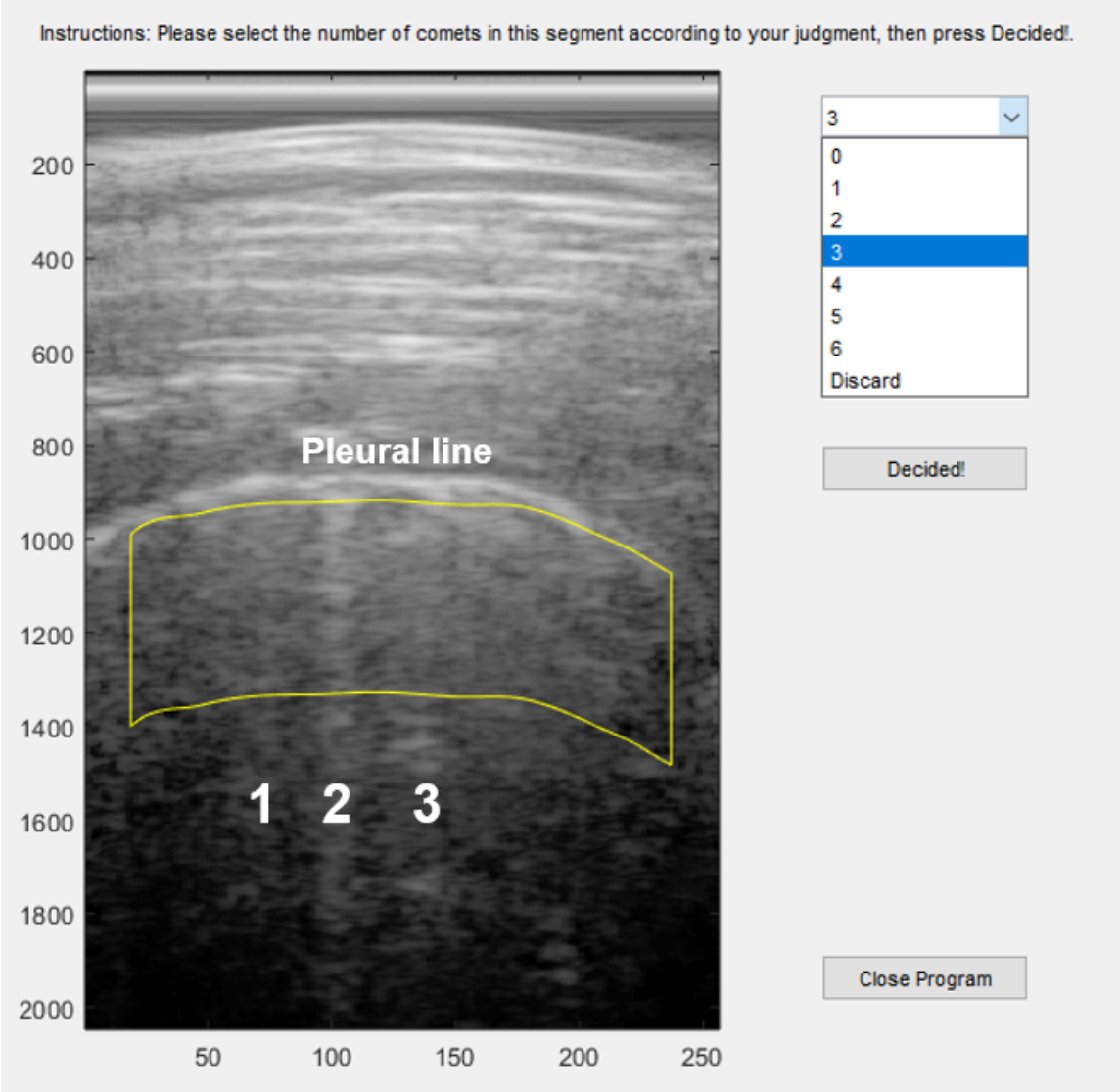

Figure 7.1: Dataset Generation. Step 1: Manually count the number of comets present in the ROI of the image (example image: 3 comets). The three comets are shown with a white text overlay. Step 2: Choose the label corresponding to the number of comets present (example image: 3). Step 3: Save the rescaled image with the label.

7.2.2 Structure of the Neural Network

The architecture of a basic convolutional neural network can contain three types of layers: convolutional layers, pooling layers, and fully connected layers. The convolutional layer uses a small kernel and extracts features from a larger image. The

number of convolutional layers tends to increase with the depth of the neural network. The pooling layer effectively down-samples an image and decreases its size. The fully connected layer computes its results from all the parameters from the previous layers and is often used for categorization purposes. An activation function can appear along with these layers above to regulate the output of these layers and apply nonlinearity to their output.

This neural network was constructed with considerations of a relatively high dimension of input and a small size of the training set. Rectified linear units (ReLU) were chosen as the activation functions for the neurons due to a reported faster training speed and the ability to prevent overfitting [18]. Overlapping average pooling with a window size of 3×3 and stride 2 was used across all layers except for the first layer, which uses max pooling of the same window size. This pooling scheme generated the highest accuracy on the validation set.

The final neural network contains four convolutional layers and a fully connected layer. Each of the four convolutional layers has kernels of size 5×5 with non-decreasing data depths of 16, 32, 64, and 128. The output of each convolutional layer is rectified by a ReLU unit and accompanied by a pooling layer. The fully connected layer contains a softmax regression layer for final classification. The input of this neural network is 16384-dimensional (128×128); the output is a single label for the number of comets present in the image. The network contains 5.3×105 parameters in total. The overall structure of the neural network can be found in Figure 7.2.

During evaluation, the neural network is evaluated five times and the most common result was used as the output.

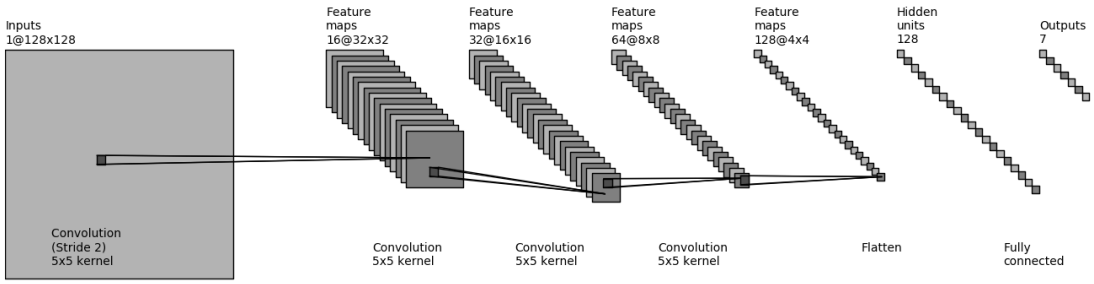

Figure 7.2: Structure of the convolutional neural network. The neural network consists of four convolutional layers and a fully connected layer. All convolutional kernels are 5×5. Each convolutional layer is accompanied by an overlapping average pooling layer. The fully connected layer routes to one of the possible comet counts in 0 to 6.

7.2.3 Considerations to Address Overfitting

Although the network is relatively small with 5.3×10^5 parameters, overfitting is still a big concern since the number of parameters overwhelm the number of training samples. Two measures were taken to address the potential of overfitting: data augmentation and dropout. Data augmentation creates unobserved data from observed data and can reduce the chance of overfitting [19, 20]. To artificially increase the size of the dataset, two kinds of data augmentation were used. First, the images are flipped to double the size of the training set. The second kind of data augmentation involves moving the ROI. The ROI of each image is moved up and down by 5% and 10% of the length of the ROI (410 pixels), as shown in Figure 7.3. The augmented training set was therefore 10 times the original size of the training set, but the inter-dependency of the training samples was increased.

Dropout involves dropping out the neuron in the network when the probability output of the neuron decreases below a certain level [21, 22]. The effective number of parameters within a neural network is reduced when dropout is introduced. In this neural network, a dropout level of 0.25 is used across the third and fourth convolutional layers. The training of the neural network was conducted using MATLAB 2016b (Natick, MA) with MatConvNet [23] beta 20. A standard mini-batch stochas-

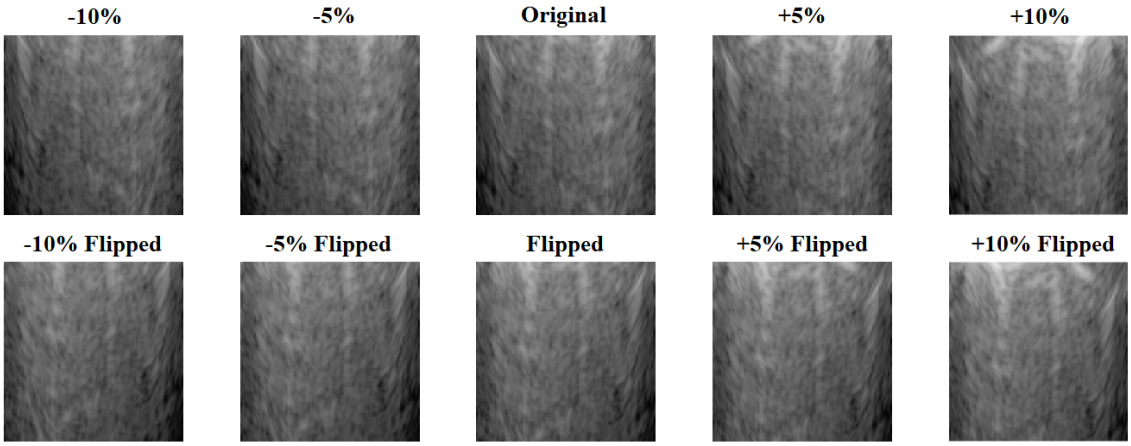

Figure 7.3: Data Augmentation by Moving ROI and Flipping. "+" denotes moving down and "-" denotes moving up. Images shown are extracted from the ROI in Figure 7.1.

tic gradient descent with momentum was used as the minimization algorithm. The batch size was 256. The final network was trained on an Intel Xeon E3-1241 v3 with NVIDIA Quadro K620 GPU with 2GB graphical memory. The training speed on GPU was about two hours. The output of the neural network was exported as plain text files and analyzed using OriginPro (OriginLab, Northampton, MA), SPSS (IBM, Armonk, NY) and R [24].

7.3 Results

Training and testing of the neural network was performed on a 4,864-image dataset obtained by the authors under IRB approval. Overfitting was well controlled with the measures taken as written in the methods section. The neural network counted the number of comets the same as the observer ("true value") in 43.4% of the images. Beyond the correctly identified images, there are another 40.8% of images with an identified comet number of true value $\pm$ 1. The measurement of intraclass correlation (ICC) for observer difference reveals that the agreement between the human-identified comet counts and the output of the neural network is excellent [25] (ICC=0.791). Our reported ICC value is based on absolute agreement. This ICC

value is superior to the ICC (0.586-0.676) of a single person identifying a single set of lung ultrasound images twice as reported by Gullett et al. [12]. A Bland-Altman plot for comparing the observer against the neural network for the test set is available in Figure 7.4. The Bland-Altman plot confirms a relatively low variation between the comet counts identified by hand and by the neural network.

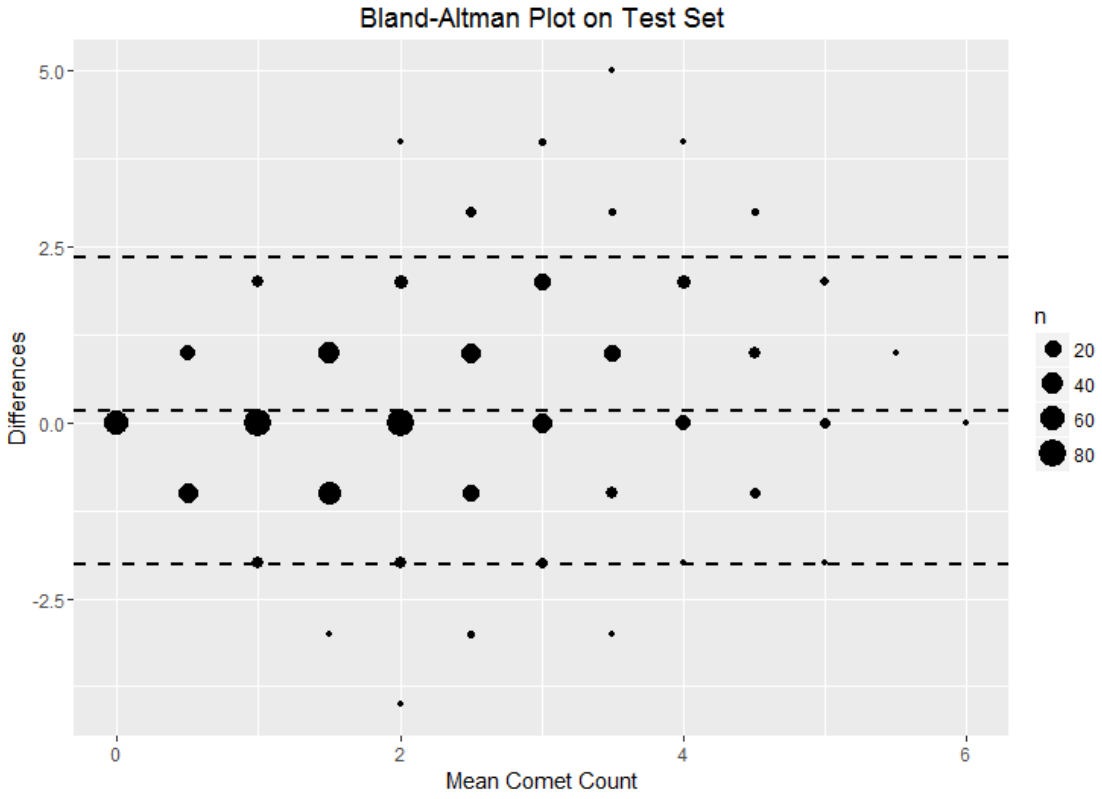

Figure 7.4: Bland-Altman Plot for Test Set. Size of circle denotes sample count. Most samples are centered around the Differences = 0 line, meaning that the human observer agrees well with the neural network.

The results are then rearranged for assessing the diagnostic value of the neural network. Researchers have used different standards for categorizing the severity of the presence of the lung ultrasound comets. Frassi et al. [2] have reported that the presence of 30 comets (at 28 scan sites, average 1.07 comets/image) indicates a severe condition; Gullett et al. [12] used 3 comets per image as the threshold for a comet-positive image. We will use the latter threshold to determine if an image is

comet positive because of our own associated clinical findings. Using this designation, the neural network can categorize 80.8% of images correctly on the test set with a retrained network. From the confusion matrix shown in Table 7.1, we achieved a precision of 73.1% and recall of 62.7%. The corresponding F1-score is 0.675.

Table 7.1: Breakdown of accuracy in categorization of degree of comets present. - means negative and + means positive. 80.8% images were categorized correctly. The precision is 73.1% and recall is 62.7%. The F1-score is 0.675.

		Test	
		−	+
True	−	380	47
	+	76	128

The neural network was then deployed on a larger level of analysis using the exact same dataset as in our previous paper [9]. This 196-loop clinical dataset includes scan location 1-4 of all subjects. A summary of the clinical parameters and demographics is available in Table 7.2. This dataset has a partial overlap with the trained data. The neural network saw 67 out of 196 loops (34.2%) in training, validation, or test set, while the rest 129 (65.8%) are new to the network. We selected this dataset to serve as cross-verification with respect to our previous results despite an optimal clinical set would have no overlap with the data used in the neural network.

Table 7.2: Clinical parameters and demographics of the patients

Clinical Parameter	Range (Mean ± SD)
Age (years)	53±14
Weight (kg)	96±24
BMI	31.5±7.6
Male Sex%	85% (17/20)
Diabetes %	55% (11/20)
Hypertension Documented %	95% (19/20)
Congestive Heart Failure Documented %	5% (1/20)
Coronary Artery Disease Documented %	20% (4/20)
Diastolic Blood Pressure (mmHg)	75±11
Systolic Blood Pressure (mmHg)	134±29
Ejection Fraction %	51±17

The comet counts by the neural network, averaged to patient level, are analyzed

against a series of clinical parameters using linear regression. The comet count exhibits a positive correlation ($p = 0.047$, $r = 0.448$) with respect to diastolic blood pressure and a near-significant negative correlation ($p = 0.061$, $r = -0.513$) with the ejection fraction, as both were confirmed by Weitzel et al. [9]. In the meantime, the patients with a higher BMI ($p = 0.009$, $r = -0.566$) were found to have fewer comets. The systolic blood pressure (p=0.371), final blood volume change ($p = 0.468$), and age ($p = 0.575$) were not found to be significant contributors to comet count. We found similar relationships with respect to the number of positive comet images for each patient, especially in diastolic blood pressure ($p = 0.041$, $r = 0.460$) and ejection fraction ($p = 0.090$, $r = -0.470$). A summary of the results is available in Table 7.3 and Figure 7.5.

Table 7.3: Linear regression of comet count (Count) and number of comet positive images (Comet+) versus relevant clinical parameters, including diastolic and systolic BP (Blood pressure), Final %BV (Change in percent blood volume), EF (Ejection fraction), age, and BMI(body mass index). Significance levels (Sig.): NS - not significant. * - $p < 0.05$. ** - $p < 0.01$. *** - $p < 0.001$. Clinical significance of comet counting is mainly in diastolic BP, EF, and BMI.

Clinical Parameter	Unit	Range	R-value	p-value (Count)	Sig.	p-value (Comet+)	Sig.
Diastolic BP	mmHg	75±11	0.448	0.047	*	0.041	*
Systolic BP	mmHg	134±29	0.211	0.370	NS	0.446	NS
Final %BV	Percent	-8.5 ± 4.7	-0.172	0.468	NS	0.511	NS
EF %	Percent	51 ± 17	-0.513	0.061	NS	0.090	NS
Subject Age	years	53 ± 14	-0.133	0.575	NS	0.441	NS
Subject BMI	kg/m^2	31.5 ± 7.6	-0.566	0.009	**	0.149	NS

Relationship between comet counts and achieved amount of ultrafiltration (UF) is reported in Figure 7.6. Achieved UF, which is positively correlated with body weight, can be seen to be firstly positively correlated with comet count. The correlation then reaches a plateau and drops negative. Our hypothesis with respect to this behavior can be seen in the discussion section.

As a proof of concept for clinical use, two de novo ultrasound loops are randomly selected from the rest of the 500 loops detailed above and fed into the neural network.

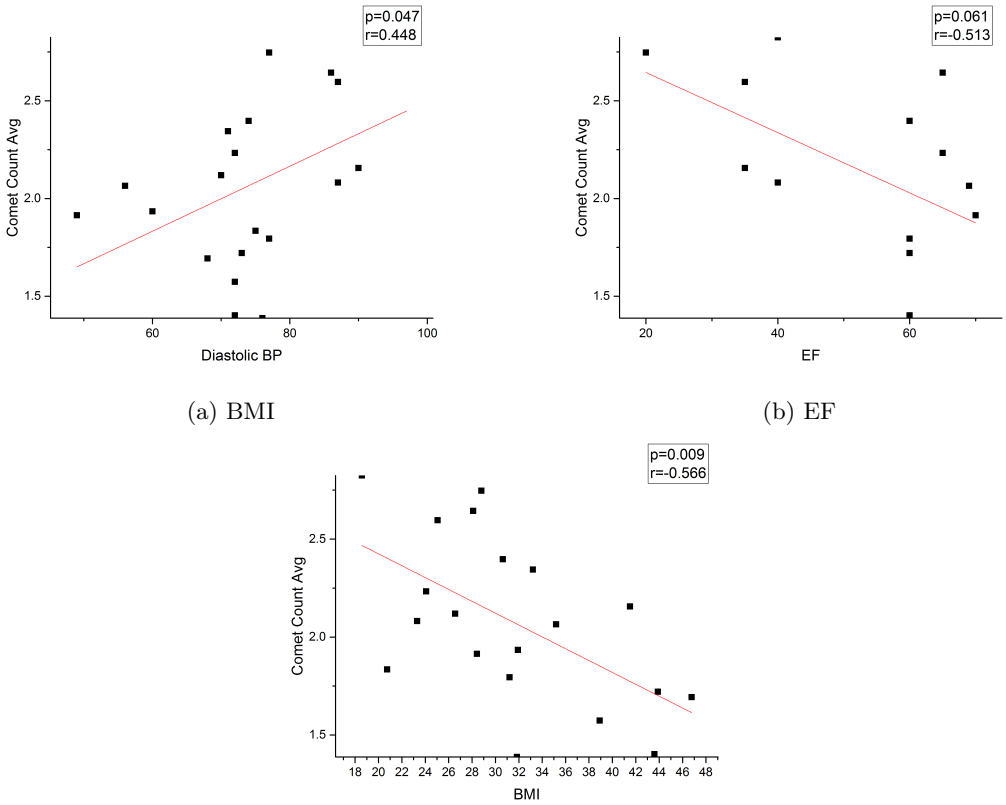

(a) BMI

(b) EF

(c) Diastolic BP

Figure 7.5: (a) Linear Regression of BMI (p=0.009, r=-0.566), (b) Diastolic Blood Pressure (p=0.047, r=0.448), and (c) Ejection Fraction (p=0.061, r=-0.513) against Comet Count.

The comet counts were also identified by hand. The categorized severity of comets was compared between the output of the neural network and hand counting and the results can be seen in Figure 7.7. The agreement is 62.5% on the first loop and 50% on the second loop. On a loop level, hand counting indicated 11 (+) and 21 (++) frames compared to 13 (+) and 19 (++) frames from the neural network for the first loop, both confirming that the first loop is comet dense. The second loop has 12 (-) and 20 (+) when counted by hand and 18 (-) and 14 (+) frames when counted by neural network, suggesting a comet mild loop. There is no severe misidentification in either loop; the indicated clinical outcome is similar.

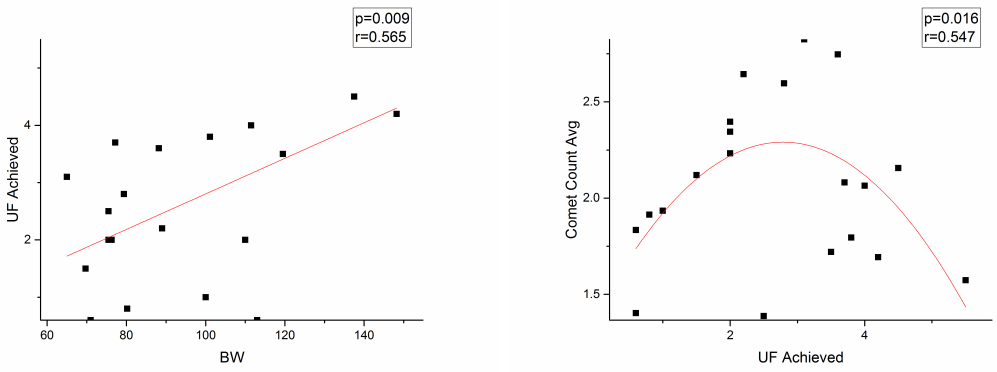

(a) UF vs. Comet Count Average

(b) UF vs. Body Weight

Figure 7.6: (a) A quadratic fit of the amount of ultrafiltration (UF), in liters, achieved with respect to the comet count. They are initially positively correlated until it quickly drops off. The p-value shown is the p-value of the leading quadratic term. The quadratic fit is statistically significant. (b) The amount of UF achieved positively correlates with the body weight of the subject in kilograms (p=0.009).

7.4 Discussion

The lung comet dataset labeled in this study is the largest to date by an order of magnitude compared to the 50-100 images used in existing studies [13, 16]. The database contains images collected from a mechanically scanned single-element transducer, which is representative in a point-of-care and telehealth ultrasound setting, although low cost array imaging systems capable of higher image quality were introduced by Phillips in 2015 and have been evolving. This neural network is a promising approach since it has reasonable accuracy and a low number of parameters. The lower number of parameters leads to increased practicality of implementation since this translates into less computational time and computing power requirements as discussed below. The 43.4% absolute accuracy means that in 43.4% of the images, the neural network identified the same number of lung comets as the observer. Despite an apparently low 43.4% absolute accuracy in the test set, the neural network reached a 0.791 absolute ICC, which indicates a low deviation from the true comet count if the comet count may be incorrect in absolute measures. This ICC suggests

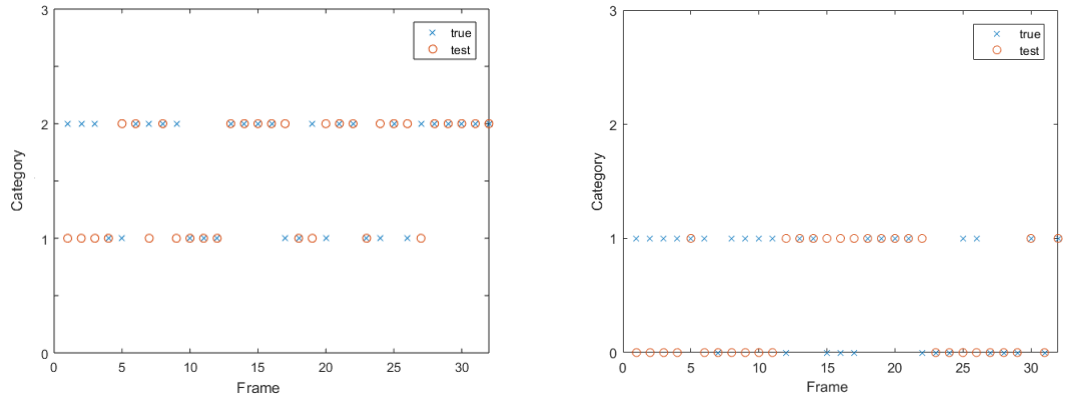

Figure 7.7: Comparison of Categorized Comet Severity for New Data. 0=Negative, 1=Mild, 2=Severe. Both measures agree on the "comet-dense" nature of the first loop with 20/32 (62.5%) agreement on frames. Both measures find the second loop to be "comet mild", with 16/32 (50.0%) agreement on frames. No severe misidentification happened in either loop. On a loop level:
Loop 1: Hand 0 (-) / 11 (+) / 21 (++) vs Neural network 0 (-) / 13 (+) / 19 (++)
Loop 2: Hand 12 (-) / 20 (+) / 0 (++) vs Neural network 18 (-) / 14 (+) / 0 (++)

a higher level of agreement of comet counting between human observers in this study and neural network than that of a single observer counting the comets twice as reported in the literature [12]. The excellent ICC level reveals the potential of using neural network as the "gold standard" in identifying lung comets. In addition, the neural network can still use more training samples and the accuracy and ICC can be further increased with more data. We decided to limit the current study to 4,896 images because of time limitations for the investigators in labeling the images to train the algorithm. With increased data, and additional time resources, a larger neural network may be used to train on the available data, which may further increase the accuracy. However, the accuracy will be limited by the intrinsic variations in comet counting by human. We conjecture that further studies using a combination of lung ultrasound and other available clinical information, such as CT information and patient's medical history, may allow greater pace to be made in improving accuracy within diagnostic tolerance.

Categorizing the ultrasound images into comet negative and positive adds a layer

of supplemental information that may be diagnostically relevant in assessing pulmonary edema. In clinical practice, the presence or absence of comets may be helpful in determining when a patient it at the ideal fluid status (aka "dry weight"), or these categories may relate to how far a patient is from their dry weight.

In the clinical dataset, the clinical findings agree well with our previous results. As in our previous study [9], these neural network findings also suggest that a higher diastolic blood pressure and a lower ejection fraction are correlated with higher comet counts. Patients with fluid overload generally present with a higher blood pressure, and the excess fluid may manifest itself with increased fluid in the lungs and corresponding higher number of comets seen on ultrasound scans. Likewise, a low ejection fraction may be accompanied by excess lung edema and more comets. We hypothesize that the observation of higher BMI being associated with lower comet counts may be attributed to attenuation of the ultrasound signal by adipose tissue. This hypothesis requires further study but is supported by the following. The number of comets is expected to increase with the obtained ultrafiltration (UF) amount, i.e. water obtained during dialysis sessions; this behavior can be seen initially but quickly decreases with increased UF amount, which is positively correlated with the body weight of the subjects. This observation suggests difficulty for the neural network, and potentially for the observer, to see comets in overweight patients. All these observations are suggestive and require further investigation.

Potential future deployment will likely benefit from the relatively low number of parameters that this neural network possesses. With the current structure and its 5.3×10^5 parameters, this neural network requires little computing power. A test on an Intel i5-6260U computer reveals that the comet identification and clinical classification of a full loop (32 frames) takes 0.11-0.12 seconds. The requirement for

memory and storage is on the order of megabytes. These low requirements ensure that most current computing systems will be able to handle this neural network and real-time comet identification is feasible. If deployed on a cloud level, this neural network will require a very small amount of network data transmission, which makes it suitable for potential use in telehealth and Internet applications. A fully automated comet identification system can incorporate another module with automatic ROI identification using either image processing or neural network methods. A fully-automated system adds little tie and effort to the current clinical practice of lung comet identification, potentially be less burdensome than manual comet counting, and has great potential to be a clinical diagnostic tool for lung water assessment. While this neural network exhibits many promising characteristics, there are some limitations exist that require further study.

First, the size of the database contains 4864 ultrasound images. It is the largest lung comet database to date but is still comparatively small compared to a big database such as ImageNet. The number of parameters still overwhelms the number of training samples. The distribution of the comet counts in the database is also somewhat uneven. The distribution of the number of images with respect to its labels ("comet counts") are attached in Table 7.4.

Table 7.4: Distribution of comet count in the comet database. The database contains many frames with low comet counts and few with high comet counts.

Label (Count)	# Images	Percentage (%)
0	748	15.4
1	1248	25.7
2	1225	25.2
3	883	18.2
4	471	9.7
5	201	4.1
6	88	1.8

Second, the neural network has performed reasonably well on the images with low

or medium comet counts (0-3, 48.3% correct) but disagreed with reference measures on the images with high comet counts (4-6, 19.4% correct). This is mainly due to the scarcity of supporting samples in the training set for comet-rich samples. In fact, it is very difficult for an artificial neural network to learn from a small pool of samples [26]. Collecting and using more data in a larger database can mitigate the low accuracy on comet-rich samples. With a much larger database, there would be enough comet-rich samples to train from; the samples can also be randomly pooled at a loop-level instead of an image-level during data split to make the training set and the test set more independent of each other. In this way, loop-level information can be generated and compared to clinical data. A further expansion for future studies would be to obtain lung ultrasound scans from a wide range of patients and pool the data on a patient level.

Third, the database was labeled by a single observer. Thus, the neural network behaves like this observer and contains this observer's subjective tendencies. The comet counting is also subject to observer fluctuations as suggested in a prior publication [12]. Because of the inherent difficulties and visual variations in identifying comets, a training set with input from multiple observers will help reduce subjectivity. Ideally, a pool of physicians will be recruited to perform comet identification in future studies so that the inter-observer variation can be minimized; this too will be the subject of future studies. A reader study characterizing the agreement of a single observer, and between multiple observers, will also be helpful in assessing the reliability of potential automatic comet counting methods.

Finally, the approach to neural network learning, in this case, can also be refined. Instead of labeling the ultrasound image, individual comets can be labeled along with information on their positions. The neural network can then be tuned to learn

from individual comets and identify the comets individually when deployed. This approach can potentially reveal information on the position of the comets and track their movement. A subset of neural networks called U-Net [27] have been applied to biomedical imaging and we are actively pursuing this path.

7.5 Conclusion

Although increasing evidence suggests that lung ultrasound comets may be clinically valuable in assessing pulmonary edema, the objective quantification of these comets has been very challenging. We performed a pilot study to test the feasibility of using a neural network system to perform lung ultrasound counting. A corresponding database of 4,896 ultrasound images was built for this system as the learning source. This machine learning system achieved a 43.4% accuracy in absolute measures and a 0.791 absolute ICC. The apparent low absolute accuracy is reflective of the low inter-measurement agreement of the comet count by a single observer re-reading the same frames. The high ICC level indicates substantial agreement of the neural network algorithm with the comet quantity as counted by a human. With the same sets of parameters, the system categorized 80.8% of the images correctly for the severity of the lung ultrasound comets when divided into a positive and a negative group. With a relatively low number of parameters, this neural network approach shows significant potential in medical decision support systems while requiring only modest computing power. The potential clinical utility of the neural network for lung comet assessment was illustrated by showing correlation between comet count and diastolic blood pressure as well as ejection fraction. Future work on this neural network will involve using more data to improve accuracy, tracking the movement of the comets, testing inter-observer variation, and assessing clinical

parameters, to further test the capabilities of neural networks in quantifying lung ultrasound comets.

Bibliography

[1] Z. Jambrik, S. Monti, V. Coppola, E. Agricola, G. Mottola, M. Miniati, and E. Picano, "Usefulness of ultrasound lung comets as a nonradiologic sign of extravascular lung water," *The American journal of cardiology*, vol. 93, no. 10, pp. 1265–1270, 2004.

[2] F. Frassi, L. Gargani, P. Tesorio, M. Raciti, G. Mottola, and E. Picano, "Prognostic value of extravascular lung water assessed with ultrasound lung comets by chest sonography in patients with dyspnea and/or chest pain," *Journal of cardiac failure*, vol. 13, no. 10, pp. 830–835, 2007.

[3] L. Gargani, F. Frassi, G. Soldati, P. Tesorio, M. Gheorghiade, and E. Picano, "Ultrasound lung comets for the differential diagnosis of acute cardiogenic dyspnoea: A comparison with natriuretic peptides," *European journal of heart failure*, vol. 10, no. 1, pp. 70–77, 2008.

[4] D. Lichtenstein, G. Meziere, P. Biderman, A. Gepner, and O. Barre, "The comet-tail artifact: an ultrasound sign of alveolar-interstitial syndrome," *American journal of respiratory and critical care medicine*, vol. 156, no. 5, pp. 1640–1646, 1997.

[5] E. Picano, F. Frassi, E. Agricola, S. Gligorova, L. Gargani, and G. Mottola, "Ultrasound lung comets: a clinically useful sign of extravascular lung water," *Journal of the American Society of Echocardiography*, vol. 19, no. 3, pp. 356–363, 2006.

[6] D. Lichtenstein, G. Meziere, P. Biderman, and A. Gepner, "The comet-tail artifact: an ultrasound sign ruling out pneumothorax," *Intensive care medicine*, vol. 25, no. 4, pp. 383–388, 1999.

[7] C. Zoccali, C. Torino, R. Tripepi, G. Tripepi, G. D'Arrigo, M. Postorino, L. Gargani, R. Sicari, E. Picano, F. Mallamaci, *et al.*, "Pulmonary congestion predicts cardiac events and mortality in esrd," *Journal of the American Society of Nephrology*, vol. 24, no. 4, pp. 639–646, 2013.

[8] F. Mallamaci, F. A. Benedetto, R. Tripepi, S. Rastelli, P. Castellino, G. Tripepi, E. Picano, and C. Zoccali, "Detection of pulmonary congestion by chest ultrasound in dialysis patients," *JACC: Cardiovascular Imaging*, vol. 3, no. 6, pp. 586–594, 2010.

[9] W. F. Weitzel, J. Hamilton, X. Wang, J. L. Bull, A. Vollmer, A. Bowman, J. Rubin, G. H. Kruger, J. Gao, M. Heung, *et al.*, "Quantitative lung ultrasound comet measurement: method and initial clinical results," *Blood purification*, vol. 39, no. 1-3, pp. 37–44, 2015.

[10] V. Panuccio, G. Enia, R. Tripepi, C. Torino, M. Garozzo, G. G. Battaglia, C. Marcantoni, L. Infantone, G. Giordano, M. L. De Giorgi, *et al.*, "Chest ultrasound and hidden lung congestion in peritoneal dialysis patients," *Nephrology Dialysis Transplantation*, vol. 27, no. 9, pp. 3601–3605, 2012.

[11] G. Soldati, R. Copetti, and S. Sher, "Can lung comets be counted as "objects"?," *JACC: Cardiovascular Imaging*, vol. 4, no. 4, pp. 438–439, 2011.

[12] J. Gullett, J. P. Donnelly, R. Sinert, B. Hosek, D. Fuller, H. Hill, I. Feldman, G. Galetto, M. Auster, and B. Hoffmann, "Interobserver agreement in the evaluation of b-lines using bedside ultrasound," *Journal of critical care*, vol. 30, no. 6, pp. 1395–1399, 2015.

[13] L. J. Brattain, B. A. Telfer, A. S. Liteplo, and V. E. Noble, "Automated b-line scoring on thoracic sonography," *Journal of Ultrasound in Medicine*, vol. 32, no. 12, pp. 2185–2190, 2013.

[14] R. Moshavegh, K. L. Hansen, H. M. Sørensen, M. C. Hemmsen, C. Ewertsen, M. B. Nielsen, and J. A. Jensen, "Novel automatic detection of pleura and b-lines (comet-tail artifacts) on in vivo lung ultrasound scans," in *Medical Imaging 2016: Ultrasonic Imaging and Tomography*, vol. 9790, p. 97900K, International Society for Optics and Photonics, 2016.

[15] N. Anantrasirichai, M. Allinovi, W. Hayes, and A. Achim, "Automatic b-line detection in paediatric lung ultrasound," in *2016 IEEE International Ultrasonics Symposium (IUS)*, pp. 1–4, IEEE, 2016.

[16] N. Anantrasirichai, W. Hayes, M. Allinovi, D. Bull, and A. Achim, "Line detection as an inverse problem: application to lung ultrasound imaging," *IEEE transactions on medical imaging*, vol. 36, no. 10, pp. 2045–2056, 2017.

[17] D. D. Cox and T. Dean, "Neural networks and neuroscience-inspired computer vision," *Current Biology*, vol. 24, no. 18, pp. R921–R929, 2014.

[18] A. Krizhevsky, I. Sutskever, and G. E. Hinton, "Imagenet classification with deep convolutional neural networks," in *Advances in neural information processing systems*, pp. 1097–1105, 2012.

[19] M. A. Tanner and W. H. Wong, "The calculation of posterior distributions by data augmentation," *Journal of the American statistical Association*, vol. 82, no. 398, pp. 528–540, 1987.

[20] A. Karpathy, G. Toderici, S. Shetty, T. Leung, R. Sukthankar, and L. Fei-Fei, "Large-scale video classification with convolutional neural networks," in *Proceedings of the IEEE conference on Computer Vision and Pattern Recognition*, pp. 1725–1732, 2014.

[21] G. E. Hinton, N. Srivastava, A. Krizhevsky, I. Sutskever, and R. R. Salakhutdinov, "Improving neural networks by preventing co-adaptation of feature detectors," *arXiv preprint arXiv:1207.0580*, 2012.

[22] N. Srivastava, G. Hinton, A. Krizhevsky, I. Sutskever, and R. Salakhutdinov, "Dropout: a simple way to prevent neural networks from overfitting," *The journal of machine learning research*, vol. 15, no. 1, pp. 1929–1958, 2014.

[23] A. Vedaldi and K. Lenc, "Matconvnet: Convolutional neural networks for matlab," in *Proceedings of the 23rd ACM international conference on Multimedia*, pp. 689–692, 2015.

[24] R. C. Team *et al.*, "R: A language and environment for statistical computing," 2013.

[25] D. V. Cicchetti, "Guidelines, criteria, and rules of thumb for evaluating normed and standardized assessment instruments in psychology.," *Psychological assessment*, vol. 6, no. 4, p. 284, 1994.

[26] N. Pinto, D. D. Cox, and J. J. DiCarlo, "Why is real-world visual object recognition hard?," *PLoS computational biology*, vol. 4, no. 1, 2008.

[27] O. Ronneberger, P. Fischer, and T. Brox, "U-net: Convolutional networks for biomedical image segmentation," in *International Conference on Medical image computing and computer-assisted intervention*, pp. 234–241, Springer, 2015.

Chapter VIII

Future Directions: Comet Quantification

8.1 Introduction

It is clear that neither the image processing method introduced in Chapter VI and the machine learning method in Chapter VII are perfect. One important aspect of comet quantification is left out in each study.

The image processing method in Chapter VI uses a single threshold for all images, and tuning of the threshold parameter was purely empirical. Although clinical significance was found, the results were not verified by a human-labeled database so that the accuracy of the method was not verified. It also required a human-labeled region of interest (ROI). The strength of the method is that this method was also a segmentation method that displays the detected comets on the screen, giving more information about the movement of comets, which has been overlooked so far. This method is also flexible in the quantifying measure of comets reported, including the comet count, fraction, and average width.

The machine learning method in Chapter VII achieves greater consistency and is more objective than human labeling, but a few problems still exist. First, a labeled ROI is still needed - although in our case, we recycled the ROI from Chapter VI. The maximum number of comets present inside a ultrasound image is limited at 6

and the algorithm has low accuracy in identifying comet-rich images due to the lack of data in the training set. This system is also not clinic-ready: the system operates as a black box by simply telling you how many comets there are in an image, but not where they are and why. It is not capable of generating other quantitative measures.

Automatic segmentation of lung comets using machine learning is the perfect marriage of the two. Segmentation networks can process images in patches and segment the information of interest. This chapter will illustrate recommendations of using segmentation networks, such as U-Nets [1], as a way to identify the number and location of the comets. In this chapter, we will discuss about the data collection utility and database we collected, and offer future recommendations for doing automatic comet segmentation with this utility or database.

8.2 Data Collection for Segmentation Networks

Segmentation networks require a different kind of label: masks of the pixel locations of the comets.

To achieve the best results, we need data labeled by experts. Therefore, we designed an application for clinicians to provide labeled comets. The main graphical user interface (GUI) is shown below in Figure 8.1.

Users can use this utility to label comets in shape of rectangles. For labeling one comet, the user would click on the image where the top-left corner of the comet is, and the down-right corner. Real time information of instructions is displayed on the top, and the current coordinates and progress within the cine loop is displayed on the right.

The ultrasound image displayed is very lightly processed by normalizing the image by its standard deviation to avoid affecting downstream machine learning systems.

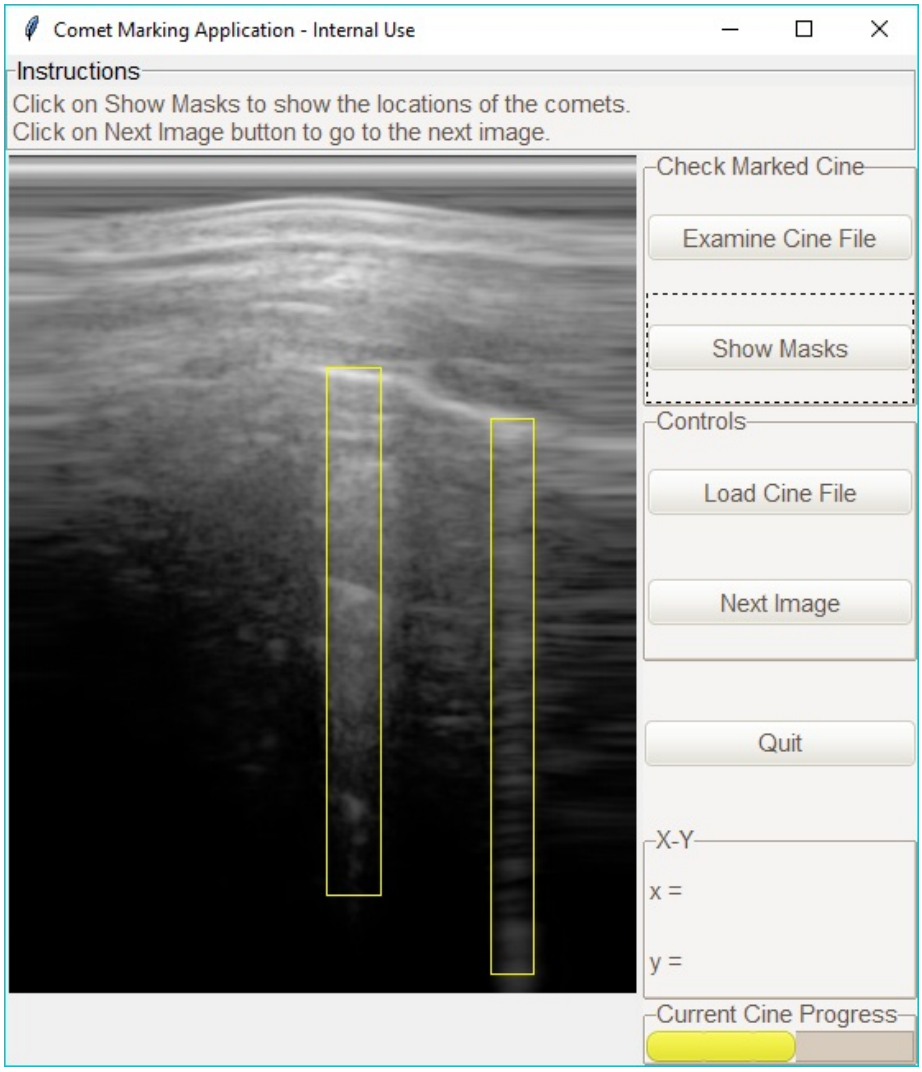

Figure 8.1: Main GUI for the comet labeling application. The application provides features including labeling comets, storing labels, and recalling labeled information.

Each frame of the cine loop is labeled, and then the information of the normalized images and the masks are compressed and stored on disk.

This application is written in Python 3 and is available as a standalone executable with packaged readme help document. The source code is available at `https://gitlab.com/bioxusn/comet-marking` if access is granted.

We invited an expert physician and an amateur to label comets using our utility on the dataset we collected in Chapter VI. The physician labeled 45 loops, for all patients at the same locations, and the amateur labeled all 88 loops we collected

from a single patient. Each loop contains 32 frames.

We additionally collected another set of clinical dataset. Our expert labeled 96 loops in the test set.

The dataset is currently protected. Characterization with the 45 loops labeled by the expert physician reveals 0.5% comet pixels and 99.5% non-comet pixels.

8.3 Future Directions

Labeling data can be extremely expensive and time-consuming. We first offer suggestions on performing studies on the dataset that we collected and some potential evaluation methods, and then we will offer suggestions on how to improve the dataset to enhance the performance of potential machine learning studies.

8.3.1 Class Balancing for Segmentation Networks

Class imbalance is detrimental to the performance to convolutional neural networks [2] and in our case, the distribution of the classes is extremely biased. In addition, we have seen the large gap in the performance of the lower-represented classes in Chapter VII. To make the classes more balanced, we suggest the following measures as an attempt to balance the classes.

First, we suggest using a Dice-coefficient based cost function [3, 4]. The Dice loss has shown to be more resistant to class imbalances [5] than traditional cost functions, such as the cross-entropy.

Second, we suggest using data augmentation techniques to artificially increase the samples containing more comet pixels.. Data augmentation is a procedure to create unobserved data from observed data to enlarge the size of the dataset [6]. One way is to aggressively oversampling the data, as shown in Figure 8.2.

Using synthetic data for lung comets is another possible solution for augmen-

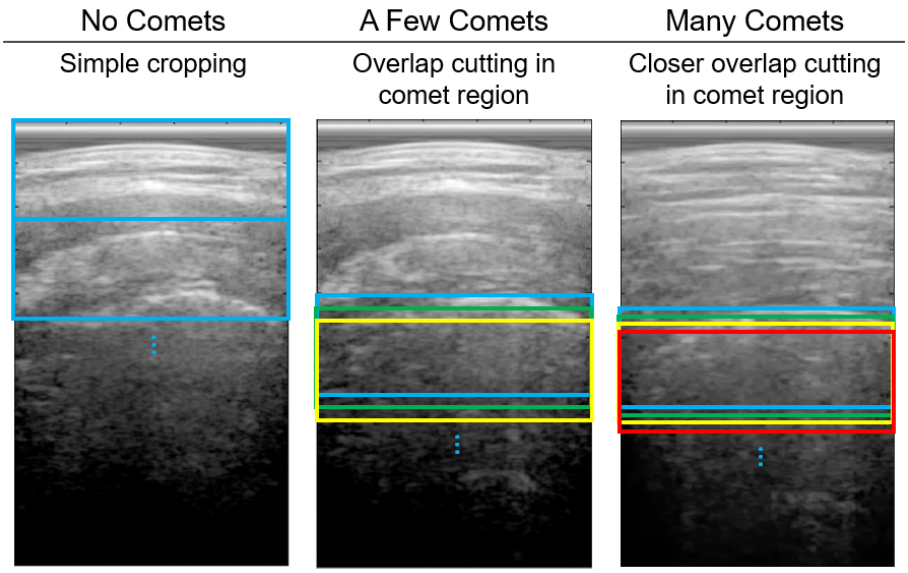

Figure 8.2: Oversampling the data. The image size is 2048×256. We use sliding windows to sample the image with window size 256×256. If the image does not contain a comet, the step size is 256. The step decreases according to the amount of comet-positive pixels inside an image.

tation. Generative adversarial networks (GANs) are designed for generating new samples from learned distribution from an existing dataset. Since we have many comet-negative loops, it could be beneficial to use a style transfer GAN [7] to convert a comet-negative image to a comet-positive image in order to balance the class representations.

8.3.2 Evaluation Methods

Pixel-wise accuracy may not be the best evaluation metric for segmentation of lung comets: missing a few pixels may not be as important as say, segmenting cell boundaries. Alternatively, two metrics have been proposed by Fenster and Chiu [8], including a distance-based metric and an area-based metric. The distance-based metric compares the distance between the true and predicted boundaries of the enclosed areas; the area-based metric quantifies an F1-score based on the area of positively-identified regions.

In addition, since lung comets are still traditionally counted as objects, traditional

assessment scores such as intraclass correlation (ICC) can still be used.

8.3.3 Suggestions on the Dataset

Since the amount of comet-positive data is severely lacking, the priority should be to collect and label more data that contain many comets. This addresses the class-imbalance problem from the core.

The dataset is tied to a single transducer and may not be readily applicable to other transducers. Since lung ultrasound has not been standardized in the clinics, data from preferably multiple kinds of scanners and scanning depths should be collected for easy adaptation to future standardization.

One could also attempt to get more people to label the comets using the comet-labeling tool. In fact, the data we collected from the amateur and the expert have 4 loops in common. With enough consistency between labelers, the neural network would benefit from receiving more labeled data. A study on the ICC of the existing data can offer elementary insight on the consistency of comet interpretation, although more labelers are still strongly preferred.

Bibliography

[1] O. Ronneberger, P. Fischer, and T. Brox, "U-net: Convolutional networks for biomedical image segmentation," in *International Conference on Medical image computing and computer-assisted intervention*, pp. 234–241, Springer, 2015.

[2] M. Buda, A. Maki, and M. A. Mazurowski, "A systematic study of the class imbalance problem in convolutional neural networks," *Neural Networks*, vol. 106, pp. 249–259, 2018.

[3] C. F. Baumgartner, L. M. Koch, M. Pollefeys, and E. Konukoglu, "An exploration of 2d and 3d deep learning techniques for cardiac mr image segmentation," in *International Workshop on Statistical Atlases and Computational Models of the Heart*, pp. 111–119, Springer, 2017.

[4] J. Bertels, T. Eelbode, M. Berman, D. Vandermeulen, F. Maes, R. Bisschops, and M. B. Blaschko, "Optimizing the dice score and jaccard index for medical image segmentation: Theory and practice," in *International Conference on Medical Image Computing and Computer-Assisted Intervention*, pp. 92–100, Springer, 2019.

[5] S. A. Taghanaki, Y. Zheng, S. K. Zhou, B. Georgescu, P. Sharma, D. Xu, D. Comaniciu, and G. Hamarneh, "Combo loss: handling input and output imbalance in multi-organ segmentation," *Computerized Medical Imaging and Graphics*, vol. 75, pp. 24–33, 2019.

[6] D. A. Van Dyk and X.-L. Meng, "The art of data augmentation," *Journal of Computational and Graphical Statistics*, vol. 10, no. 1, pp. 1–50, 2001.

[7] L. Zhang, Y. Ji, X. Lin, and C. Liu, "Style transfer for anime sketches with enhanced residual u-net and auxiliary classifier gan," in *2017 4th IAPR Asian Conference on Pattern Recognition (ACPR)*, pp. 506–511, IEEE, 2017.

[8] A. Fenster and B. Chiu, "Evaluation of segmentation algorithms for medical imaging," in *2005 IEEE Engineering in Medicine and Biology 27th Annual Conference*, pp. 7186–7189, IEEE, 2006.